1.0

1.1

1.25 1.4 1.6

1.8

2.0

2.2

2.5

2.8

3.2

3.6

4.0

MIZEX

BULLETIN VII

DTIC FILE COPY

DTIC
ELECTE
SEP 2 9 1986
S
A
D

MARCH 1986

BULLETIN

86 9 09 059

MIZEX BULLETIN SERIES: INFORMATION FOR CONTRIBUTORS

The main purpose of the MIZEX Bulletin series* is to provide a permanent medium for the interchange of initial results, data summaries, and theoretical ideas relevant to the Marginal Ice Zone Experiment. This series will be unrefereed and should not be considered a substitute for more complete and finalized journal articles.

Because of the similarity of the physics of the marginal ice zone in different regions, contributions relevant to any marginal ice zone are welcome, provided they are relevant to the overall goals of MIZEX.

These overall goals are discussed in Bulletin I (Wadhams et al., CRREL Special Report 81-19), which described the research strategy, and Bulletin II (Johannesen et al., CRREL Special Report 83-12), which outlined the science plan for the main 1984 summer experiment. Copies of earlier or current bulletins may be obtained from the Technical Information Branch, USA CRREL.

Persons interested in contributing articles to the bulletin should send copies to one of the editors listed below with figures reproducible in black and white. Proofs of the retyped manuscripts will not be sent to the author unless specifically requested.

Science Editors:

W.D. Hibler III
USA Cold Regions Research and
and Engineering Laboratory
72 Lyme Road
Hanover, New Hampshire 03755-1290

Peter Wadhams
Scott Polar Research Institute
Lensfield Road
Cambridge CB2 1ER
United Kingdom

Technical Editor:

Maria Bergstad
USA Cold Regions Research
and Engineering Laboratory
72 Lyme Road
Hanover, New Hampshire 03755-1290

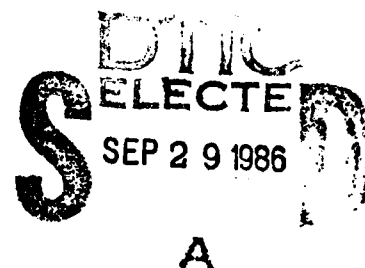*Cover: The MV* Polarbjørn *in the marginal ice zone during the drift phase of MIZEX 83. Photo taken 27 June 1983 from an altitude of 1400 ft by Vernon Squire. The Polarbjørn is 50 m in length.*

MIZEX
A Program for Mesoscale Air-Ice-Ocean Interaction Experiments in Arctic Marginal Ice Zones

MIZEX BULLETIN VII

March 1986

U.S. Army Cold Regions Research and Engineering Laboratory
Hanover, New Hampshire, USA

PREFACE

This bulletin contains a collection of articles ranging from analysis of observational data on the marginal ice zone to theoretical papers relevant to the physics of air/ice/ocean dynamics in the MIZ. As such it represents a more general format for articles describing the marginal ice zone than previous bulletins. We will continue this more general format in most future issues, with occasional special issues interspersed. Authors are encouraged to submit articles on any aspect of marginal ice zone studies in both the northern and southern hemispheres.

W.D. HIBLER III
March 1986

CONTENTS

QUALITY
INSPECTED
1

Accession For

NTIS GRA&I

DTIC TAB

Unannounced

Justification

By

Distribution/

Availability Codes

Dist	Avail and/or Special
A-1	

A Note on Estimating Melt Rate in the MIZ

MILES G. McPHEE

McPhee Research Company, Route 8, Box 304H, Yakima, Washington 98908

How heat and salt are exchanged at the ice/ocean interface is a central issue in understanding the thermodynamics and the dynamics of the marginal ice zone. The intent of this note is to assemble some ideas about boundary conditions at the horizontal ice/ocean interface, to investigate what they imply for the oceanic boundary layer, and to present an approximate method for estimating melt rates of sea ice when the predominant heat transfer is from the ocean. The note is purposely informal, and if it generates further discussion, I will consider it worthwhile.

In the 1983 MIZ issue of the *Journal of Geophysical Research*, Ed Josberger and I each published articles (Josberger, 1983; McPhee, 1983) on how sea ice melts in above-freezing water. Considering that we used rather similar methods, it was somewhat surprising that we came to diametrically opposed conclusions regarding the importance of buoyancy flux in the dynamics of the planetary boundary layer (PBL). I wrote a comment on Josberger's article (McPhee, 1984) to the effect that he had incorrectly calculated the Obukhov length, and he replied (Josberger, 1984) that I failed to treat conditions at the ice/ocean interface properly.

To some extent, Ed was right. The fact is, I was not sure what to use for a boundary condition at the ice/ocean interface (I was unconvinced that saline ice would melt under equilibrium conditions in the complex environment that makes up the interface), so I avoided the question by formulating the problem in terms of change in mean temperature across the PBL, and by relating the surface salinity flux to the product of ice growth rate and the difference between mixed-layer and ice salinities. My approach amounts to considering some level a little removed from the actual interface, then assuming that the momentum flux (stress) and heat and salinity fluxes are the same there as they are at the interface, a common and useful approximation in boundary-layer studies. If one assumes that the average heat and salt fluxes are proportional to the overall ice growth rate, then the problem can be solved without direct reference to S_0 and T_0, the interfacial salinity and temperature, even though it is somewhat unsatisfying to deal with changes across the PBL rather than absolute values.

As Ed and I were airing our differences, George Mellor, who was visiting the Naval Postgraduate School at the same time I was, took interest in the ice/ocean PBL problem. George used the freezing-line T_0/S_0 relationship to put the boundary conditions for his numerical PBL model capped with ice on a rigorous footing. We have since applied the Mellor-Yamada 'level 2.5' time-dependent model to the regime, first results of which will soon be out in a manuscript by Mellor, McPhee, and Steele. This note discusses those boundary conditions as George formulated them, and their implication for simpler, steady-state PBL models.

Consider a thermodynamic control volume of infinitesimal extent surrounding the ice/ocean interface and moving with it, as diagrammed in Figure 1. We assume that neither mass nor energy accumulates within the volume and describe the rate of freezing by the ice growth rate, d. Mass conservation and isostasy require the vertical velocity of fluid into the control volume to be $w = -(\varrho_i/\varrho_0)\,d$. (Dynamically, this 'injection velocity' is insignificant relative to other fluid velocities and is ignored in the equations of motion.) The change in enthalpy is dominated by the phase change (about 60 times the sensible heat change), so the first-law balance is approximately:

$$\varrho_0 c_p < w'T'>_0 \; = \; \varrho_0 w L_s - k_s \left. \frac{\partial T_i}{\partial z}\right|_0$$

where $k_s\,(\partial T_i/\partial z)|_0$ is heat conduction through the ice and $\varrho_0\,c<w'T'>_0$ is heat flux from the ocean. Latent heat, L_s, and thermal conductivity, k_s, are functions of ice salinity and can be appreciably different from their fresh-ice counterparts. The 'kinematic' heat flux is:
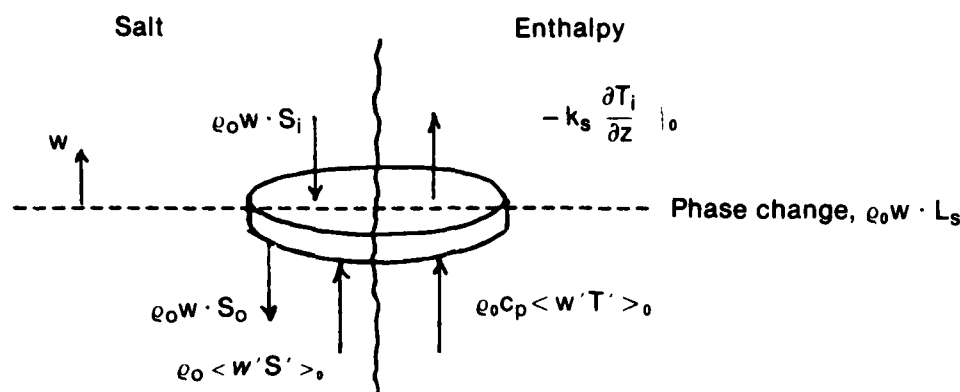
Fig. 1. *Schematic of thermodynamic control volume surrounding ice/water interface.*

$$<w'T'>_0 = Q_L w - \frac{k_s}{\varrho_0 c_p} \frac{\partial T_i}{\partial z}\Big|_0 \qquad (1)$$

where $Q_L = L_s/\varrho_0 c_p$ has temperature units with a typical value of about 60 °C.

Salt conservation is treated similarly. As the control volume moves, flux and advection at the lower surface are balanced by advection only at the upper surface, since we ignore salt diffusion in the ice:

$$\varrho_0 <w'S'>_0 + \varrho_0 w S_i = \varrho_0 w S_0.$$

The salinity flux is thus

$$<w'S'>_0 = w(S_0 - S_i) \qquad (2)$$

When ice melts, the salinity flux is positive, meaning that salt (and mass) are transported upward, which is to say that relatively fresh melt water is mixed down by turbulent (and molecular) processes. At temperatures near freezing, the thermal expansion coefficient of sea water is small, and buoyancy is governed mainly by the salt flux.

What do the surface flux conditions imply about the boundary layer? First, suppose we know the mean salinity and temperature at some level near the interface in the turbulent flow. By choosing the level close enough, the 'wall-layer' conditions of constant flux and small buoyancy effects can be approximated. We further assume that turbulent diffusivities for momentum, heat, and salt are the same, so we have

$$kzu_* \left[\frac{\partial T}{\partial z}, \frac{\partial S}{\partial z}\right] = \left| <w'T'>_0, <w'S'>_0 \right|$$

so

$$T_0 - T = \frac{<w'T'>_0}{ku_*} \ln\left(\frac{-Z}{z_{OT}}\right) \qquad (3)$$

$$S_0 - S = \frac{<w'S'>_0}{ku_*} \ln\left(\frac{-Z}{Z_{OS}}\right) \qquad (4)$$

where k is von Karman's constant, equal to 0.4.

According to Gill (1982), the freezing temperature of sea water is

$$T_f(S,p) = -0.0575S + 1.710523 \times 10^{-3} S^{1/2}$$

$$-2.154996 \times 10^{-4} S^2 - 7.53 \times 10^{-3} p$$

where S is in ppt and p in bars. This is often linearized to

$$T_f = -mS \qquad \text{where } m = 0.06 \,°C/(\%_0)$$

If interfacial stress $(\varrho_0 u_*^2)$ is known, we now have a third equation for the unknowns T_0, S_0, and w that is readily solved. We used this approach to tie the interface quantities to flow properties of the first grid point in the Mellor-Yamada numerical model.

Now suppose we have neither measurements nor a numerical model to specify conditions in the near surface layer, but that we can estimate the 'far-field' temperature, and salinity and the stress acting at the ice/water interface. Is there a simple way of estimating, say, melt rate? Perhaps. Two factors make this problem less tractable than the surface layer approach described above: first, turbulent flux is not constant across the entire PBL, but instead decreases from its surface value to zero

2

and, second, the eddy viscosity loses its simple linear z-dependence. Actually, the similarity model I used in McPhee (1983) is quite simple, but requires some familiarity with my notation and peculiar way of viewing the PBL. In a sense, what follows is a further simplification of that theory, which may help explain its function. Josberger used an analogous technique but, in addition to our difference about what constitutes buoyancy flux, made two assumptions with which I disagree, as explained below.

It helps to review some rudimentary concepts about steady, horizontally homogeneous planetary boundary layers. First, almost by definition, the PBL extends through the region where turbulent flux of momentum and scalar properties occurs. By implication, these fluxes must fall off to zero somewhere near the outer limits of the PBL. This is the source of one of my disagreements with Josberger—he assumed constant flux for heat and salt (but not momentum) through the entire PBL. Second, there seem to be three length scales that affect the large-scale behavior of turbulence in the PBL. They are: 1) a scale proportional to u_*/f, which derives from a conditional stability related to rotation of the reference frame; 2) the distance from the fluid/solid interface; and 3) the Obukhov length, which is essentially the vertical distance a fluid parcel moves in a density-stratified flow before its initial kinetic energy is converted to gravitational potential energy. In general, turbulence at a given level in the PBL responds to whichever length scale is shortest at that point. Using this paradigm, my studies have shown that the length scale of the energy-containing eddies in a neutrally stratified flow will increase until it reaches roughly $(1/20) \cdot u_*/f$. Beyond that level, the turbulence is 'free,' meaning the eddies are no longer affected by the wall itself. The neutral boundary layer seems to extend to about 8 or 10 times the scale of the largest eddies, say 0.4 to 0.5 u_*/f.

If the stratifying tendency is strong, as it is when ice melts rapidly, the Obukhov length is short, limiting the maximum length scale of the eddies relative to the neutral case. The basic idea behind similarity in fluid dynamical problems is to find scales that collapse a whole class of physical realizations to one equation, the solution of which then has a general nature. My similarity theory (McPhee, 1981) for the outer layer combines the planetary scale and the Obukhov length in a scale for the effective vertical influence of the largest eddies. When this scale is specified, other properties (e.g., the depth of the PBL, which is constant in the similarity coordinates) fall out automatically. Increased surface buoyancy decreases the length scale, limits the size of the boundary layer, and traps the effect of surface fluxes closer to the surface. There is a significant feedback here: as turbulent heat flux increases, so does melting, which inhibits the efficiency of turbulent transfer. For this reason, a bulk Stanton-number approach for calculating heat flux should be examined critically, if used in a regime with turbulence levels different from that used to derive the Stanton number. An interesting consequence of the same effect is that by confining momentum flux to a shallower region, increased buoyancy causes faster near-surface currents (and ice velocity) for the same interfacial stress. Buoyancy-caused change in the
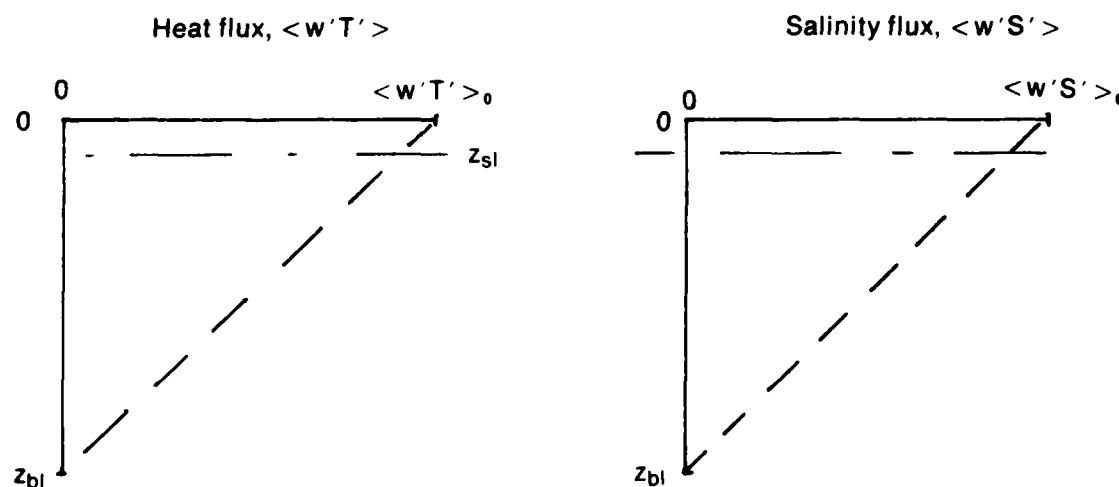

Heat flux, $<w'T'>$

Salinity flux, $<w'S'>$

Fig. 2. Flux profiles in boundary layer under melting ice.

3

PBL depth is a second source of my disagreement with Josberger: he sets the PBL depth to the limit I suggested for the neutral case ($0.5\ u_*/f$) and leaves it there regardless of surface buoyancy flux.

Consider a melting regime with no heat conduction through the ice, as sketched in Figure 2. The dashed lines are meant to indicate that there is nothing *a priori* known about the shape of the profiles, just that they fall from surface values to near zero at the far extent of the PBL. We can simplify matters greatly by assuming that a) the form of the scalar flux profiles is similar, and that b) the eddy diffusivities are the same for salinity and heat, as are c) the surface roughnesses. Each of these assumptions occupies long (sometimes tedious) hours of argument among turbulence students, but for the present purposes it is safe to say that none is in gross error. With that, we can immediately write:

$$\frac{\partial}{\partial z}\ [T,S] = -[Q_L w, w(S_0-S_i)]\cdot\frac{F}{K}$$

where F is a function that describes the shape of both flux profiles and K is eddy diffusivity.

Integrating from the base of the PBL, we have

$$[(T_0-T_\infty), (S_0-S_\infty)] = [Q_L w,\ w(S_0-S_i)]\cdot$$

$$\int_{z_{bl}}^{-z_o} \frac{F}{K}\ dz \qquad (5)$$

from which

$$\frac{T_0-T_\infty}{Q_L} = \frac{S_0-T_\infty}{S_0-S_i}$$

and with the freezing line approximation, $T_0 = -m\cdot S_0$, and some rearranging,

$$\frac{S_0}{S_\infty} = \frac{Q_L-\left(\frac{S_0-S_i}{S_\infty}\right)T_\infty}{Q_L+m(S_0-S_i)} \qquad (6)$$

This can be written as a quadratic in S_0 and solved, but casting it in this form shows that the ratio is dominated by Q_L (which is about 60°C), so that for realistic MIZ values of S_∞ and T_∞ it is always within a few percent of unity. Similarly, T_0 is within a few tenths of a degree of the freezing point of the far field, $-mS_\infty$. For practical purposes, the difference between S_0 and S_∞ is overshadowed by the uncertainty in S_i and Q_i, and ex-

act specification of conditions at the interface is not crucial to specifying heat and salt flux. Note that this result follows from assumptions a through c listed above, and not from any particular form specified for the flux profile shape or eddy diffusivity.

For a useful estimate of melt rate, we have to address the integral in equation 5; specifically, the shape of the flux profile and the eddy viscosity. It turns out that assuming a linear fall off to scalar fluxes is not a bad description for a number of modeling and experimental studies. Much more important than the exact form of the curve is the depth to which turbulence penetrates. Without going into the details of its derivation, I worked out a theory several years ago (McPhee, 1981), using the three scales described at the beginning of this section, that specifies a scale for the free turbulence. As a first-order approximation to that theory, eddy viscosity may be written:

$$K = -kzu_*; \qquad -z_0 > z > z_{sl}$$

$$K = k\xi_N u_*^2\eta_*^2/f; \qquad z_{sl} > z > z_{bl}$$

where

$$z_{sl} = -u_*\eta_*^2\xi_N/f \qquad z_{bl} = -ku_*\eta_*/f$$

where ξ_N is a constant, about 0.05, and η_* is a stability parameter described below. Assuming heat flux is linear from its surface value to zero at z_{bl}, the equation may be integrated in two parts, through the outer, free-turbulence layer, and through a surface layer:

$$\frac{T_0-T_\infty}{wQ_L} = \frac{1}{ku_*}\int_{z_{sl}}^{-z_{ot}}\left(\frac{1}{z}-\frac{1}{z_{bl}}\right)dz +$$

$$\frac{f}{k\xi_N u_*^2\eta_*^2}\int_{z_{bl}}^{z_{sl}}\left(1-\frac{z}{z_{bl}}\right)dz.$$

A straightforward scale analysis shows that the integral is dominated by two terms, and the equation may be written

$$\Lambda = \frac{u_*(T_0-T_\infty)}{wQ_L} = \frac{1}{k}\overbrace{\ln\left(\frac{u_*\xi_N}{fz_{OT}}\cdot\eta_*^2\right)}^{\Lambda_1}+\overbrace{\frac{1}{2\xi_N\eta_*}}^{\Lambda_2} \qquad (7)$$

4

$\Lambda = \Lambda_1 + \Lambda_2$ is the inverse of a heat transfer coefficient and comprises two parts: Λ_1 is the surface layer contribution to the boundary-layer integral, and Λ_2 is the integral through the outer (Ekman) layer. Note that each depends on η_*, but that the surface layer dependence is logarithmic, thus weaker. Λ_1 is also weakly dependent on u_*.

The buoyancy scale factor η_*, derived in McPhee (1981), is given by

$$\eta_* = \left(1 + \frac{\xi_N u_*}{R_c f L}\right)^{-1/2}$$

where $L = \varrho_0 u_*^3 / (gk < w' \varrho' >_0)$ is the Obukhov length and R_c is the critical flux Richardson number, equal to 0.2. η_* is 1 for neutral stability (no buoyancy) and less than 1 for all stably stratified flows. The buoyancy flux is approximately

$$\frac{g < w' \varrho' >_0}{\varrho_0} \cong g \alpha_S < w'S' >_0$$

where the thermal expansion term is neglected at low temperatures. From equation 2 and with the following: $\alpha_S = 8 \times 10^{-4} \ (\%o)^{-1}$, $g = 9.8 \ \mathrm{m \ s^{-2}}$, and $f = 1.4 \times 10^{-4} \ \mathrm{s^{-1}}$, the expression for η_* is approximately

$$\eta_* \cong \left[1 + a_1 \frac{w}{u_*^2}(S_0 - S_i)\right]^{-1/2} \tag{8}$$

where $a_1 = 5.6 \ \mathrm{m \ s^{-1}} \ (\%o)^{-1}$.

The effect of η_* on heat transfer is demonstrated as follows: let u_* be 0.01 m s^{-1}, and assume first that there is no surface buoyancy flux, so that $\eta_* = 1$. With $z_{OT} = 10^{-1}$ m (see discussion below), Λ_1 is 20.5 and Λ_2 is 10. If we now specify a melt rate of 50 cm da^{-1} ($w = 5 \times 10^{-6}$ m s^{-1}) and a salinity difference $(S_0 - S_i)$ of 25, then according to equation 8, $\eta_* = 0.35$. The change in Λ_1 (equal to 2 ln $[\eta_*]/0.4$) is about -5.2, while Λ_2 increases by 18.6. There is a significant net increase in Λ from the integral across the outer layer, and a corresponding 30% decrease in the heat transfer coefficient.

The temperature surface roughness, z_{OT}, warrants comment. In McPhee (1983), I equated it to the momentum surface roughness, z_0, which is relatively large under sea ice. George Mellor has pointed out that the fundamental processes that deterine z_0 include form drag forces across roughness elements, for which there is no analog in the heat transfer process. He suggests using $z_{OT} = \nu_T/ku_*$, where ν_T is the molecular thermal diffusivity. For $u_* = 0.01$ m s^{-1}, this puts z_{OT} at about

3×10^{-4} m. My intuition is that this underestimates z_{OT} in the complex under-ice environment, and that the value chosen above, namely 10^{-1} m, represents a compromise. Nevertheless, I now think that the value used in McPhee (1983), 0.05 m, is too large for z_{OT}, though not necessarily for z_0. For reference, making z_{OT} 30 times smaller in the example above adds about 8.5 to Λ_1, the surface-layer contribution to the boundary-layer integral, which is still considerably smaller than the buoyancy contribution.

Given surface stress $(\varrho_0 u_*^2)$, here is a method for estimating melt rate. First, estimate the change in temperature $(T_0 - T_\infty)$ and salinity difference $(S_0 - S_i)$, either directly or from T_∞ and S_∞ using equation 6. Initially, assume $\eta_* = 1$ (neutral conditions), and use equation 7 to calculate an upper bound for w, which is used in equation 8 to obtain a refined estimate of η_*. The procedure is repeated until the value for w converges to within some tolerance; in practice, this convergence occurs rapidly. Melt rate is $(\varrho_0/\varrho_i)w$. The following table shows the calculation for $u_* = 0.01$ m s^{-1}, $(T_0 - T_\infty) = 2°C$, and $(S_0 - S_i) = 25\%o$:

Iteration	η_*	Λ	$w(\times 10^5 \ \mathrm{m \ s^{-1}})$
1	1	30.5	1.09
2	0.25	53.6	0.62
3	0.32	46.2	0.72
4	0.30	47.8	0.70

Melt rate is about 67 cm/day.

This relatively simple calculation can furnish additional information, such as the depth to which the "melt-water lens" penetrates, which is $k \eta_* u_*/f$, or approximately 9 m. The technique may also be used to investigate ice drift and near-surface currents, but it is then probably easier to refer to the original similarity theory. A reader who has followed the arguments here will see that they are applied in the same way there, except that the scale factor is derived from more basic assumptions.

Note that melt rate calculated this way will persist only as long as heat is available. With "off-ice" advection, the leading ice edge will encounter warm water continuously, but trailing floes interact with water that has been cooled and undergo less melting. To treat the problem in any detail requires consideration of both time dependence and horizontal gradients, which add considerable complexity.

5

REFERENCES

Gill, A.E., *Atmosphere-Ocean Dynamics*, Academic Press, New York, 1982.

Josberger, E., Sea ice melting in the Marginal Ice Zone, *J. Geophys. Res.*, *88*, 2841-2844, 1983.

Josberger, E., Reply, *J. Geophys. Res.*, *89*, 761, 1984.

McPhee, M.G., Turbulent heat and momentum transfer in the oceanic boundary layer under melting pack ice, *J. Geophys. Res.*, *88*, 2827-2835, 1983.

McPhee, M.G., Comment on "Sea ice melting in the Marginal Ice Zone," by E.G. Josberger, *J. Geophys. Res.*, *89*, 759-760, 1984.

Kinematics of Marginal Ice: MIZEX 83

HAJIME ITO

Alfred-Wegener-Institut fur Polarforschung

The kinematics of the marginal ice zone, an important element in ice dynamics and hence in the air/ice/water system of the area, were studied in the Fram Strait, east of Greenland, as a part of MIZEX 83 (inset, Figure 1). The primary purpose of the work was as a pilot study for the main program in 1984 (Johannessen et al., 1983). Some interesting phenomena detected directly from the pilot study are presented in this article.

Ice margin

At the ice margin the frozen sea meets the open sea. The general characteristics of the transition are schematically described first. Two facts are essential to establish an ice margin. First, a quantity (for example, fish population, air temperature, floe diameter, to mention a few) that has a constant value, Q_1, (or changes its value linearly with distance) in the region far into the frozen sea. (In
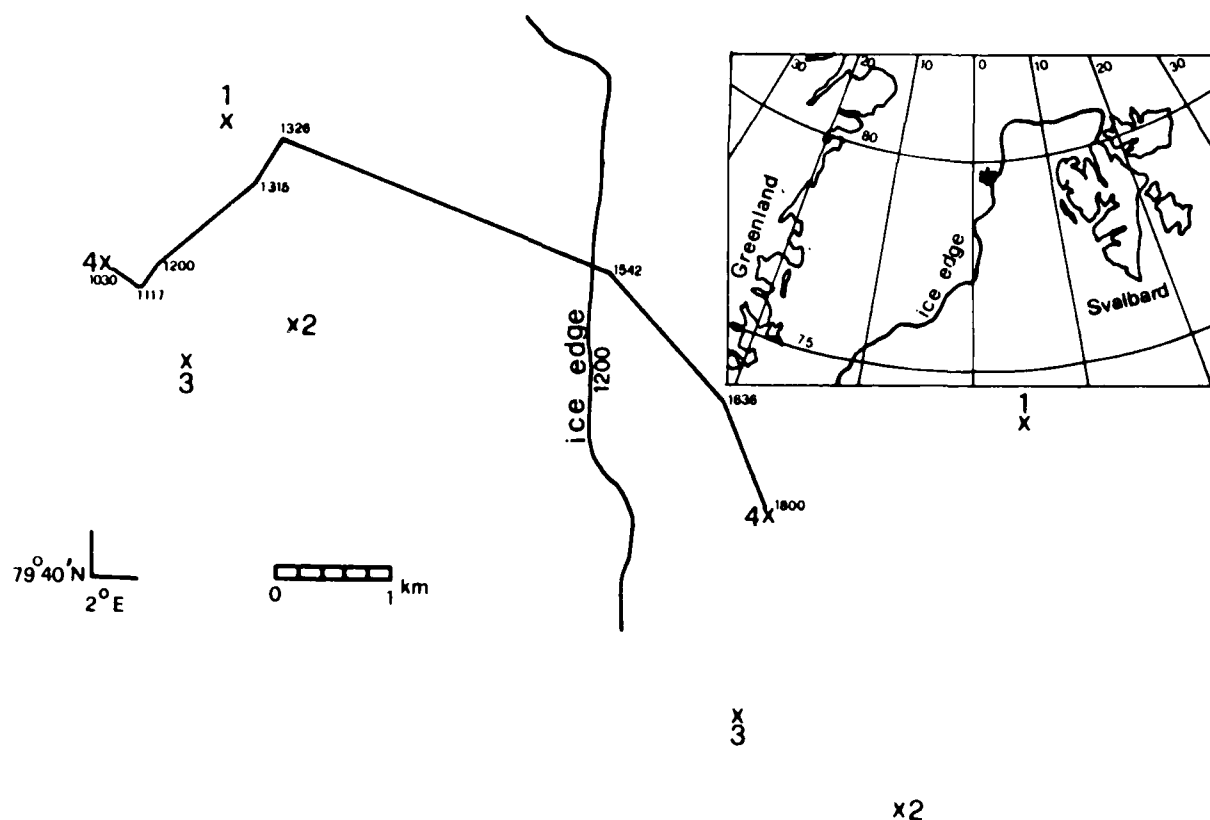

Fig. 1. Position of markers 1, 2, 3, and 4 at 1030 and 1800 GMT, 11 July 1983. The path line of marker 4 and the ice edge location at 1200 GMT are also shown.
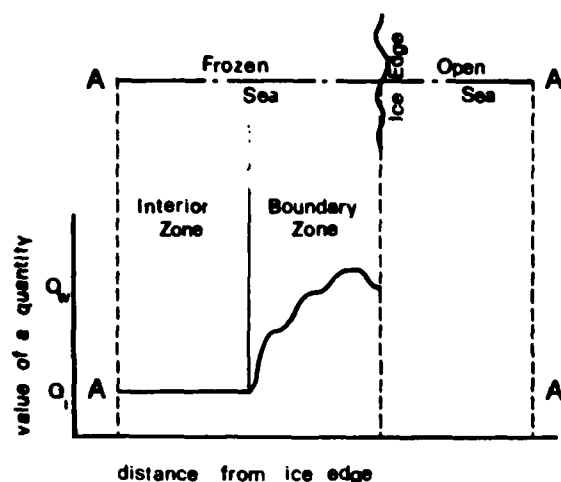
7

Fig. 2. Schematic transition from frozen sea to open sea.

the latter case, its gradient is used.) Such a place is called the "interior zone"—to be precise, an interior zone for the quantity—and it is almost always present, since the extent of the area is not restricted and in the extreme can be reduced to a line. Second, the value of the quantity must be prescribed at the ice/water boundary (i.e., the ice edge), Q_W (Figure 2).

There may be a "boundary" zone that connects the interior zone to the ice edge. How the quantity changes beyond the ice edge into the water is not of concern here; indeed, it need not even be defined over the open sea. The boundary zone thus has a secondary meaning to construct the ice margin, in the sense that a transition can also exist without the presence of a boundary zone (e.g., open water washing a solid fast ice field). Nevertheless, the boundary zone is most interesting. All behaviours that are associated with the ice/water transition can be expected to be present in the boundary zone in extreme form. The final purpose of this study is to obtain the actual shape of the profile over the boundary zone for the quantity in question.

More than one boundary zone can exist, possibly with intermediate interior zones in between. In that case the schema has only to be repeated; the treatment may become more complicated, but nothing essentially new is added. When the quantity is a tensor, the schema is applied on its components or on its invariants. The profile over the boundary zone can change its shape drastically with time, for each quantity in question and along the ice edge, while the basic schema is applicable throughout.

Measurement

Four markers, 1 through 4, were set on ice floes, and their relative positions were noted every 30 minutes during the time 1030 to 1800 GMT, 11 July 1983, by ordinary survey instruments (Theodolite Wild T2, Distomat Wild DI4L). The absolute position was also determined, but with much less accuracy, through the ship position and the compass. The positions of the markers at the first and last measurements are shown in Figure 1 with the path line of marker 4. The ice edge at 1200 GMT is also plotted in the figure (personal communication, Strübing). Since the ice edge also moved, none of the markers crossed the ice edge during the observation.

The accuracy of individual distance and angle measurements was estimated to be within 2 cm and 0.002 400° respectively. Due to the rapid movement (relative to the time required to complete a reading) and insufficiently accurate time determination, the positions of the markers are estimated to be correct within several meters relative to each other. The position of the markers relative to the earth is assumed to be reliable within hundreds of meters.

The time interval of the measurement was somewhat irregular, but the nominal time of 30 minutes is used throughout this article, except in the calculation of velocity, where the actual time interval was used.

The wind record for the day on the *Polarstern* is given below:

0000 GMT	280° from north	at 15 knots
0300	290°	at 13
0600	280°	at 15
0900	280°	at 12
1200	240°	at 12
1500	250°	at 12
1800	230°	at 07
2100	210°	at 12

The wind was constant during the measurement in terms of both direction and speed. Immediately before measurement started, the wind direction rotated counterclockwise by 40°. No information is available on the sea current behaviour for the day.

Analyses

Preliminary analysis showed that the classical or engineering treatment cannot be used because of the large deformation. More complicated methods of analysis (e.g., Truesdell and Toupin, 1960) have to be employed.

Frame. A moving two-dimensional cartesian frame was used to describe the present configura-
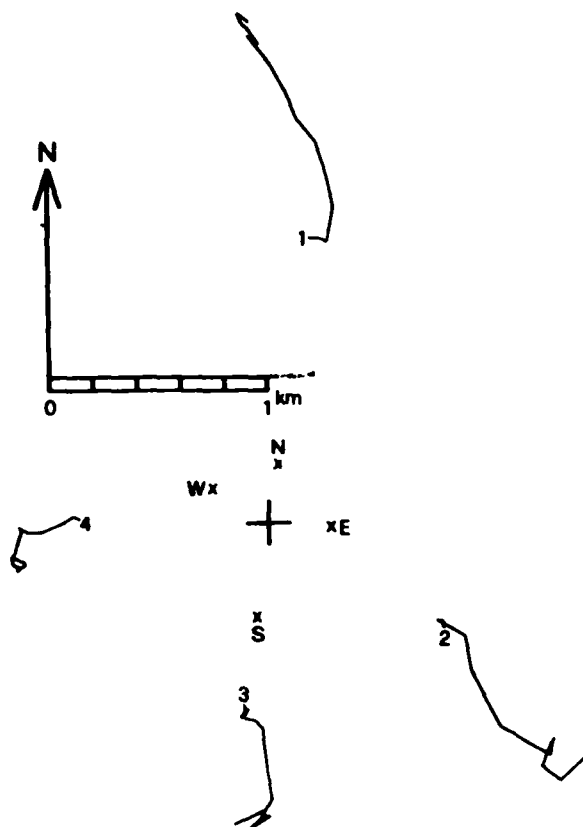
8

Fig. 3. Path lines of the markers in a moving frame (*). The movement started at the numbered end. Centers of four triangles (*), N, E, S, and W, are also shown. (* see definitions in text.)

tion. The movement of the frame was determined by two conditions: the origins of the frame's coordinates were always at the center of the four markers, and the sum of the directions from the origin to each marker (angles from an arbitrary but fixed direction) stayed constant. Such separation of rigid translation and rotation from the deformation is generally not essential but it was convenient for this particular study, as the positions had been measured with differing accuracy. The positions of the markers in this frame are shown in Figure 3.

Strain. The shape at 1030 GMT was taken to be the reference configuration. A set of three markers formed a triangle. There were four triangles. Under the linear assumption within a triangle, the deformation gradient was calculated and that value was attached to the center of the triangle (the centers of triangles N, E, S, and W at 1030 are shown in Figure 3). This procedure is not completely legitimate; two triangles had a common side or area, where two different linear fields were

assumed. Caution is therefore necessary in the discussion. Green's and Cauchy's deformation tensors, rotation tensors, principal axes, and the values for them (where applicable) and various invariants of them were calculated. Some of them will be shown during the discussion.

Strain rate. In addition, chronological linearity was assumed during the preceding 30 minutes to compute the velocity. That value was again attached to the ceners of the triangles and to the present time (neither 30 nor 15 minutes ago). Various tensors and invariants were computed in a manner similar to the strain computation.

Discussion

Rigid movement. The markers moved approximately in the direction of the wind with an average speed of 700 mh^{-1} until 1330 (Figure 1). Then they suddenly changed direction about 60° towards the right, and proceeded with a greater speed, 1200 m h^{-1} average, turning gently more to the right. The wind did not change direction (nor speed) throughout the measurement. The phenomenon indicates one or both of two possibilities: the sea current changed velocity at 1330, or the markers were transferred through their own movement relative to the zone boundary from one zone to another where different mechanisms governed. There is no means of checking the first possibility.

Rigid rotation is plotted in Figure 4. The field rotated at first counterclockwise then clockwise, both almost linearly, with an average angular speed of 8° h^{-1}. The two possibilities given above can also be applied to explain the sudden change in the rotating direction. The turning time was, however, 1.5 h earlier in this case. This favors the second possibility: The geometrical distribution of zones need not be the same for the translation and the rotation. Even if this were true, the sea current is not excluded from the discussion. The current may be an important element that specifies the characteristics of different zones. The rotation of the complete field to such an extent without any accompanying rotation in wind is in itself a very interesting phenomenon, and is probably related to the marginal eddies.

The rotation of individual floes differs from that of the entire field. For comparison, the observed rotation of a randomly chosen floe on which marker 4 was located is plotted in Figure 4. The curve is more irregular and changes value more violently, though somewhat systematically. It is an indicator of the local shearing in the neighbourhood of the floe.

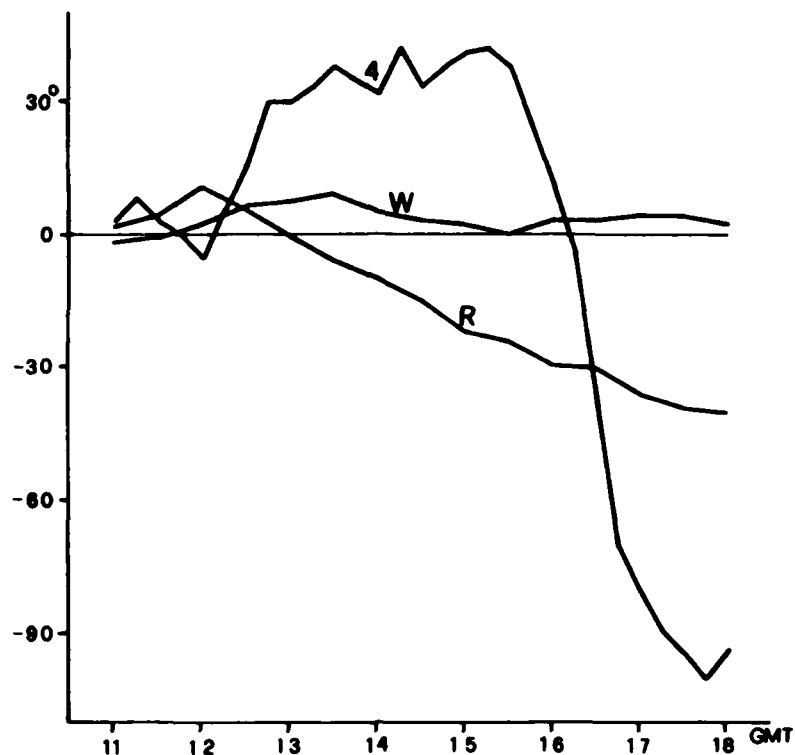The rotation tensor is an additional rotation of

Fig. 4. Rotation of the field, positive counterclockwise. R—rigid rotation of the observation area. 4—rotation of the floe on which marker 4 was located. W—rotation tensor of triangle W.

each individual triangle. The value was much less than the rotations mentioned above, and nothing particularly interesting was found. Triangle W is shown in Figure 4 in terms of angle, to indicate the magnitude.

Displacement. Two components of the deformation gradient are plotted in Figure 5. The area was inactive until 1200. This again suggests the transfer from one zone to another at this time (or a change in the sea current). Assuming that the inactive zone is the interior zone and the active one is the boundary zone, the extension of the latter can be estimated to be a couple of kilometers from the ice edge (see Figure 1). Remembering that the ice edge ran parallel to the Y-axis, the eastward and southward components of the displacement increased as the location moved to the east, closer to the ice edge, after the observation area entered into the boundary zone. Now the geometrical arrangement of the centers of three of the triangles was in the order W, N, E from west to the ice edge (triangle S is excluded here for the reason given below). Figure 5a shows the increment of the eastward component decreased at first from west to east and then, after 1430, increased toward the ice

edge. This apparent concave-convex transition is not essential, but is associated with the rotation.

Figure 5b shows that the increase of the southward component of the displacement was greater toward the ice edge all the time after 1200. The magnitude of the southward component, hence also the difference in magnitude among the different triangles, was larger than that of the eastward component.

Two other components of the deformation gradient are plotted in Figure 6 to show the change of the deformation along the ice edge. The behaviour of triangle S was quite different from that of the other three. The ice motion was by no means constant parallel to the ice edge, i.e. one-dimensional treatment and the concept of a "band" have to be abandoned. Figures 6a and b are similar to Figures 5a and b respectively, if the direction east (X) is replaced by south (-Y). Similar discussion is applicable. The movement of the ice margin is more obvious in the direction of its normal for an "observer," as it is visible for him, but the movement in the parallel direction is often more important. This general statement, accepted for a fixed boundary (wall) without question, is logically supported
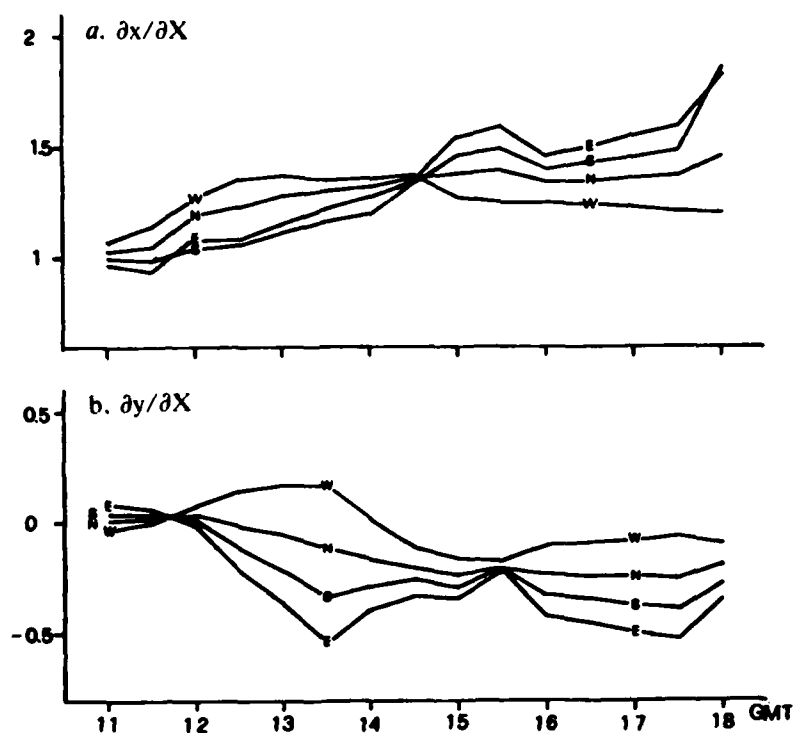
10

Fig. 5. X *components of deformation gradient. N, E, S, and W indicate the names of the triangles.* X: *reference coordinate.* x, y: *present coordinates.*
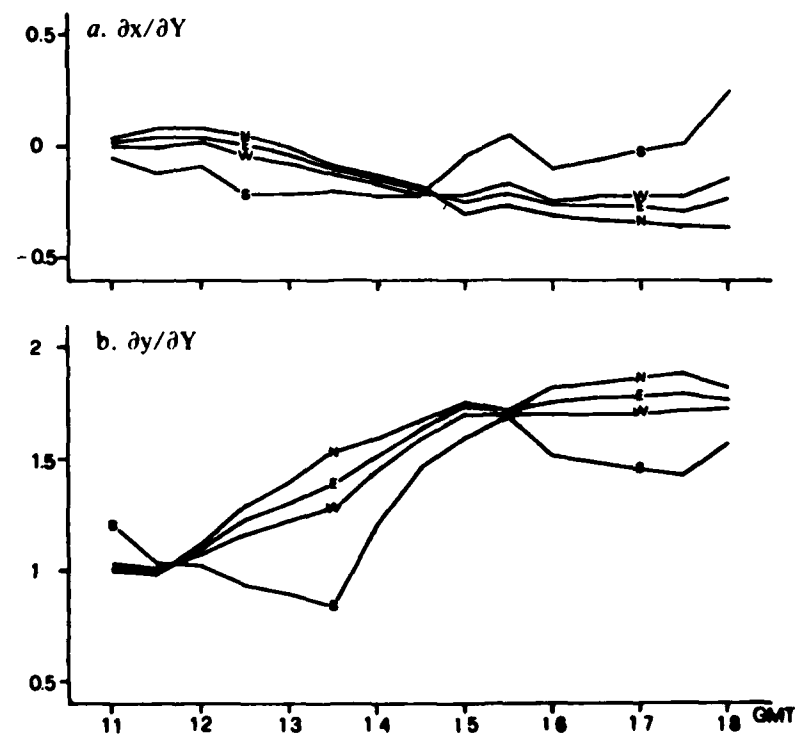

Fig. 6. Y *components of deformation gradient. N, E, S, and W indicate the names of the triangles.* Y: *reference coordinate.* x, y: *present coordinates.*
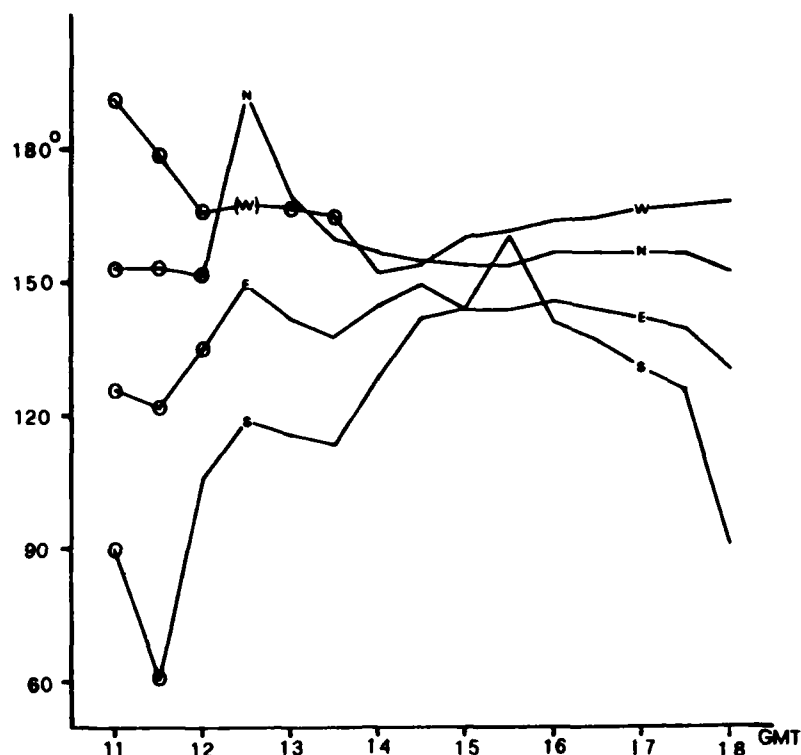
11

Fig. 7. Direction of the major principal axis of deformation, in degrees from north. Where circled, the value of the minor axis was used. N, E, S, and W indicate the names of the triangles.

in this particular case by the fact that the ice is transported from the Arctic Ocean to the south, not from Greenland to the east.

Deformation. Figure 7 shows the major principal axis of Green's deformation tensor, in terms of angle measured from north. The value of the minor principal axis was used in some places where indicated, so that the angle does not change abruptly by 90°. The angles were more or less constant, except for triangle S, but at different values for each triangle, smaller toward the east and south. The constant directions make the interpretation of the principal values, which are plotted in Figure 8, convenient. Exchange of major and minor values corresponds to the substitution of the angles mentioned above. The observation area was at first compressed in the direction given above, and then stretched for a much greater amount than before compression, either until the end of the measurement (N, E) or until 1500 GMT (W, S), when the deformation in the triangle was stopped.

The deformation in the minor direction indicates two different types. Triangles N and W were stretched and either immediately (N) or after compression (W) reached a constant value at 1200 or 1500 GMT respectively. The second type (E, S) was more complicated: small extension, large compression, large extension then compression to reach the same constant value as the first group.

There seems to be a zone where the extension prevailed in the direction 130° to 170° from north, the angle being smaller as the point moved to the east. Either this zone was periodically compressed for a short time, or the observation area entered this zone at 1130. Otherwise, the entire zone was stretched in that direction monotonically. Triangles W and S left the zone at 1500. At right angles to this direction the zone was also expanded, but to a lesser amount; the northwestern part was expanded more at first, while the southeastern part of the zone was compressed, then the roles were exchanged. It was a kind of wave propagation.
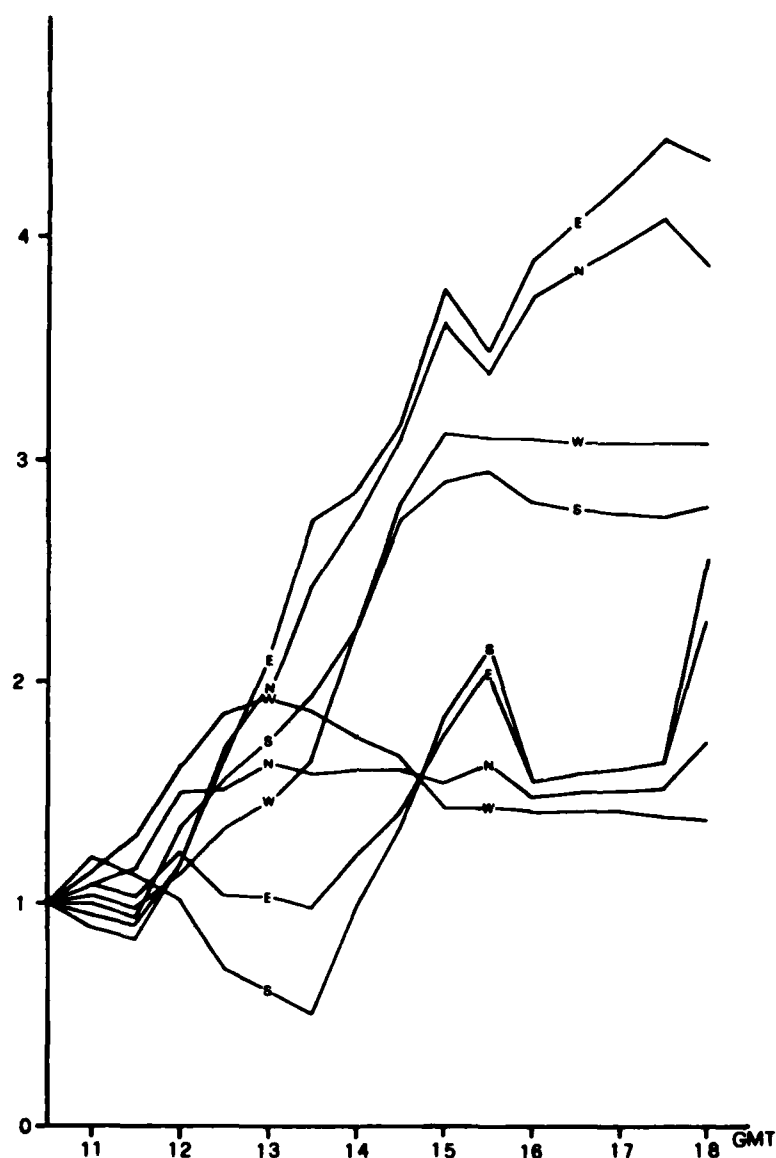
12

Fig. 8. Principal values of Green's deformation tensor, $C_1 = \lambda_1{}^2$,
$C_2 = \lambda_2{}^2$.

As a result, the areas of the triangles changed, as shown in Figure 9. The increase of the area started almost at the same time (1130, only S at 1330) and the rates were also similar to each other, but the increase was stopped at different times, W at 1430, N at 1500, and E and S at 1530. The area was increased to double or more through the stay in the zone for several hours, hence the ice concentration fell to less than half of its previous value.

Motion. A similar analysis was made for the strain rate as for the strain, but nothing very interesting was found. The reason for this disappoint-

ing finding must be the too large time interval in the measurement. For movement this rapid, the linearity assumption for 30 minutes was not allowed.

Principal stretchings are shown in Figure 10. The almost linear decrease in the major stretching of triangle E and the large repeated areal change rate of triangle S are some of the phenomena that it would have been interesting to study in detail, if more information had been available.

Directly measured maximum stretch in 1 hr was 1.291, and the computed maximum stretching was
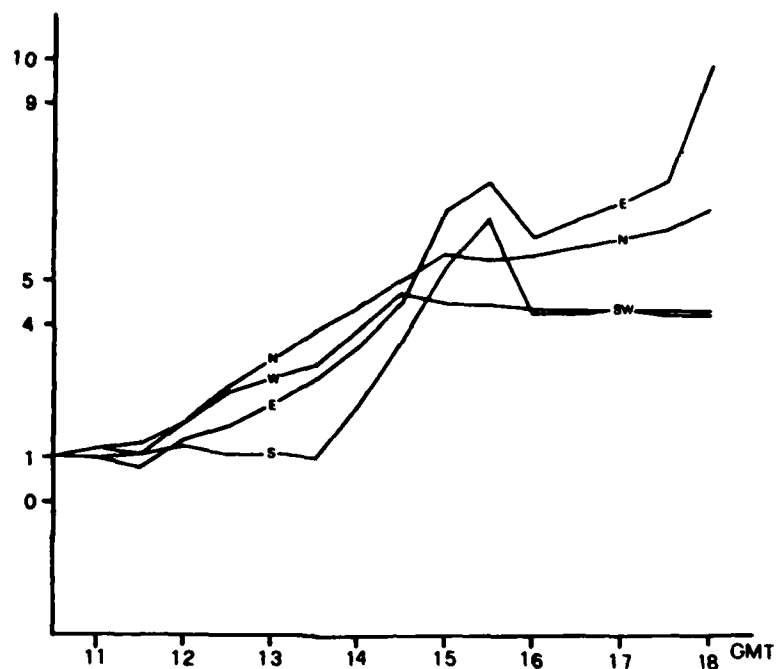
13

Fig. 9. Second invariant of Green's deformation tensor, $C_1 C_2 =$ $\lambda_1^2 \lambda_2^2 = (area)^2$. N, E, S, and W indicate the names of the triangles.
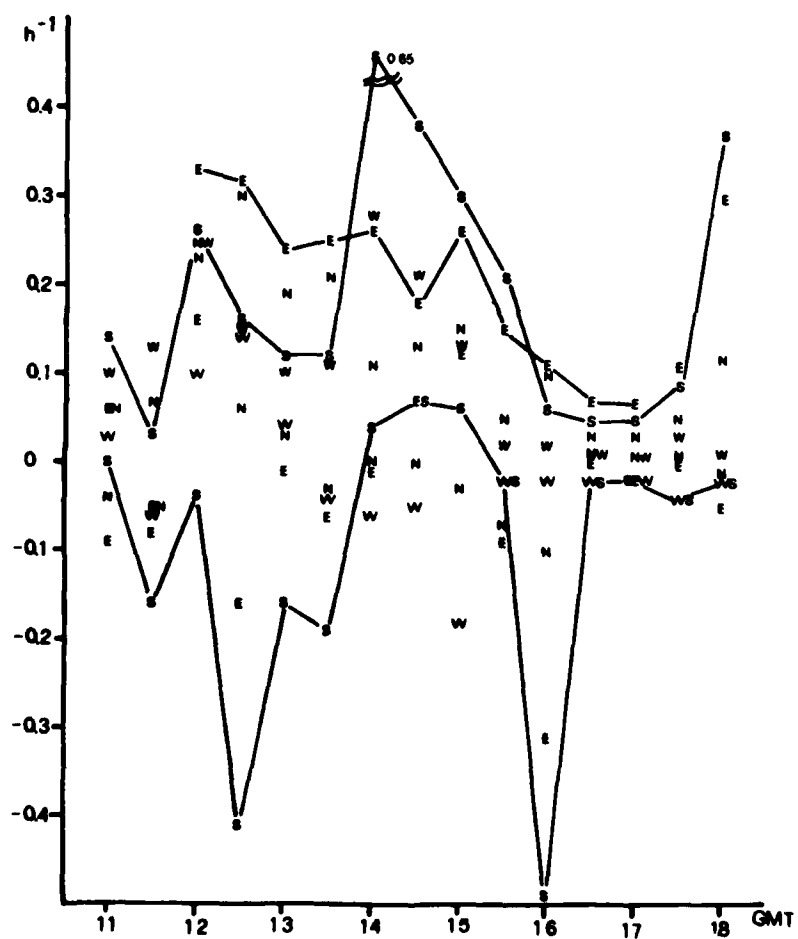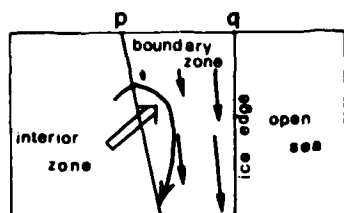

Fig. 10. Principal values of stretching tensor, d_1, d_2. N, E, S, and W indicate the names of the triangles.

14

a. Double arrow—basic move-
ment for entire ice field; solid
arrow—additional movement
available only in the boundary
zone; curved arrow—path line
of the observation area rela-
tive to the interior zone.

b. i—interior zone;
b—boundary zone;
c—chaotic zone;
p—front of interior
zone; p'—second
front; q—ice edge.

Fig. 11. Model of marginal ice.

0.652 h⁻¹. In comparison to the values obtained in AIDJEX (e.g., Pritchard, 1974) and the MIZEX-83 interior ice (e.g., Hibler and Lepparanta, 1984), the active motion at the ice margin is clearly indicated.

Model

The model was an attempt to reconstruct the movement of the ice field, explaining all the phenomena observed. With so little information in hand, great freedom is left in constructing a model of the marginal ice. A plausible structure is presented below, while many different schemas might suit the results as well.

The entire ice field moved approximately in the direction of the wind. It should not be understood from this that the coriolis force can be ignored. Many factors together, the wind being only one of them, moved the field in a direction that happened to be very close to the wind direction. Immediately at the ice edge, there was a boundary zone where additional southbound movement was overlapped (Figure 11a). The additional movement was variable within the zone: greater speed toward the ice edge and toward the south. The increase of the speed to the south was necessary to maintain continuity of ice transport in the zone, as the zone became narrow to the south (Figure 6b). The direction was not exactly parallel to the ice edge but was slightly inclined to the east. The tilt angle was smaller, because the point was located closer to the ice edge. Nevertheless the eastward component was greater toward the ice edge due to increasing speed (Figure 5a).

The observation area was in the interior zone at the beginning, and was transferred over line p into the boundary zone at 1130. The transfer was not made continuously but as a block. Through such an intermittent transfer, line p retreated relative to the material movement. Until the southward additional component increased sufficiently to overcome the northward basic component at 1330, the observation area continued to move northward. The turning of the path line (Figure 1) thus happened in the middle of the boundary zone and had no direct relation to the crossing of a zone boundary.

The interior zone rotated as a whole counter-clockwise, so that its front, line p, came to be at right angles to its movement. On the other hand, the boundary zone rotated clockwise so line p ran parallel to the ice edge, line q (Figure 4). The change of the rotation was encountered immediately upon crossing of line p.

All the triangles were stretched in the direction of the boundary zone movement (Figure 8). Through rigid rotation clockwise, triangles W and S went back to the interior zone at 1500, when the stretch stopped increasing. Along line p a strong local shearing force existed, which is noticed in the rotation of an individual floe (Figure 4), from 1200 (eastward crossing) and from 1530 (westward crossing).

The boundary zone was also stretched at right angles to the main direction discussed above, due to the increase of the eastward component toward the ice edge. As the eastward component was much smaller than the southward one, the corre-

sponding stretch was also smaller (Figure 8, minor values). The behaviour of the minor values also indicates that the shape of lines p and/or q was not steady but a wave propagated along them.

Where lines p and q meet, a chaotic zone is expected (Figure 11b). The irregular behaviour of triangle S may be explained by the fact that it lay closest to the chaotic zone and was influenced by the turbulence more than the other triangles. The seaward extension of the chaotic zone may have the shape of an eddy. The boundary zone in this model cannot be a boundary jet in the strict sense, as it is not a continuous stream but a chain of repeated schemata. The extension of line p (shown as p' in the figure) may form a secondary front.

No comment can be given from a single short observation, even if the model is a correct one, as to whether this kinematic situation is a common occurrence for the area. Furthermore, kinematic study alone cannot tell through which mechanism the movement was established.

Conclusions

Active marginal ice was found very close to the ice edge, which was a couple of kilometers wide and had a fine structure. Observations have to be made there, and in detail. The behaviour of the marginal ice was also different along the ice edge. One-dimensional analysis and related measurements should be abandoned. If the strain rate has to be measured, the time interval of succeeding readings must be short.

Acknowledgment

REFERENCES

Hibler III, W.D. and M. Lepparanta, MIZEX 83 mesoscale sea ice dynamics: Initial analysis, *MIZEX Bulletin IV,* USA Cold Regions Research and Engineering Laboratory, Special Report 84-28, pp. 19–28, 1984.

Johannessen, O.M., W.D. Hibler III, P. Wadhams, W.J. Campbell, K. Hasselmann, I. Dyer and M. Dunbar, MIZEX, A program for mesoscale air-ice-ocean interaction experiments in arctic marginal ice zones, II. A science plan for a summer marginal ice zone experiment in the Fram Strait/Greenland Sea: 1984, *MIZEX Bulletin II,* USA Cold Regions Research and Engineering Laboratory, Special Report 83-12, 1983.

Pritchard, R., What? Strain? What strain?, *AIDJEX Bulletin, 26,* 59–74, 1974.

Truesdell, C. and R.A. Toupin, The classical field theories, in *Handbuch der Physik,* edited by S. Flugge, vol. III/1, Springer Verlag, Berlin, 226–783, 1960.

On Estimating Ice Stress from MIZEX 83
Ice Deformation and Current Measurements

M. LEPPARANTA
Institute of Marine Research
P.O. Box 33, 00931 Helsinki, Finland

W.D. HIBLER III
U.S. Army Cold Regions Research and Engineering Laboratory
Hanover, New Hampshire 03755-1290

O. JOHANNESSEN
University of Bergen, Bergen, Norway

It has become fashionable to describe sea ice in the marginal ice zone as drifting freely, mainly in response to wind current and wave effects. Observations of the deformation field and associated currents taken during MIZEX 83, however, give quite another picture in which the internal ice stress is not insignificant. In particular during the ice station phase of the MIZEX 83 East Greenland experiment, the pack ice was quite compacted and the resulting deformation field was rather damped. If ice interaction played no role, we would expect the ice to continue converging forever under compacting winds. What seems to happen instead is that once the ice reaches a certain compact state, it ceases converging due to the ice interaction and there is a concomitant reduction in the amount of shearing. Moreover, initial analysis of MIZEX 84 data shows this more compact state to be associated with both greatly reduced fluctuations in the deformation signal and less floe rotation.

During the 1983 experiment we were fortunate enough to have simultaneous current measurements at the three outer vertices of the deformation array (O, C, and J in Figure 1). Currents were measured at several levels at 10-minute intervals, and deformation was recorded at 3-minute intervals with a better-than-1-m accuracy using a Del Norte radar transponder system (for a more complete description of the deformation data, see Hibler and Lepparanta, 1983). Over much of this period the winds were relatively weak, so currents supplied the main motive source for the ice. Moreover, analysis of the relative currents between the

floes shows the ice typically remains "locked up," even though the relative currents can be substantial and even though the whole region may be drifting in an absolute sense with the currents.
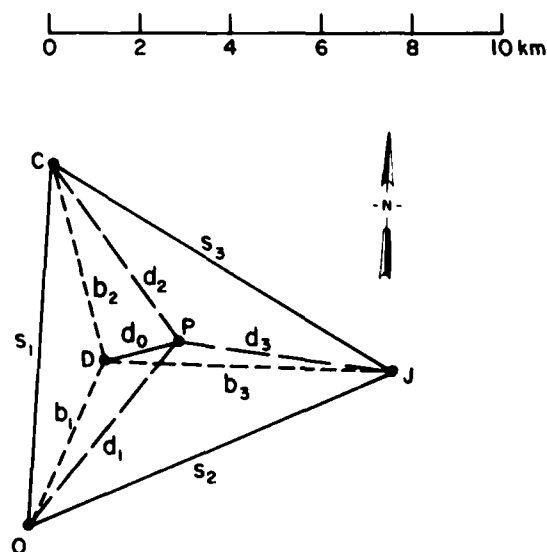

Fig. 1. *Configuration of strain array and nomenclature for distances discussed. The triangle is plotted to scale for 29 June 0800 GMT; the ship (M/V Polarbjórn) is located at the center point P moored to an ice floe. Del Norte units are located at solid points. Directly measured distances (accurate to 1-2 m) are denoted by subscripted b's and d's and distances calculated by triangulation (less accurate depending on geometry) are denoted by subscripted s's.*
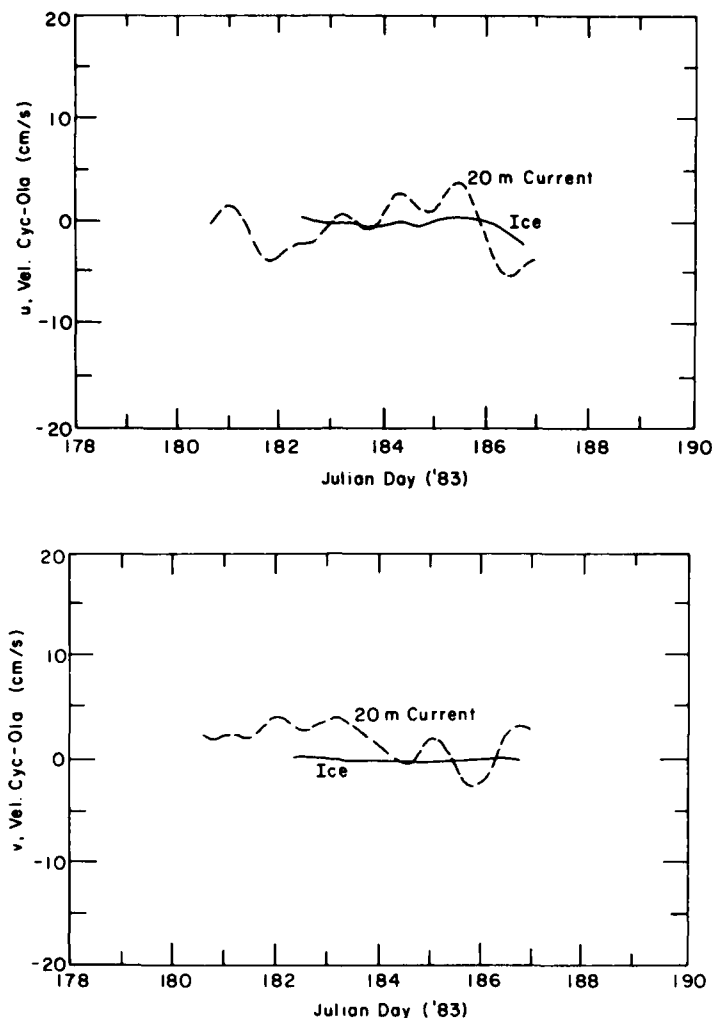
17

*Fig. 2. Time series of smoothed relative currents and relative
ice motion between stations O and C.*

Such behavior is quite consistent with plastic models (see, for example Lepparanta and Hibler, 1985), but not with simple pressure-term-only rheologies (e.g. Röed and O'Brien, 1983). Within the framework of a plastic rheology, this situation affords enough information for a lower bound estimate of the stress in the ice. Basically, under relative rigid conditions the rigid state of plasticity takes the appropriate stress state necessary to absorb differences in the body forces (in this case the water drag), as long as these stress states do not exceed the plastic limit.

A typical situation of this nature that occurred is shown in Figure 2 where we have plotted the ice motion and ocean current differences between sites C and O over a period of several days. These data have been somewhat smoothed by filtering

but that does not affect the argument. As can be seen from this figure, the relative currents are quite substantial whereas the ice is essentially locked up. This "locked up" state is hard to justify by different drag coefficients, since the same relative rigid conditions occur for both divergent and convergent motion.

Based on this figure the relative currents have a maximum value on the order of 5 cm s^{-1}, and the distance between the sites is on the order of 10 km. If σ_1 is the stress at one site, then, assuming all variables vary linearly over the deformation array, to prevent ice motion σ_2 must be at least $\sigma_1 + \Delta\sigma$ where $\Delta\sigma/\Delta x$ equals the differential ice water stress between the two sites. To obtain the water stress precisely would require knowledge of the absolute currents, but as a crude estimate we take

18

the absolute current to be 0 at one site. Therefore, taking a quadratic water coefficient of 0.0055, the water stress differential is

$$0.0055 \varrho_w (0.04)^2 = 0.0055 \cdot 10^3 \cdot 1.6 \cdot 10^{-3}$$

$$= 8.8 \cdot 10^{-2} \text{ Nt m}^{-2}$$

$$\therefore \Delta\sigma = 8.8 \cdot 10^{-2} \cdot 10^4$$

$$= 10^3 \text{ Nt m}^{-1}.$$

While this value is smaller than typical strengths used in large-scale plastic models (see e.g. Hibler and Walsh, 1980) on the order of 10^4 to 10^5 Nt m^{-1}, it is by no means trivial. It is clear from the estimation procedure that this value depends on the spacing between the points. To support the same current differential over a larger region, the stress must vary a larger amount. This is in fact one reason why, on a larger scale, a plastic system will deform as if it were in free drift, whereas smaller sections can be relatively rigid.

While the estimates made here are crude, they do give an idea of the plastic stresses that can be expected in the marginal ice zone. These comparisons also indicate that ice deformation provides a much more sensitive test between ice drift theories than ice trajectories.

REFERENCES

Hibler, W.D. III and J. Walsh. On modeling seasonal and interannual fluctuation of Arctic sea ice, *J. Phys. Oceanogr., 9(12)*, 1514-1523, 1980.

Hibler, W.D. III and M. Lepparanta. MIZEX 83 mesoscale sea ice dynamics: Initial analysis, *MIZEX Bulletin IV,* USA Cold Regions Research and Engineering Laboratory, Special Report 84-28, pp. 19-28, 1984.

Lepparanta, M. and W.D. Hibler III. The role of plastic ice interaction in marginal ice zone dynamics, *J. Geophys. Res., 90,* 11899-11910, 1985.

Røed, L.P. and J.J. O'Brien. A coupled ice-ocean model of upwelling in the marginal ice zone, *J. Geophys. Res., 88,* 2863-2872, 1983.

Crystal Structure of Fram Strait Sea Ice

A.J. GOW, W.B. TUCKER III AND W.F. WEEKS

U.S. Army Cold Regions Research and Engineering Laboratory
Hanover, New Hampshire, U.S.A.

During June and July 1984, sea ice physical property investigations were conducted from the FS *Polarstern* during MIZEX-84. A large area within the Fram Strait was traversed by *Polarstern*, providing an opportunity to obtain core samples that very likely had originated in different parts of the Arctic basin. Ice cores were taken at the locations shown in Figure 1. For each core we measured temperature and salinity profiles and documented the crystal structure through the thickness of the ice floe. Figure 2 shows an exam-

ple of our characterization method applied to a core taken through undeformed multi-year ice. In this paper, we wish to report on specific examples of the crystal structures observed on MIZEX and to discuss the origin of these textures with regard to the ice growth and ablation processes. First, however a general description of sea ice growth is presented as background for later discussion of the crystal structure.

Sea ice formation typically begins with the free growth of crystals in a slightly supercooled water
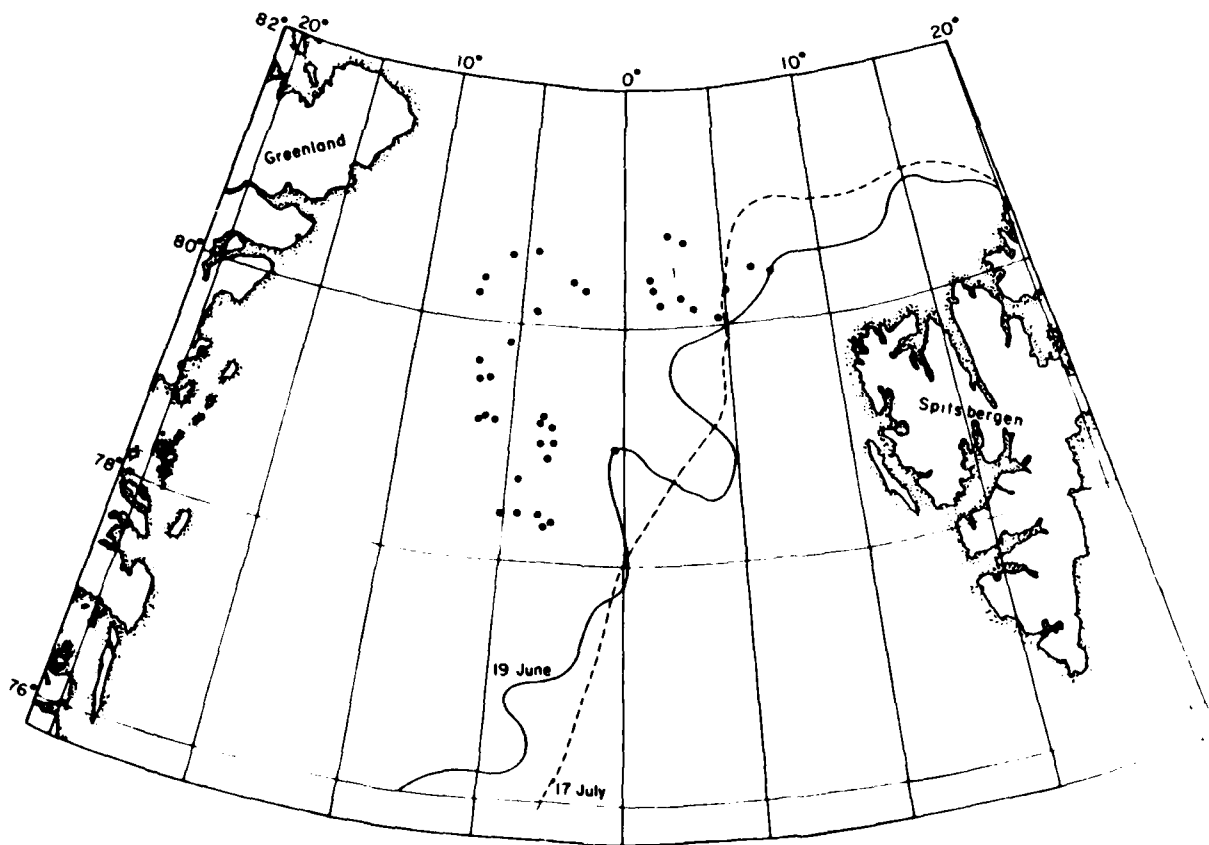

Fig. 1. Ice properties sampling locations. Approximate ice edge locations for 19 June and 17 July 1984 are also shown.
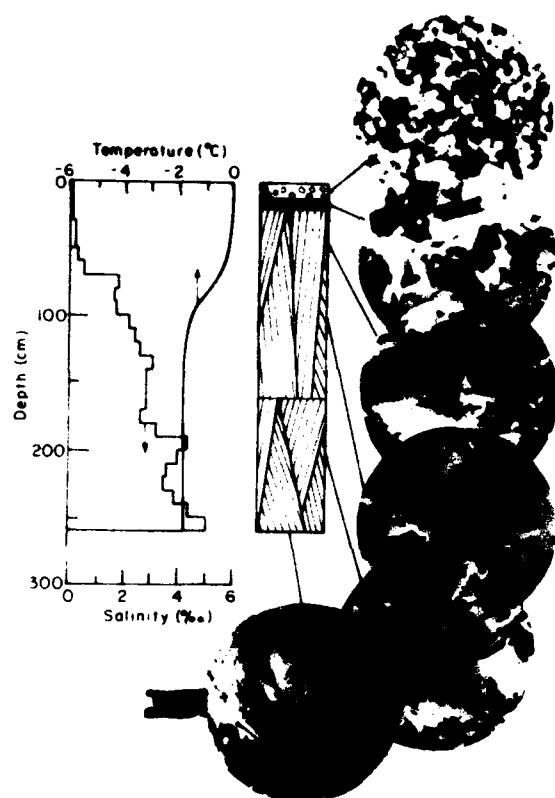
Fig. 2. Typical properties and structural profile of multi-year sea ice composed of 90% congelation. Columnar ice overlain by granular ice and a refrozen melt layer.

column. This initial growth usually occurs in the form of minute spheres, which rapidly change to discs that typically grow to diameters of 2 to 3 mm (Weeks and Ackley, 1982). The discs then evolve into hexagonal dendritic star-like crystals that are much more effective at dissipating heat and solute into the surrounding liquid. If the water remains calm, the crystals tend to float with their basal planes parallel to the water surface with the result that when they freeze together to form a surface skim, the crystals become oriented with their c-axes vertical. This is rarely the case, however, because freezing most commonly occurs under turbulent conditions (wind- or wave-induced) that cause many crystals to be trapped with their c-axes at various inclinations from the vertical. Generally this surface layer of frazil or granular ice grows no thicker than a few centimeters, but the action of stronger winds and waves can result in accumulations of frazil up to 1 m thick.

Once a stable surface layer of ice is established, growth of columnar crystals begins. This appear-

ance of a new crystal form marks the transition to congelation growth, the direct freezing of seawater to the bottom of the existing ice sheet. This transition generally occurs within 5 to 10 cm of the surface, but in some instances may extend to 50 cm deep.

Congelation growth typically produces vertically elongated columnar crystals that can be tens of centimeters long but usually do not exceed 2-3 cm in cross-sectional diameter. The c-axes of these crystals themselves also possess a cellular substructure consisting of vertical plates 0.5-1 mm thick, separated by parallel layers of brine inclusions. The platelets consist of essentially pure ice with the characteristic salinity arising from the brine incorporated between the plates. Such structure reflects the morphology of the growing interface, which consists of pure ice dendrites protruding vertically downwards into the sea water. Some of the brine excluded during freezing is trapped in the grooves between the dendrites as the growth interface advances. The initial salinity of the ice, which is determined by the amount of entrapped brine, has been shown to be inversely proportional to the brine layer spacing (Nakawo and Sinha, 1984). The layer spacing, in turn, is related to the growth rate such that the faster the growth, the closer the spacing and thus the saltier the ice, and vice versa. Once the initial salinity of the ice has been established, subsequent changes are determined essentially by the thermal history of the ice. Temperature variations cause changes in the geometry and distribution of the brine inclusions. The largest effect is the formation of brine drainage systems, vertical tubes with diagonal feeder channels made up of coalesced brine inclusions. The formation of these drainage systems is always associated with significant warming of the ice. Changes in crystalline texture may also accompany desalination, and the combination of all these effects generally leads to significant modification of the mechanical and electromagnetic properties of the ice.

What we have described above is the classical growth sequence of sea ice. However, there can be deviations from this norm, including the occurrence of frazil or granular ice at levels in the ice that are unrelated to surface turbulence effects. Our preliminary MIZEX findings (Tucker et al., 1985) indicated that 24% of the total ice sampled consisted of granular ice, mainly frazil, but also including snow ice, necessarily limited to the surfaces of floes. Most of this frazil was found in cores taken from previously deformed ice, e.g., in ridged ice. Generally, granular ice was restricted to frazil occupying the voids between the inclined
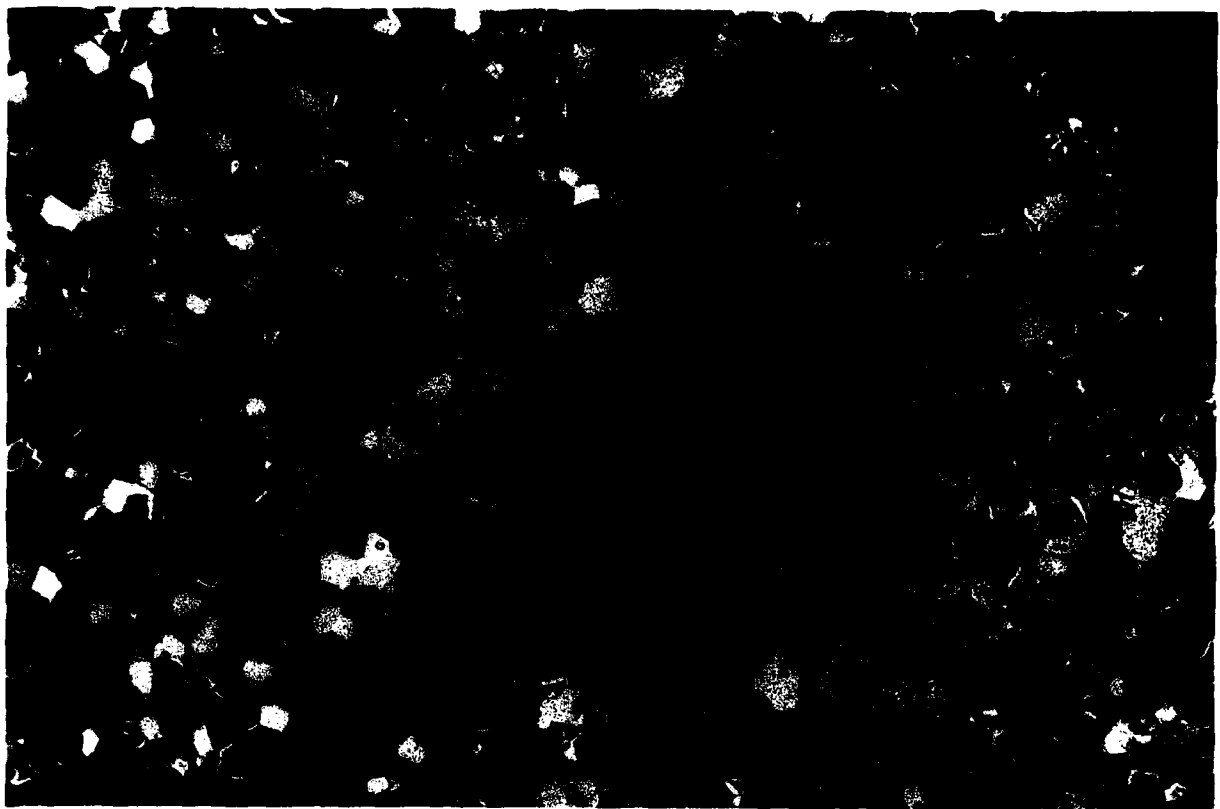
21

Fig. 3. *Horizontal thin section of fine-grained frazil from a depth of 300 cm in a multi-year ridge. Scale measures in centimeters and millimeters.*
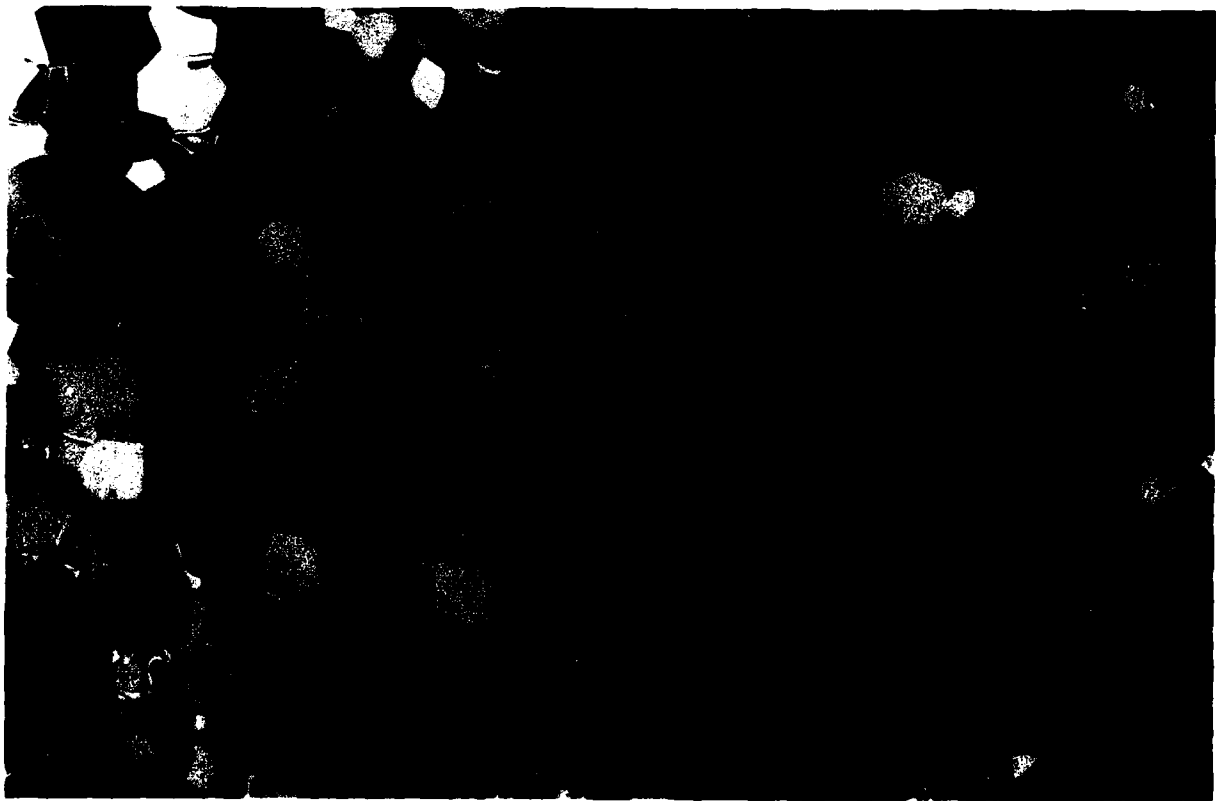

Fig. 4. *Horizontal thin section of snow ice at 3-cm depth in first-year ice. Scale measures in centimeters and millimeters.*

blocks in the ridges. We speculate that freezing nuclei, consisting of snow or crushed ice, precipitated the formation of frazil crystals in the voids. In constrast to the small amounts of frazil observed on MIZEX, Gow et al. (1982) found large accumulations of this ice type in Weddell Sea ice. Frazil ice made up 60% of the total ice sampled and was observed in both first- and multi-year ice and occasionally in thicknesses exceeding 3 m. Apparently, environmental conditions linked closely to the depth and structural characteristics of the oceanic mixed layer are more amenable to frazil formation in the Weddell Sea than in the Arctic basin.

We have used both horizontal and vertical thin sections to examine ice structure. Thin sections were prepared from cores using microtome sectioning techniques described in Weeks and Gow (1978). The structural plates shown here were obtained by placing the thin sections between crossed polaroids and photographing them in transmitted light. This technique, which utilizes the principle of interference colors, clearly reveals individual crystal boundaries, brine drainage channels, and the brine lamallae/platelet substructure of individual crystals. Color photographs (slides) were orig-

inally made with a 35-mm camera using Kodachrome® 200 ASA color slide film at aperture settings ranging from F8 to F126 at a 1-second shutter speed. The slides were then used to prepare the color internegatives needed to produce the color prints shown here. Black and white photographs were taken with a 10- by 12.5-cm press camera set up to provide negatives at approximately a 1:1 scale. The Kodak Plus-X-Pan® film used for this purpose was exposed for about 0.5 second at an aperture setting of F8.

Figures 3 and 4 illustrate two varieties of granular ice. The ice in Figure 3 consists of very fine-grained frazil that was located at a depth of 300 cm in a multi-year floe. Inclined columnar ice both above and below the frazil indicate that it formed in the void between blocks in a pressure ridge. Figure 4 features a much coarser-grained type of ice consisting of crystals with polyhedral outlines. This is snow ice, formed by the freezing of water-saturated snow. This is further confirmed by its occurrence at the top of the floe and by the fact that its salinity was less than 0.5‰.

Refrozen melt ponds were found to have crystal textures that are very similar to those observed in ice formed on freshwater lakes. Figure 5 shows

Fig. 5. Horizontal thin section of melt pond ice from 7-cm depth in multi-year sea ice. Scale measures in centimeters and millimeters.

23

typical melt pond crystal texture as observed in a horizontal section. Grain cross-sectional diameters up to 1 cm are commonplace and the *c*-axes are randomly distributed in the horizontal plane. The location of this section was 7 cm below the top of the melt pond on a multi-year floe. The salinity at this depth measured less than 0.2‰. The vertical section of this ice (not shown here) displayed a columnar texture with vertically oriented crystals. A much more dramatic example of melt pond structure is shown in Figure 6, a vertical sec-
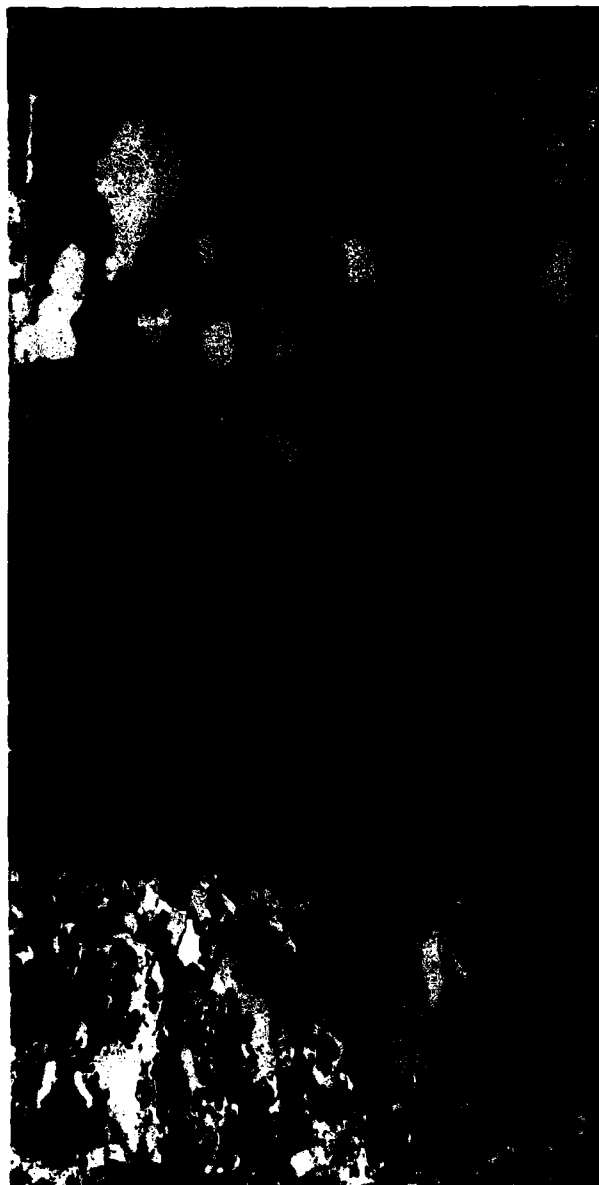

Fig. 6. Vertical thin section through a melt pond from the ice surface to a depth of 15 cm in multi-year ice.

tion of the top 15 cm from a different multi-year floe. Here a 5-cm-thick layer of snow ice, made up of large, randomly oriented crystals, overlies a melt pond exhibiting *c*-axis vertical melt crystal structure. The individual crystals here are very large, the result of slow freezing of the water. Gow (1984) points out that the type of crystal structure occurring in lake ice covers is determined by whether or not the lake water is seeded at the onset of freezing. Seeding leads to the growth of columnar, *c*-axis horizontal crystals, and unseeded (spontaneously nucleated) growth promotes the formation of massive, *c*-axis vertical crystals. The same is also true of melt ponds freezing on the tops of multi-year sea ice floes. Beneath the melt-pond ice, a sharp transition to columnar sea ice is evident.

As with granular ice, a variety of columnar ice forms were observed on MIZEX. Figure 7 shows columnar ice in horizontal section in which the *c*-axes are not only horizontal but are all very nearly aligned in the same direction. (In columnar sea ice the *c*-axes are normal to the long dimensions of the crystals.) This particular section was prepared from multi-year ice at a depth of 203 cm. In sharp contrast, Figure 8 shows a section from near the bottom of a 236-cm-thick first-year floe. In addition to exhibiting a variety of crystal sizes and shapes, very little crystal alignment is observed here. Weeks and Gow (1978, 1980), on the basis of measured and inferred current direction, believe that the alignment of crystal *c*-axes is controlled by the direction of the current at the growing interface. This control of current directions on the *c*-axis alignments in sea ice has now been verified in a series of laboratory experiments by Langhorne (1983). A likely explanation is that a current moving across (parallel to the *c*-axes), rather than parallel to the protruding dendrites (normal to the *c*-axes) presumably provides more effective heat transfer away from the dendrites, resulting in a growth advantage. Strong horizontal alignments would indicate that the ice had remained in a fixed position relative to the steady current direction. A weak alignment or lack of alignment implies that the ice, if in fixed position, must have grown in an area of highly variable current directions or, in the case of drifting pack ice, must have been rotating as it drifted.

Figure 9 shows much finer grained columnar ice than either of the previous two figures. We do not fully understand all the processes controlling the crystal size of columnar sea ice, but we speculate that the freezing rate of the sea water must be an important factor. Note also in this fine-grained ice
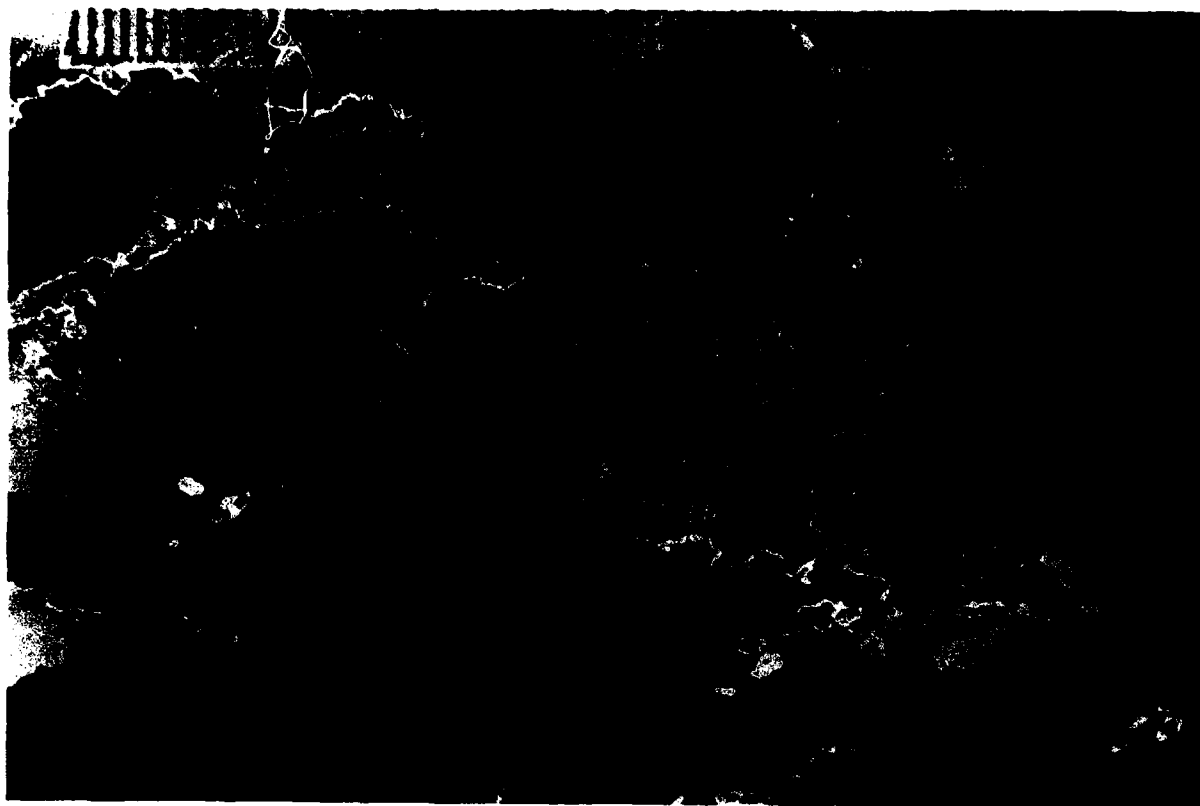
24

Fig. 7. Horizontal thin section of aligned columnar ice from a depth of 203 cm in multi-year ice. Scale measures in centimeters and millimeters.
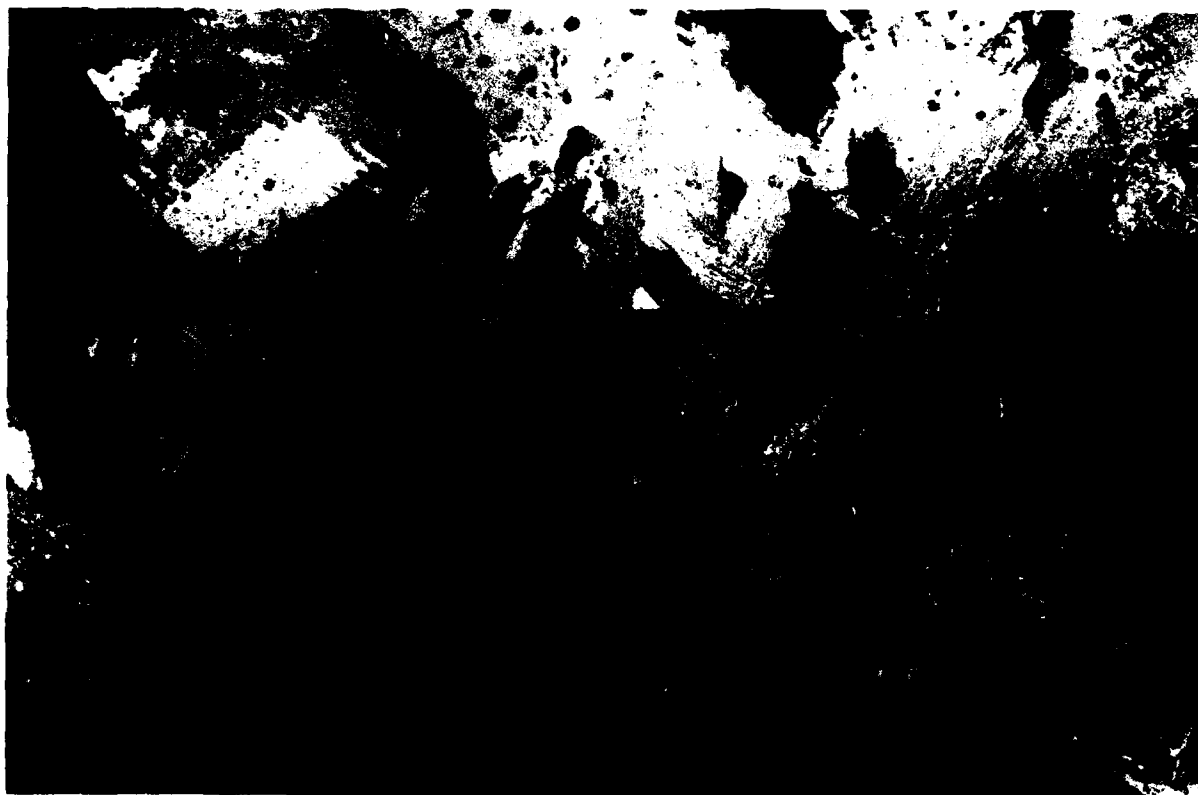

Fig.8. Horizontal thin section of unaligned columnar ice from the bottom of a 236-cm first-year floe. Scale measures in centimeters and millimeters.
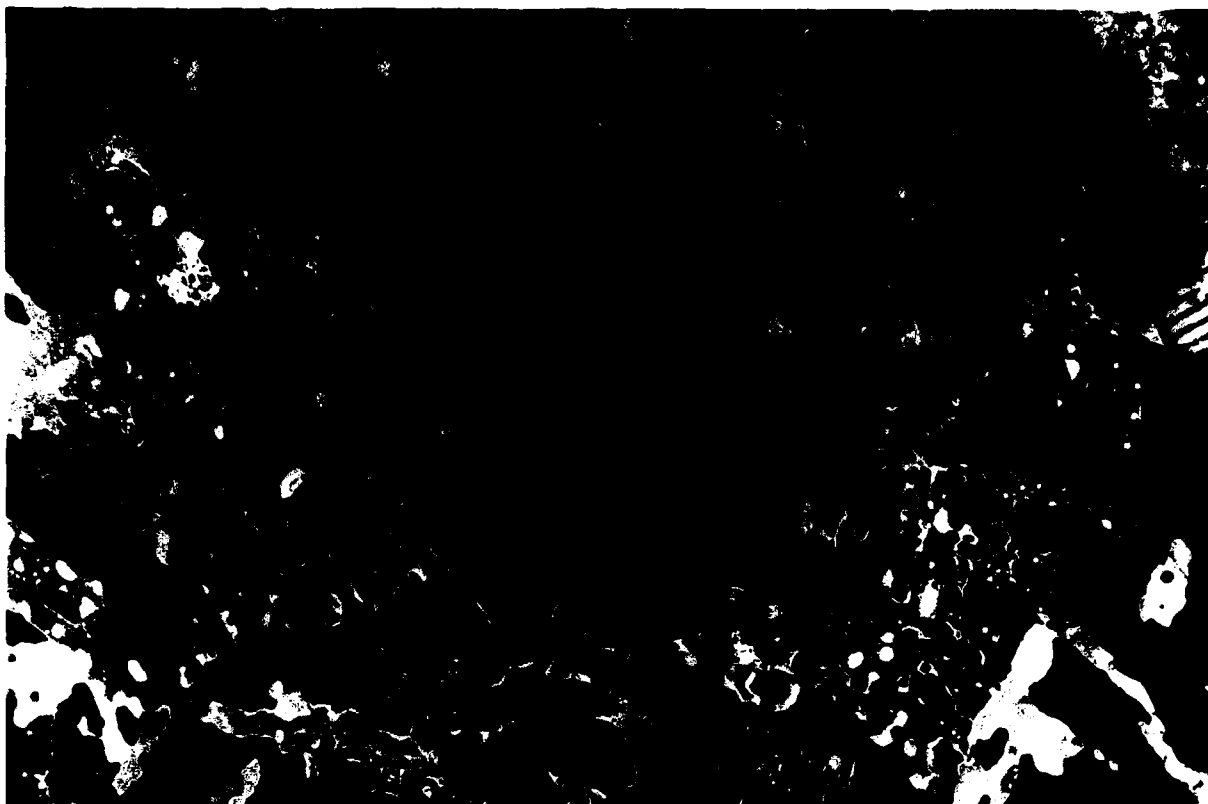
25

Fig. 9. Horizontal thin section of fine-grained columnar ice from a depth of 225 cm in multi-year ice. Scale measures in centimeters and millimeters.
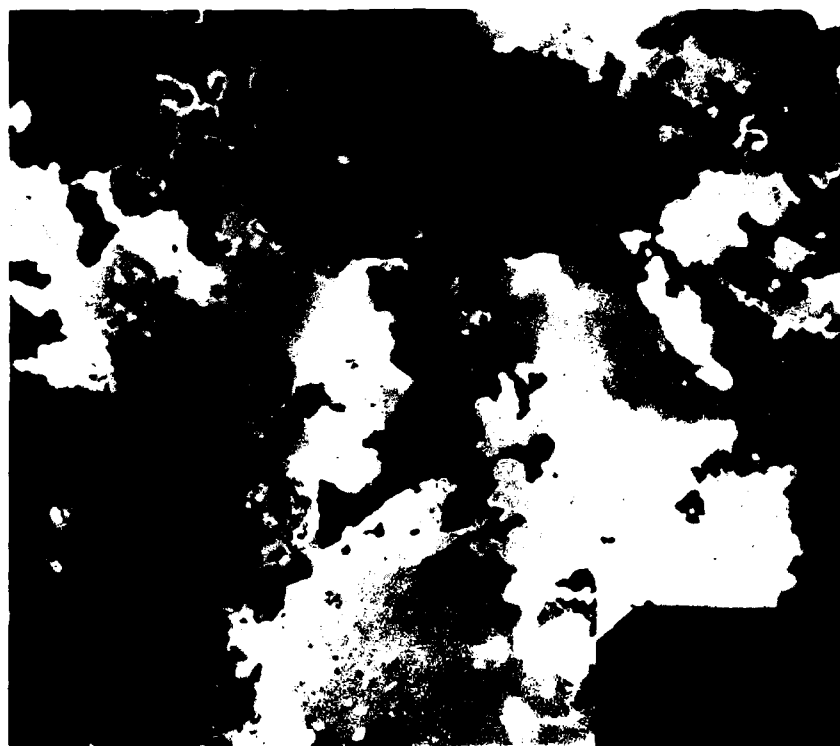

Fig. 10. Horizontal thin section of retextured columnar ice from a depth of 15 cm in multi-year ice. Scale measures in centimeters and millimeters.

26

the absence of any significant alignment of the crystals. This section of ice was obtained from a depth of 225 cm in a multi-year ridge fragment.

One of the more interesting structures, which to our knowledge has not been previously reported, is shown in Figure 10. Ice in this thin section, from a depth of 15 cm in a multi-year floe, shows considerable modification of its structure due to elevated temperatures during the previous summer. The more obvious structural modifications include nearly complete obliteration of the original ice platelet/brine lamallae substructure and substantial smoothing of the grain boundaries. Although there appear to be no significant changes in the overall crystal lattice structure, as evidenced by the retention of an original c-axis alignment, this retexturing always accompanies other changes in the physical properties of the ice. For example, it 1) is invariable associated with ice of very low salinity (less than 0.5‰), and 2) is restricted to the top meter of multi-year ice. The ice is much less opaque (often semi-transparent) in appearance and is much more resistant to drilling and sawing than ice from the same depth in a first-year floe.
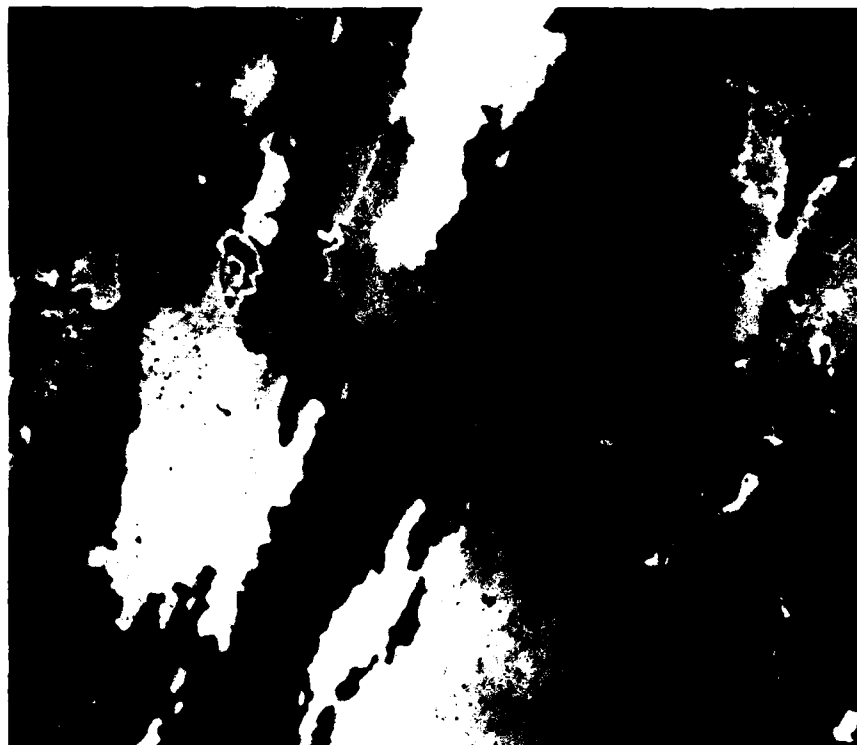
Although the sequence of horizontal thin sections in the multi-year profile in Figure 2 clearly indicates some diversity of crystal structure, evidence for retexturing of the ice is best observed in magnified sections, such as those shown in Figure 11. These sections were obtained from depths of 20, 93, and 192 cm respectively, in a 294-cm-thick floe that was very similar structurally to that shown in Figure 2. Vertical sectioning of the floe verified that it consisted entirely of congelation (columnar) ice.

In ice from 192 cm (Figure 11c), crystals are still interpenetrated structurally and still retain the well-defined platelet/brine lamalla substructure so characteristic of congelation ice. However, the salinity—2.5‰—clearly indicates some loss of the originally entrapped brine even at this level in the floe. Since this floe was 294 cm thick, it is very likely that ice now at 192 cm was formed two winters ago but was located deep enough in the floe to protect it from the dramatic effects of surface warming during the intervening summer (1983). However, this situation is not true of ice at 93 cm (Figure 11b) where only vestiges of the original ice
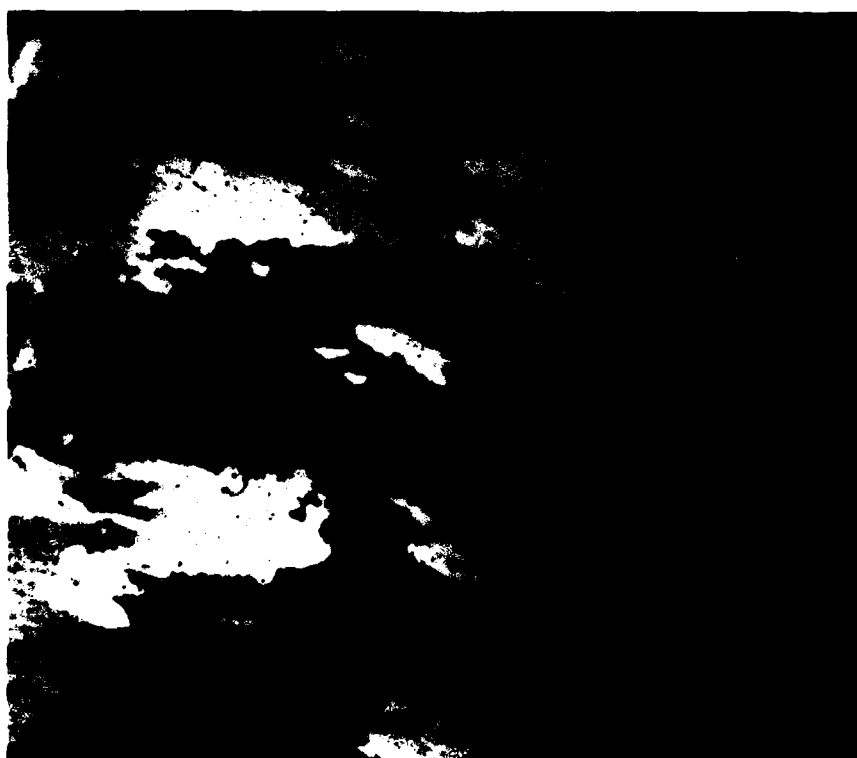

a. 20 cm.

Fig. 11. Horizontal thin section sequence of multi-year ice showing retexturing effects. Scale measures in centimeters and millimeters.

27

b. 93 cm.

c. 192 cm.

*Fig. 11 (cont'd). Horizontal thin section sequence of multi-year ice showing
retexturing effects.*

28

platelet/brine layer substructure of crystals are retained (though original c-axis alignment appears to be preserved), and the salinity has been reduced to 1.7‰, indicative of substantial desalination. The situation is even more extreme in the case of ice from 20 cm (Figure 11a), which bears little resemblance whatsoever to congelation sea ice. Crystal boundaries have developed sutured outlines, and all trace of substructure has disappeared. Total loss of brine pocket structure in this ice is also reflected in the salinity, which measured less than 0.2‰.

Retexturing of crystals in the upper levels of multi-year floes and the associated loss of brine (and brine pockets) also produces very substantial changes in the mechanical and electrical properties of the ice. In the case of the latter such changes should result in remote sensing signatures being significantly different from those of first-year ice.

In this brief report we have described the various forms of crystal structure that characterize the sea ice in Fram Strait. We have found that frazil is a minor component of the floes, and that retexturing of the crystal structure is a prevalent and diagnostic property of the congelation ice in the top meter or so of multi-year floes. Based on the structural properties described here, in conjunction with other physical properties of the ice, we have been able to distinguish between first- and multi-year ice and to determine the ages of multi-year floes. In addition, we have obtained a much better understanding of the processes that control the growth characteristics and metamorphic properties of the ice entering Fram Strait from the Arctic basin.

REFERENCES

Gow, A.J., Quiet freezing of lakes and the concept of orientation textures in lake ice sheets. *Proc. IAHR 7th Symp. on Ice,* Hamburg, August 27-31, 1984, *1,* 137-149, 1984.

Gow, A.J., S.F. Ackley, W.F. Weeks and J.W. Govoni, Physical and structural characteristics of Antarctic sea ice. *Annals Glac., 3,* 113-117, 1982.

Langhorne, P.J., Laboratory experiments on crystal orientation of NaCl ice. *Annals Glac., 4,* 163-169, 1983.

Nakawo, M. and N.K. Sinha, A note on brine layer spacing of first-year sea ice. *Atmos.-Ocean, 22*(2), 193-206, 1984.

Tucker, W.B. III, A.J. Gow and W.F. Weeks, Physical properties of sea ice in the Greenland Sea. *Proc. POAC-85,* Narssarssuaq, Greenland, September 7-14, 177-188, 1985.

Weeks, W.F. and A.J. Gow, Preferred crystal orientation along the margins of the Arctic Ocean. *Jrnl. Geophys. Res., 83*(C10), 5105-5121, 1978.

Weeks, W.F. and A.J. Gow, Crystal alignments in the fast ice of arctic Alaska. *Jrnl. Geophys. Res., 85*(C2), 1137-1146, 1980.

Weeks, W.F. and S.F. Ackley, The growth, structure and properties of sea ice. USA Cold Regions Research and Engineering Laboratory, CRREL Monograph 82-1, 130 pp., 1982.

MIZEX 84 Ice Surface Measurements
from the FS *Polarstern*

B.A. BURNS, R.W. LARSON and R.G. ONSTOTT
Environmental Research Institute of Michigan
P.O. Box 8616, Ann Arbor, Michigan 48107, U.S.A.

INTRODUCTION

The principal parameters used in modeling the microwave response of a surface are the dielectric constant of the surface material and the surface and subsurface roughness. The dielectric constant depends on the physical properties of the material: temperature, density, and composition. It is greatly affected by the presence of liquid water in the material because of the highly absorptive nature of water in the microwave portion of the spectrum. In the case of snow cover, snow wetness can be a critical factor in the value of the dielectric constant, and therefore in its microwave response.

The snow cover on arctic sea ice is of interest for both its own signature and its effect on the signature of the underlying ice. Surface albedo is a key parameter in thermodynamic models of sea ice growth and can differ significantly for dry snow and melting snow conditions (Shine and Henderson-Sellers, 1985). The state of the snow also determines whether it is transparent or opaque, or totally masking to radiation coming from the sea ice. Snowpack with high liquid water content can, depending on the operating frequency of the sensor, absorb sufficient radiation that it appears similar to open water, or limit penetration such that surface scattering dominates and the sea ice has a uniform signature regardless of ice type (Onstott and Moore, 1984). Both effects introduce errors into estimates of ice concentration and ice thickness (i.e. ice type) distribution derived from remote sensing instruments.

During MIZEX 84 several groups working from different research vessels made measurements of the dielectric constant, snow wetness and physical properties of the snow cover on ice floes. We report here results obtained by the group operating from the FS *Polarstern*. Nineteen sites were visited during the period 18 June–14 July 1984 for which both dielectric constant and snow wetness measurements were made. These sites were distributed across the region traversed by *Polarstern*, generally 78°10′N to 80°40′N and 11°W to 9°E, as seen in Figure 1. Exact site locations are given in Burns and Larson (1985). Snow cover conditions at these sites ranged from dry and cold to melting, with snow depths between 0 and 85 cm. Ice cores were obtained at most sites by the Cold Regions Research and Engineering Laboratory (CRREL) team, so that ice type was positively determined. Dielectric constant measurements of two of the core samples are also reported here.

Although some sites, especially the ones visited early in the experiment, do not have coincident remote sensing data, the aim was to coordinate measurements with shipscat and heloscat operations and with aircraft SAR, SLAR or PMI data collection. Nine of the site measurements were coordinated with shipscat measurements, five with heloscat flights, two with aircraft PMI overflights, and seven with aircraft SAR or SLAR overflights.
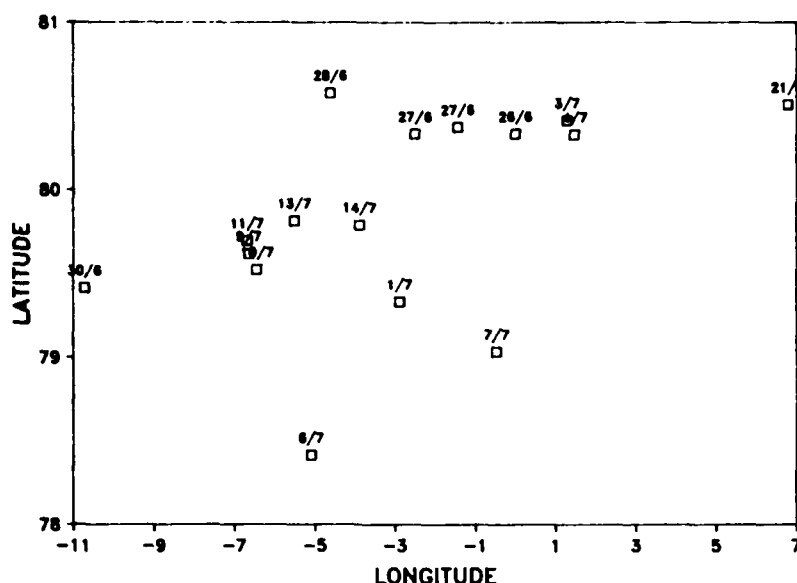
Fig. 1. Site positions for dielectric constant measurements made from Polarstern during MIZEX 84.

EQUIPMENT AND OPERATION

Equipment used in making surface measurements included ERIM dielectric constant instrumentation at 100 MHz, L-band and X-band (Larson, 1986), CRREL alcohol calorimetry apparatus to measure snow wetness (Fisk, 1983), a snow density kit (sample tubes and balance), stem thermometers, and collapsible rulers. The 100-MHz Q-meter proved the most useful of the dielectric instrumentation because it was the most portable, could be used to profile the significant snow cover found throughout the experimental area, and provided values for both the real part of the dielectric constant and the loss tangent most directly.

At sites accessed directly from the ship, a full set of dielectric constant, snow wetness, and snow characterization measurements were carried out, as it was possible to transport all necessary equipment to the ice. For these sites snow samples were taken back to the ship and the liquid water fraction measured in a coldroom under controlled conditions. Usually, but not always, ship-mounted scatterometer measurements and ice cores were also obtained for these sites.

When accessing the ice with helicopter, both time and space were very limited so that only 100-MHz dielectric measurements were carried out. On one helicopter mission snow wetness was

measured on the floe, but due to the lengthiness of the measurement this was not repeated, and on the next mission samples were brought back. The inevitable change of state caused by transporting samples will of course introduce additional uncertainties in the measurement results.

The dielectric constant results reported here are restricted to those obtained at 100 MHz, as these represent the most complete record both spatially and temporally. A full tabulation of the surface measurements is given in Burns and Larson (1985).

RESULTS

Snow cover

The principal reason for making this set of surface measurements is to gain a better understanding of how the complex dielectric constant, and therefore remotely sensed microwave signatures, can be used to obtain information on snow cover conditions. It is of interest then how the measured surface parameters varied throughout the experiment and how the dielectric constant is related to them.

The temporal record of observed snow wetness between 21 June and 16 July is shown in Figure 2 superimposed on the surface air temperature
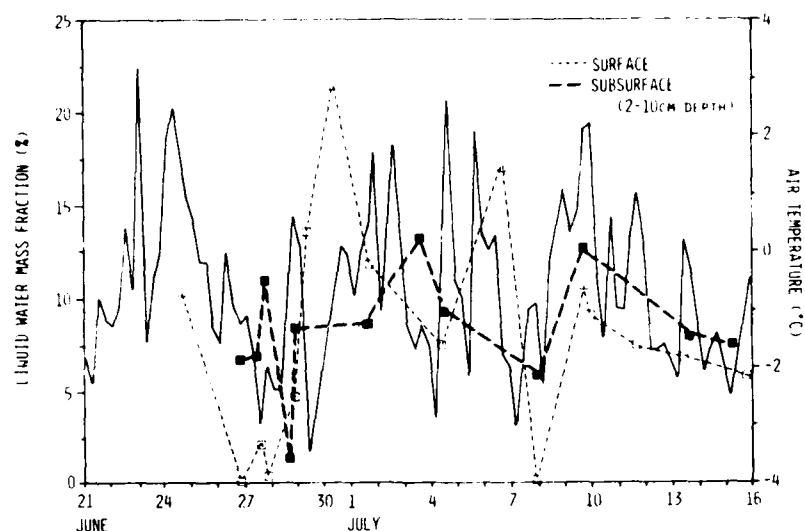
31

Fig. 2. Variation of the liquid water content of the snow cover contrasted with air temperature variation observed during the experiment.
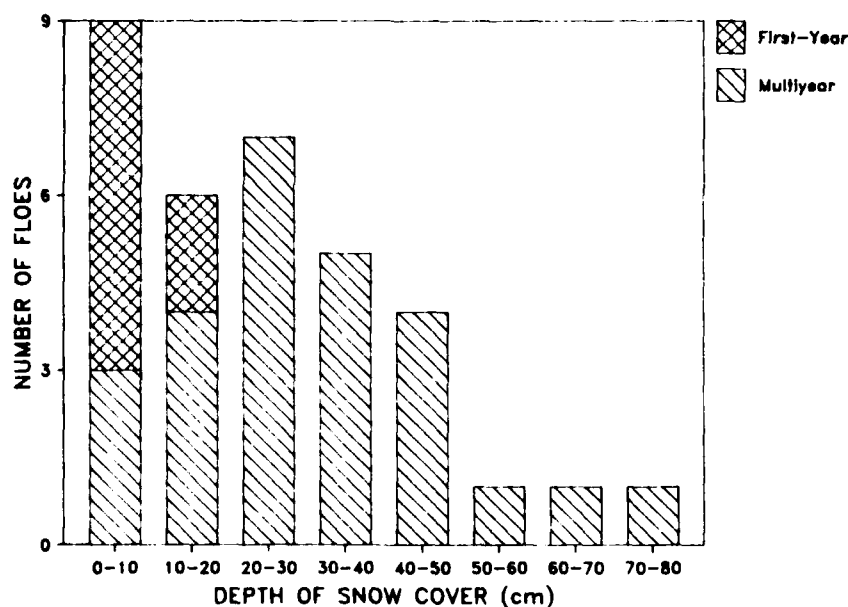

Fig. 3. Frequency of observed mean snow depth as a function of ice type.

record from *Polarstern*. Liquid water values for subsurface layers show much less extreme variation (1 to 13% by mass) than do the surface values (0 to 21% by mass), indicating the insulating effect of the snow. This may also be indicated by the observed lag in the liquid water plots relative to the temperature plot, which is most pronounced for the subsurface, although sample spacing is too sparse for this trend to be quantified. It should be noted that liquid water variability seen in Figure 2 also includes spatial variability, as the ship did not remain at one floe for more than a few hours, and it does not show the high liquid water content of snow cover observed near the snow/ice interface, which increased throughout the experiment as the melt season progressed.
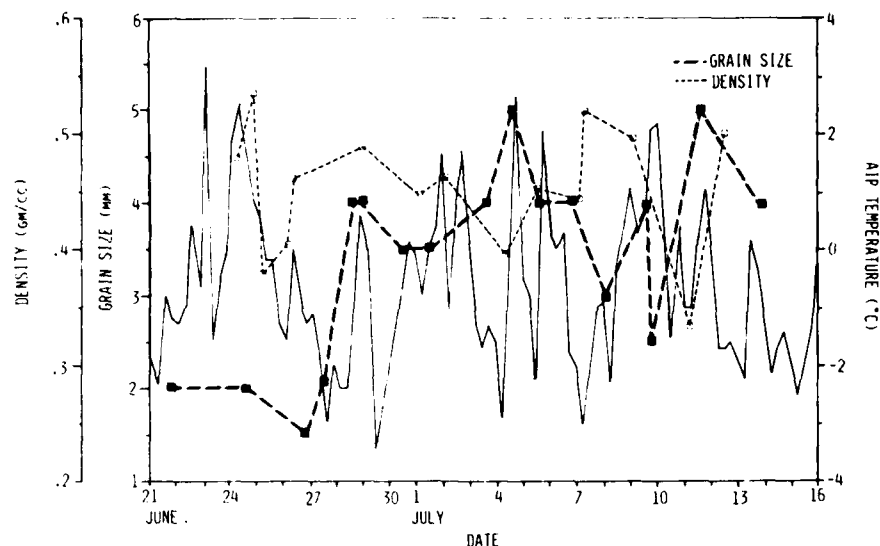
32

Fig. 4. Observed variations in snow density, grain size and air temperature
during the experiment period.

As seen from Figure 2, the majority of liquid water mass fraction values for subsurface measurements fall in the 5 to 10% range. The extreme values outside of this range correspond to first-year floe measurements. Although only a few data points are available, different behaviors for first-year and multiyear ice may be expected because of differences in amount of snow cover. On the average, multiyear floes had twice as much snow cover as first-year floes. The distribution of snow depths observed on both types of floes is shown in Figure 3; contributions to the 0- to 10-cm bin for multiyear floes come mainly from those floes visited late in the experiment when melting was significant.

The transition to melt conditions also produced a metamorphosis in snow cover from the less dense, small crystal snow to dense, large crystal (corn snow) firn. This was generally observed during the experiment and is to some extent quantified by grain size and density measurements plotted as a function of time in Figure 4. Density values plotted are for surface, or subsurface in cases of a surface crust. Again these plots reflect spatial as well as temporal variability, although over the area sampled the incident radiation is probably uniform.

Given the variation observed for liquid water, temperature, density and grain size (Figures 2 and 4), significant variation in the dielectric constant, which depends on all these factors, is also expected. The temporal record of the dielectric constant at

100 MHz is shown in Figure 5 for both the snow surface and snow at depths of 2–15 cm. Values range from 1.5 for frozen crust (T_{air} = –1.5°C) to 4.5 for firn with 5% liquid water content by volume. The surface measurements show a close correlation with surface temperature fluctuations (see Figure 6), whereas the subsurface measurements indicate more stable dielectric properties at depth. The spatial variability expected is indicated in Figure 7, which shows contours of dielectric constant based on a grid of measurements made on a site with fairly advanced melt. These results have two major implications for remotely sensed microwave signatures: (1) the microwave signatures will show significant temporal variability if the frequency is such that only the surface is sensed; and (2) given the typical sensor footprint size, the response reflects a mean dielectric constant with possibly large variance.

To understand the microwave signatures in terms of snow cover conditions (or in other words the effect of snow cover on the signatures) requires examination of the relationship between the complex dielectric constant and snow cover parameters. During the summer season, the dielectric properties of the snow cover are primarily determined by its liquid water content. The correlation between the electrical properties and liquid water content is demonstrated in Figure 8. Here the real part of the dielectric constant, ϵ', and the loss tangent, $\tan\delta$, are plotted against volume liquid water content per unit volume, W_v. A linear

33
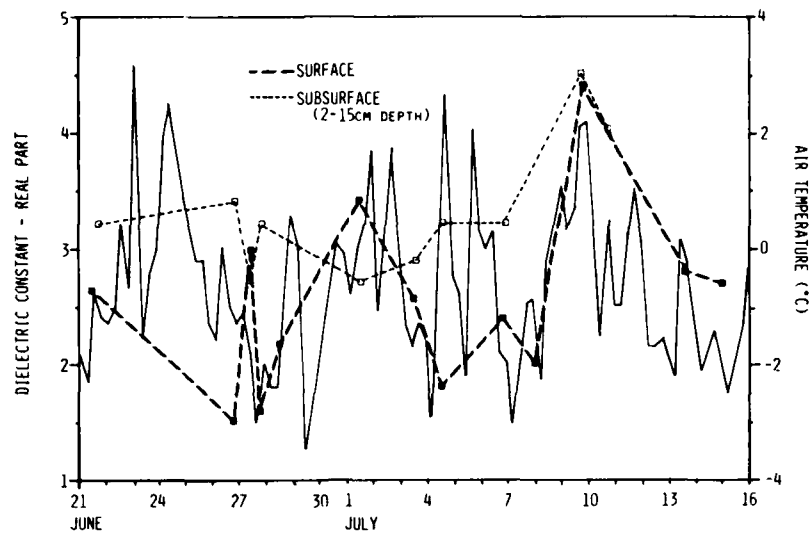
Fig. 5. *Variations in dielectric constant values for surface and subsurface snow contrasted with air temperature variation for the experiment period.*
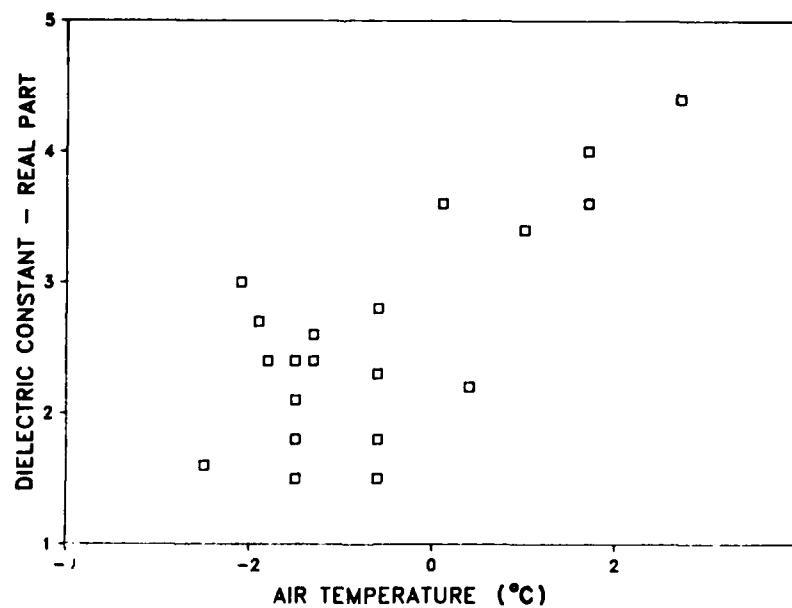
Fig. 6. *An approximate linear dependence observed between surface dielectric constant measurements and air temperature.*

34
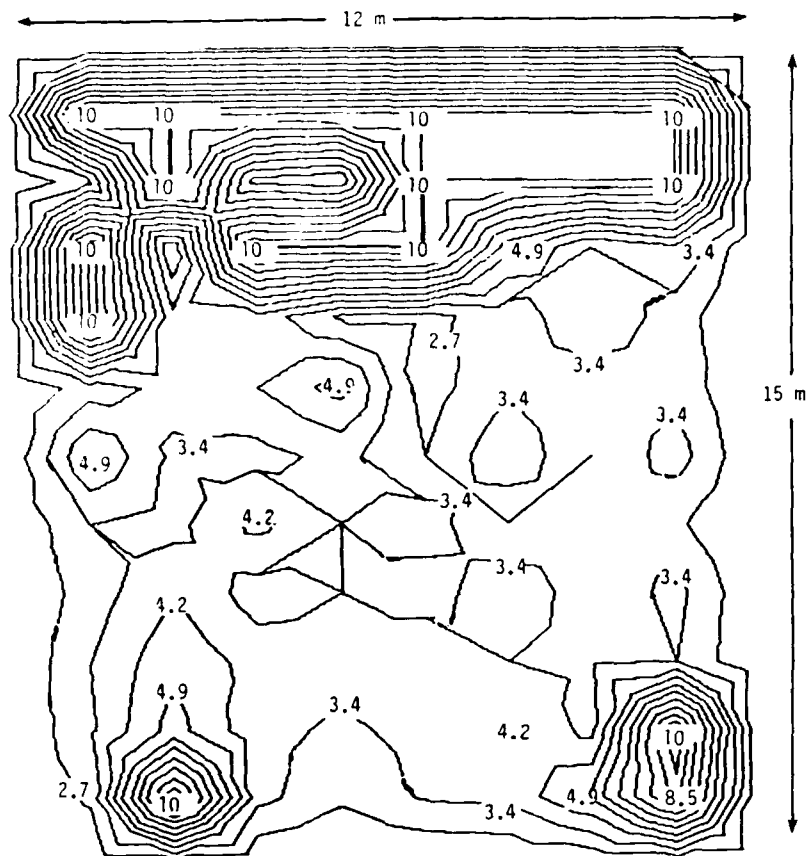
Fig. 7. 2-D contour plot shows spatial variation of 100-MHz dielectric constant values over an area representing approximately 20 SAR resolution cells. Values of 10 represent melt-pond areas where no measurements were obtained.

Fig. 8. Measured values of both the real part of the dielectric constant and the loss tangent increase with increasing snow liquid water content.

a. *Observed relationship between measurement values (correlation coefficient ≈ 0.6). The effect of liquid water content on the measured density has been removed.*

b. *Relationship between dielectric constant ϵ', snow density ϱ_{DS}, and liquid water content W_v derived from the data plotted for W_v ranging from 0 to 6% by volume.*
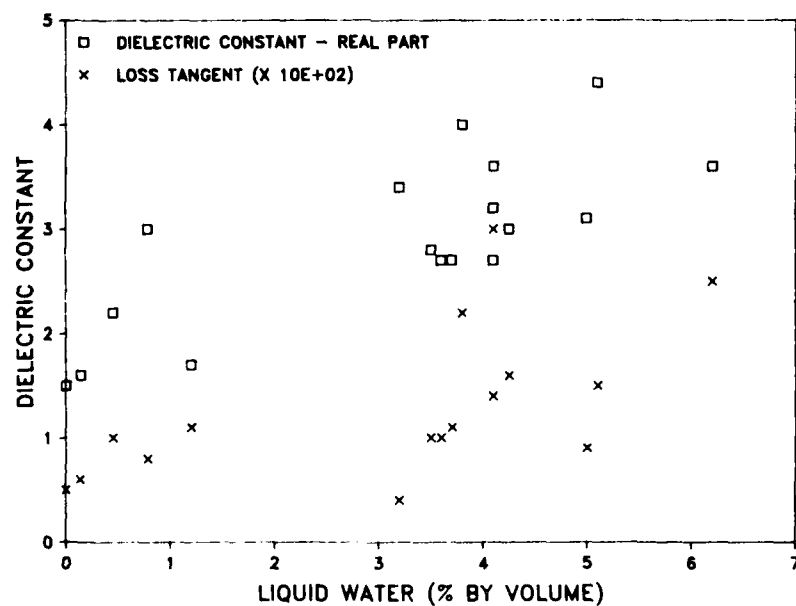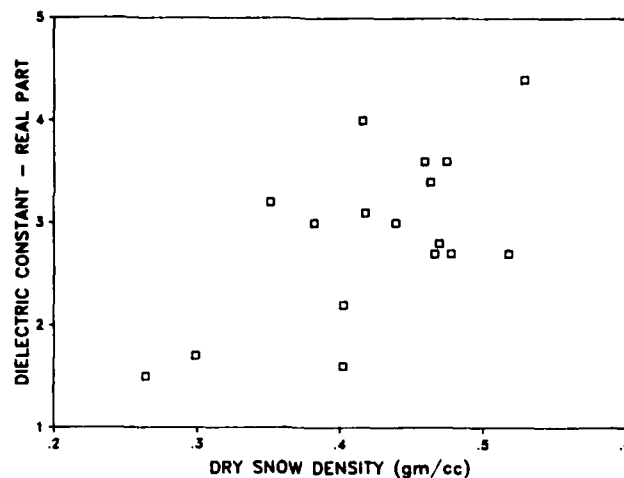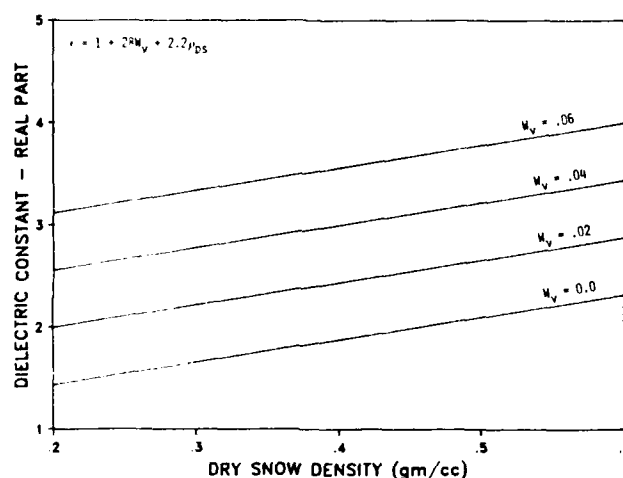
Fig. 9. Dielectric constant (real part) versus snow density.

regression of W_v against ϵ' results in a correlation coefficient of 0.8. The regression coefficient for W_v vs tanδ is 0.6.

Snow temperature, grain size, and density variations can also affect dielectric properties, although their importance is greatly reduced in the summer season. During the measurement period the snow temperature remained near the melting point, ranging between -1°C and 0°C. Such small variation was insufficient to produce detectable variations in the dielectric properties.

The measured values of the real part of the dielectric constant do show a weak correlation with snow density (Figure 9a) but no correlation with grain size. Doing a multiple linear regression of liquid water and snow density against ϵ' resulted in the relationship

$$\epsilon' = 1 + 2.2\varrho_{DS} + 28W_v \qquad (1)$$

where ϱ_{DS} is an equivalent dry snow density in which the liquid water is replaced by air:

36
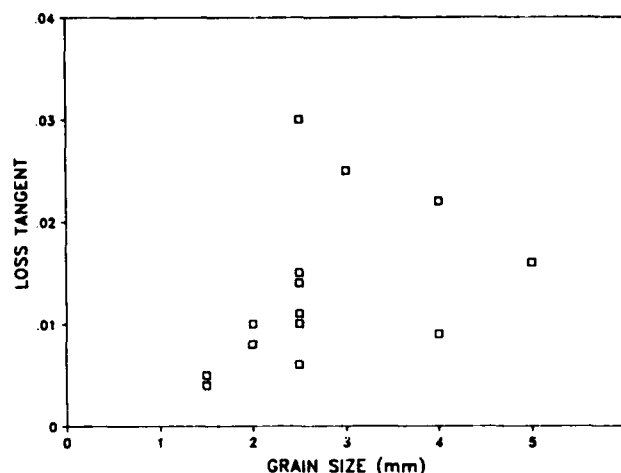
a. Observed relationship between measurement values (correlation coefficient = 0.4).
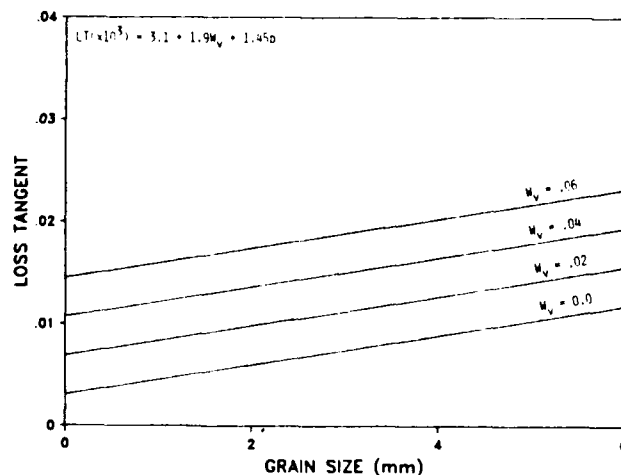
b. Relationship between loss tangent LT, grain size d, and liquid water content W_v derived from the data plotted for W_v ranging from 0 to 6% by volume.

Fig. 10. Loss tangent versus grain size.

$$\varrho_{DS} = \frac{\varrho_s - W_v}{1.0 - W_v} \approx \varrho_s - W_v. \qquad (2)$$

This relationship between ϵ' and dry snow density for a range of liquid water content values is plotted in Figure 9b.

Measurements of loss tangent appear to be correlated not with density but with grain size, al-

though weakly so, as indicated in Figure 10a. A multiple linear regression of liquid water content and grain size, d, produced the relationship

$$\tan\delta(\times 10^3) = 3.1 + 1.9 W_v + 1.45 d. \qquad (3)$$

Following this relationship the loss tangent is plotted against grain size in Figure 10b for several values of liquid water content.
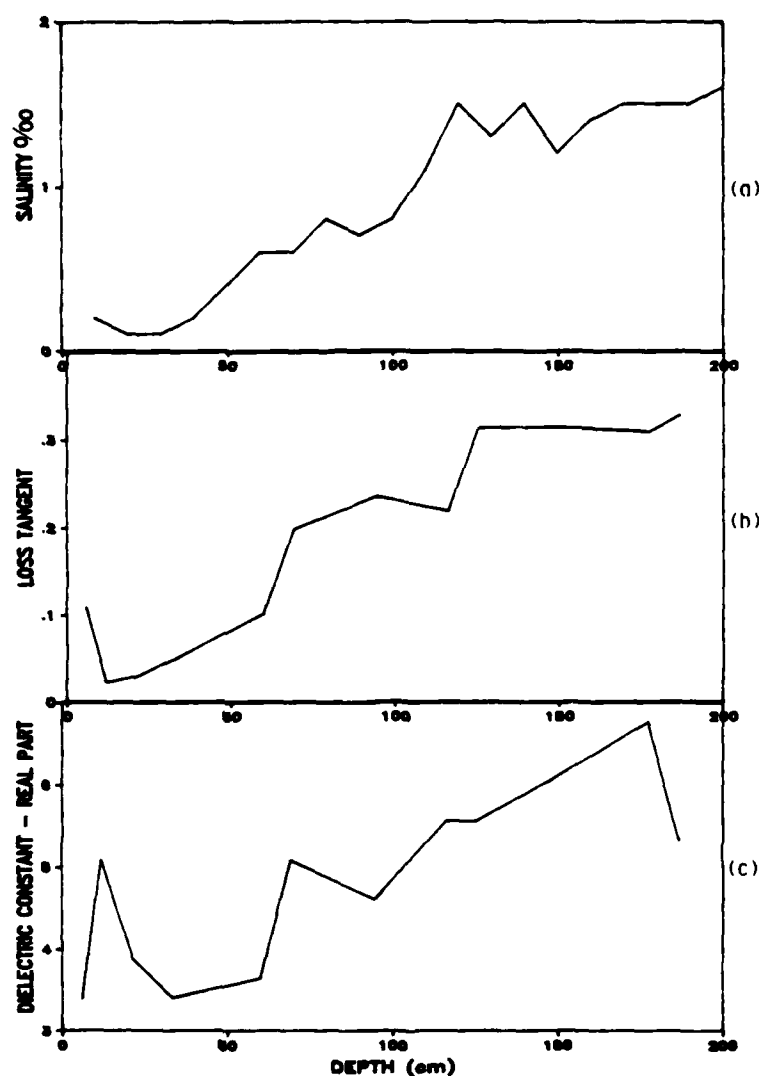
Fig. 11. Comparison of salinity (a) and 100-MHz dielectric constant measurements (b and c) as a function of depth into the ice for multiyear floe core 11-1 shows close correlation between loss tangent and salinity.

Ice cores

Under certain conditions, such as relatively dry and/or thin snow cover and the use of relatively long wavelengths, penetration through the snow and into the ice can be significant. The dielectric properties of the sea ice then become important. Depth profiles of the real part of the dielectric constant and loss tangent were obtained for ice cores from two multiyear floes, one core from a relatively uniform region of congelation ice and one from a ridge. These are shown in Figures 11 and 12 along with salinity profiles determined from adjacent cores by the CRREL team.

Measurements were made using the 100-MHz Q-meter device in the ship's coldrooms approximately 10–12 hours after the cores were extracted from the floes. Samples were cut from labeled core segments that were being stored for structural analysis at -10°C. Actual measurements were carried out in an adjoining coldroom at 0°C, which may have induced some surface melting in the samples as will be discussed later.

For both cores the loss tangent measurements appear to be positively correlated with salinity, showing a general increase with increasing salinity as expected from previous measurements (e.g.

38
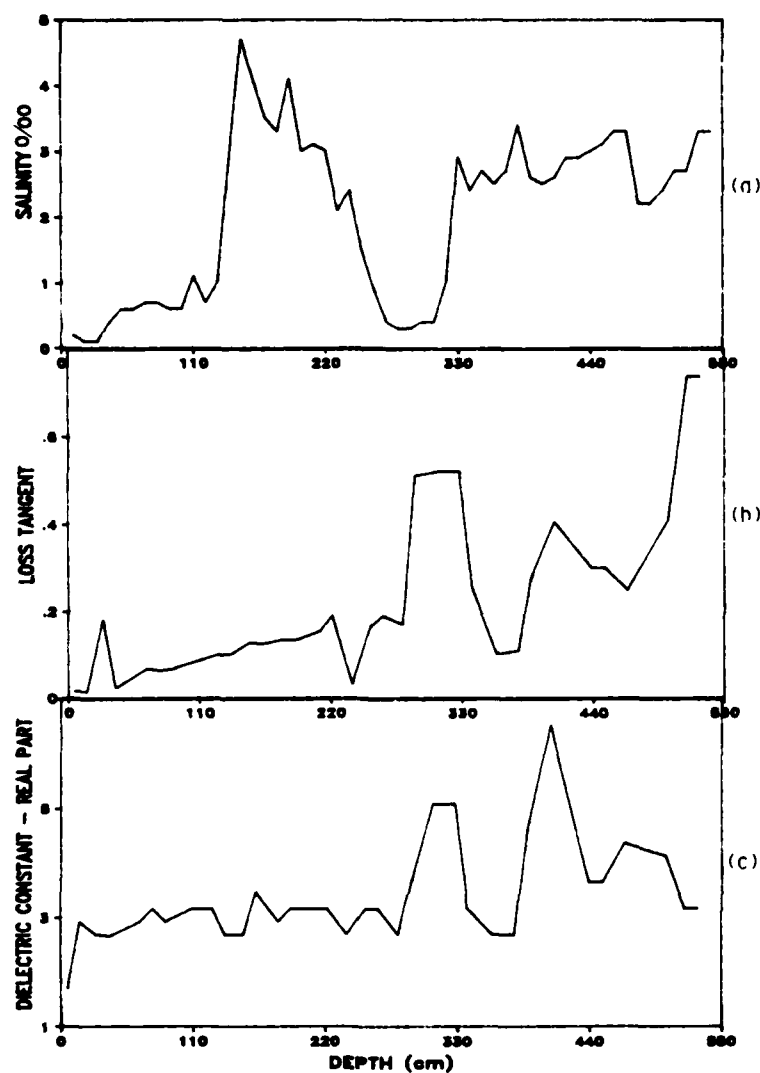
Fig. 12. In contrast to Figure 11, depth profiles for multiyear ridge core 13-1 show little correlation between salinity and loss tangent.

Vant et al., 1978). The loss tangent profile for core 11-1 closely follows the form of the salinity profile, whereas that of core 13-1 shows significantly more deviation. Part of this discrepancy may be attributable to mislabeling of core segments. A separate salinity measurement made on the ice sample used for the dielectric constant measurement at "360 cm" produced a salinity value of 0.5%oo, corresponding to the values at 270–320 cm in the salinity profile. The dip in loss tangent at "360 cm" in the loss tangent profile may therefore actually be due to the dip at 270–320 cm in the salinity profile. Other deviations may be due to the

structural variations found in this multiyear ridge core. Because of these uncertainties and the time lag between the extraction of the cores and these measurements, a relationship between loss tangent and salinity cannot be reliably derived from these data.

The measurements of the real part of the dielectric constant show much less correlation with the salinity profiles than do the loss tangent measurements. The real part is more sensitive to porosity than to salinity so that some of the variations observed in the dielectric constant profiles probably reflect structural changes, especially for core 13-1,

39

which is composed of several different segments of frazil and congelation ice and mixtures of the two (A. Gow, private communication). However, no clear correlation between dielectric constant and structure is observed when the two profiles are compared. The extremely high values (> 5.5) cannot be attributed to structural fluctuations and probably reflect the presence of liquid water either on the walls of the 100-MHz cavity or in the sample. This unavoidably results from the necessity of making measurements in the 0°C coldroom. These values are therefore not representative of the in situ dielectric properties of the sea ice itself and should be discounted.

CONCLUSIONS AND RECOMMENDATIONS

Analysis results from measurements of snow cover properties made from the *Polarstern* during MIZEX 84 have been presented here with the aim of providing relationships between dielectric properties and surface and environmental conditions that can be used in the interpretation of remotely sensed microwave data taken during the experiment. The major results obtained from this analysis are:

1. Documentation of the temporal variation in dielectric properties of snow cover. Results show a linear increase in dielectric constant with increased air temperature, which probably reflects the change in snow liquid water content. These measurements need to be compared with values of surface radiant heat flux also.

2. Determination of the relationship between liquid water content and dielectric properties for snow cover in the MIZ. It was found that the real part of the dielectric constant depended on liquid water content and, to a lesser extent, snow density. The loss tangent (imaginary part/real part) also depended on liquid water content and was weakly correlated to grain size. Additional measurements are needed over a wider range of densities and snow temperature.

3. Comparison of the depth profiles of dielectric constant and salinity for multiyear ice cores. This showed that a high correlation does exist between loss tangent and salinity, but that other factors

(ice structure) control the behavior of the real part of the dielectric constant.

In carrying out this analysis, several potential improvements to the measurement routine have become evident. One parameter that was not measured consistently was the air temperature at the surface where measurements were being made. Observations through several diurnal cycles of the same snowpack are also needed to monitor snow metamorphosis. These data, combined with radiant heat flux measurements, would provide further insight into the dependence of electrical surface properties and meteorological parameters. With regard to sampling techniques, liquid water measurements need to be made in situ from the same sample level as dielectric constant measurements, and dielectric constant measurements on ice cores need to be made immediately after they are extracted, with simultaneous temperature and density measurements.

REFERENCES

Burns, B.A. and R.W. Larson, Trip report: ERIM activities on "Polarstern" to support MIZEX 84 remote sensing. Environmental Research Institute of Michigan, ERIM Report 166900-7-1, 1985.

Fisk, D.J., Progress in methods of measuring free water content of snow. In *Optical Engineering for Cold Environments,* Society of Photo-Optical Instrumentation Engineers, Bellingham, Washington, p. 48-51, 1983.

Larson, R.W., Field devices for dielectric constant measurements at 0.1, 1.0 and 10 GHz. In preparation, 1986.

Onstott, R.G. and R.K. Moore, Active microwave measurements of sea ice in the marginal ice zone under summer conditions. In *Proceedings IGARSS 84,* p. 359-363, 1984.

Shine, K.P. and A. Henderson-Sellers, The sensitivity of a thermodynamic sea ice model to changes in surface albedo parameterization. *J. Geophys. Res., 90,* 2243-2250, 1985.

Vant, M.R., R.O. Ramseier and V. Makios, The complex-dielectric constant of sea ice at frequencies in the range 0.1-40 GHz. *J. Appl. Phys., 49,* 1264-1280, 1978.

1984-85 Current Observations in the East Greenland Current:
A Preliminary Description

R.D. MUENCH, G.S.E. LAGERLOEF AND J.T. GUNN
Science Applications International Corporation
13400B Northrup Way, Suite 36, Bellevue, Washington 98005, U.S.A.

1. INTRODUCTION

The East Greenland Current (EGC) is a primary oceanographic circulation feature in the Greenland Sea (Figure 1). This current flows southward through Fram Strait and is initially a broad, strait-wide flow with a major component entering southwestward from the region north of Svalbard. Farther south this flow occupies only that portion of the Fram Strait-Greenland Sea region located west of the East Greenland Polar Front (EGPF), and contains a pronounced jet-like high-speed core just west of this front. The EGPF separates cold, low-salinity water exiting the Arctic Basin from warmer, more saline water in the central Greenland Sea. In central Fram Strait part of the current becomes incorporated into a cyclonic gyre which overlies the Molloy Deep. By the time it has come as far south as about 79°N, the jet-like core of the current has impinged upon the steep East Greenland continental slope, characterized at that point by north-south-trending isobaths which con-
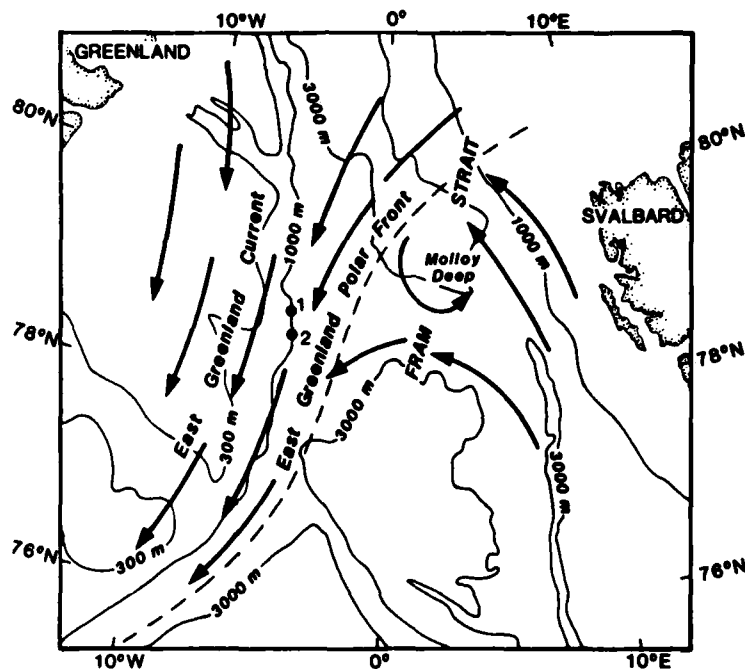

Fig. 1. Geographical location of the 1984-85 MIZEX current moorings (1 and 2), schematic representation of the major regional oceanic circulation features (arrows), location of the East Greenland Polar Front (dashed line) and major bathymetric features. Depths in the Molloy Deep exceed 5500 m.

strain the flow to a north-south orientation. The current coincides approximately with the outer marginal ice zone (MIZ) from the vicinity of Svalbard southward to the southern tip of Greenland, and it is suspected that the current exerts a strong influence over physical processes in the MIZ.

Though the EGC has long been recognized as a distinct feature, it has been only within the past decade or so that sufficient field work has been carried out to allow a preliminary quantitative description. As part of the ongoing effort to describe and understand this current, and in an attempt to identify its interactions with the MIZ, two current moorings were deployed within the EGC over a 13-month period in 1984-85. The moorings were located near the core of the current at about the 1000-m isobath along the continental slope, at about 78°30' and 78°45'N (see Figure 1). These locations lay west of the ice edge and were ice-covered throughout most of the observation period. Each mooring contained two current meters which sampled the upper and lower layers of the EGC, resulting in four records of current speed and direction, each about 13 months long. This report describes the observation program and presents and summarily discusses the most significant features seen in the resulting current data.

The data discussed in this report were obtained in conjunction with, and as part of, the summer 1985 Marginal Ice Zone Experiment (MIZEX).

2. THE OBSERVATION PROGRAM

The two current moorings were deployed nominally along the 1000-m isobath of the East Greenland continental slope in mid-June 1984 (Figure 1, Table 1). Variations in actual bottom depths of about 1000 m at the times of deployment were due to ship drift which occurred during the deployment operations. Mooring configuration was of the "standard" oceanographic taut-wire type, with 36-in. spherical steel floats positioned at about 90-m depth for flotation. This depth is well below that at which wave-induced rotor pumping is believed to have a significant biasing effect on the recorded current data. Acoustic releases were positioned below the deeper current meters on each mooring. The deployments took place during the early part of the summer 1984 MIZEX field program, and were carried out from the German research icebreaker *Polarstern*. The moorings were recovered in mid-July 1985 from the same vessel.

The instruments used were Aanderaa RCM-4 recording current meters. These units measure speed to a factory-advertised accuracy of about ± 1 cm/s (at the speeds which were observed), and direction to about ± 5°. The sampling intervals were 60 minutes, with speeds integrated over this period and direction measured once instantaneously during each interval. The raw data were first inspected visually for bad data points. This inspection revealed that the first 4 days' upper level record at mooring 2 was irretrievably contaminated by "spiking," and this short segment of the record was deleted. Some minor spiking during the final month's upper level record from mooring 1 was edited out of the data, leaving a satisfactorily clean record. As a final check on data quality, harmonic tidal analyses were carried out on sequential 30-day record segments. Invariant amplitudes, phases and major axis orientation of the tidal current constituents indicated that the speed, time base and directional data are reliable and that accuracy falls within the above specifications.

To provide a check on whether the moorings "heeled over" during periods of strong currents, which would have pulled the current meters into deeper water than under static conditions and resulted in recording of current data from depths greater than planned, the uppermost meters were equipped with pressure gauges. Some such deepening was observed on the few occasions when

Table 1. Particulars of the June 1984-July 1985 MIZEX current moorings.

Mooring ID	Latitude (North)	Longitude (West)	Date deployed (Z)	Date recovered (Z)	Bottom depth (m)	Instrument depth (m)
1	78°43.988'	4°51.131'	15 June 84	16 July 85	994	94 394
2	78°29.160'	4°33.288'	15 June 84	18 July 85	1020	120 420

strong (about 30 cm/s) currents were present at both depths, but these depth increases amounted to only a few meters and the incidents were not frequent or severe enough to affect the longer-term statistical validity of the data.

3. THE OBSERVED CURRENTS

The four current records obtained were each about 13 months long. This length is adequate to detect seasonal variations in current and, in addition, mesoscale variability and higher-frequency tidal and near-inertial motions which can also be characterized. Because these very generalized classes of motion reflect different dynamic processes, the following section is subdivided based upon the time scales of the observed currents into low-frequency (seasonal), mesoscale, tidal, and near-inertial.

3.1 Low-frequency currents

Each of the four current records was first resolved into its u (cross-isobath, east positive) and v (along-isobath, north-positive) components; u and v were taken to be in the same direction at both moorings so as to simplify comparisons between the records and also because the isobaths at each mooring trended within a few degrees (i.e. within the directional accuracy of the current meters) of true north. The resulting hourly u and v components were then subjected to a 35-hour low-pass filter to remove tidal and inertial constituents. The low-pass filtered records were then passed through a 30-day "boxcar" filter which effectively computes 30-day mean values with a 15-day overlap between consecutive 30-day intervals. A 95% error estimate was computed for each interval, where error = (2 standard deviations)/(square root [record length/2 ×integral time scale]) and the integral time scale is defined as the integral from zero to infinity under the autocorrelation curve (Lagerloef et al., 1981). The results of these computations are presented in Figure 2, and the discussion below refers to this figure.

The 30-day mean v components (Figure 2a) were almost always southward, the only exception being a brief period of northward flow, not significant at the 95% level, which occurred at mooring 1 in June 1985. The southward 30-day mean speeds were greatest in summer and for the upper records, and were smallest in winter for both the upper and lower records. Maximum southward summer speeds of order 10 cm/s occurred in the
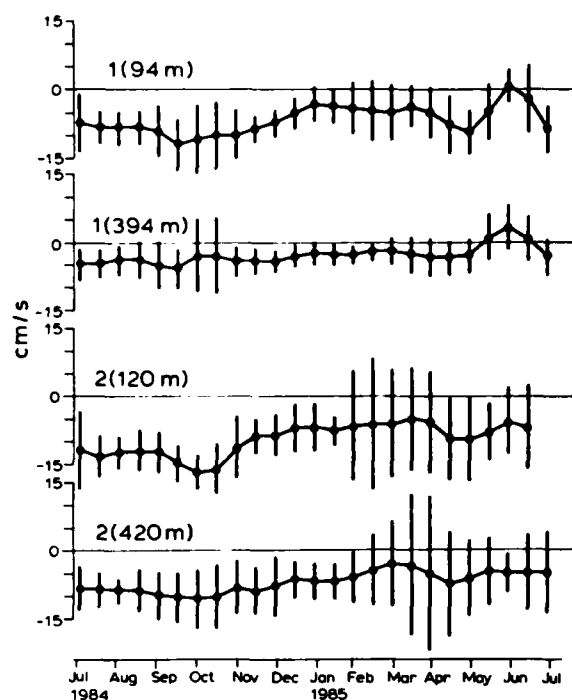
a. Along-shelf (v) components.
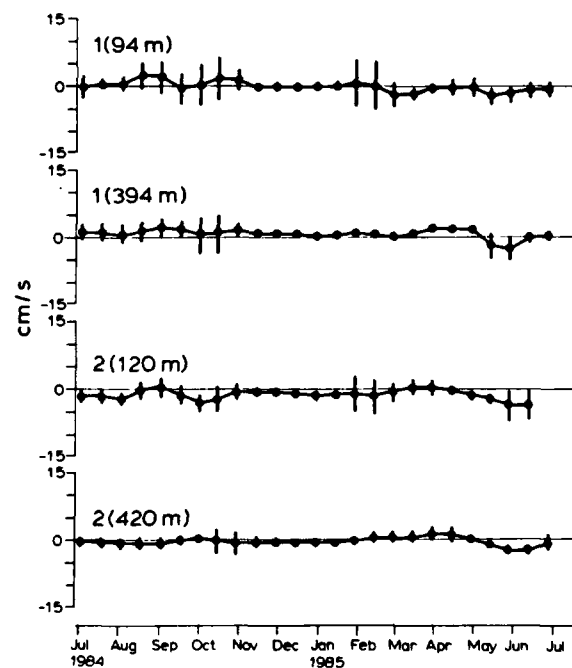
b. Cross-shelf (u) components.

Fig. 2. Very low pass (30-day) filtered current components. Vertical bars indicate error estimates computed as described in the text. Last month of series (8 June–8 July 1985) is omitted for convenience in plotting.

43

upper record at mooring 1, and speeds of more than 15 cm/s were observed in the upper record at mooring 2. Summer lower level speeds were of order 5 and 10 cm/s at moorings 1 and 2 respectively, so that the speed differences between upper and lower levels were about 5 cm/s at both moorings. Speeds were lower in winter than in summer, being less than 5 cm/s at mooring 1 and of order 5 cm/s at mooring 2. The differences between upper and lower level speeds were generally less than 2 cm/s in winter and were not significant at the 95% level. The large error bars during winter were due to occurrence of energetic mesoscale disturbances, noted in Section 3.2, which showed strong separation between upper and lower layers in contrast to the weak vertical shear in the 30-day means.

The 30-day mean u components (Figure 2b) were smaller than v at both moorings and at both levels; u was always less than about 3 cm/s and was often not significantly (at the 95% level) non-zero. There was no apparent preferred long-term direction in u; however, there was a tendency for weak (1–2 cm/s) eastward flow in summer 1984 at both depths at mooring 1 and for westward flow in summer 1985 at both moorings. In winter, u for both levels at the two moorings was less than 1 cm/s and was often negligibly small.

The above describes a mean (30-day averaged) flow which was consistently along-isobath and southward at speeds of 5–15 cm/s (upper level) and 2–10 cm/s (lower level), and which had much smaller (less than 3 cm/s) cross-isobath speeds with no apparent preferred direction. The higher speeds occurred in summer 1984. Vertical speed differences between the two levels were greatest at both mooring locations in summer 1984, with upper level speeds typically 5 cm/s greater than those in the lower level. In winter, vertical speed differences were typically 2 cm/s or less.

There are few available observations with which to compare these mean currents. Paquette et al. (1985) provide a useful summary of past work on the EGPF and present new data from October–November 1981. They have constructed dynamic topographies which show a southward net baroclinic flow, both at the surface and at 150 db, at the mooring locations. Their data were, however, insufficient to define the net flow orientation. They cite frontal jet speeds approaching 100 cm/s, far higher than observed at any time in our data, and it seems apparent that moorings 1 and 2 were not situated correctly to sample the highest speed front-associated currents ("jet"). The 100-m mean currents were 10–15 cm/s in autumn 1984,

and the 400-m currents were still between 5 and 10 cm/s. Paquette et al. used the 500-db level as a reference in computing dynamic heights, and our observations show that there was still considerable motion at 400 m in autumn 1984. A more quantitative representation of the upper layer dynamic topography would therefore require extrapolation of a deeper reference level onto the continental shelf from deeper water. Paquette et al. observe that surface current speeds are typically 3 to 10 times higher than at 150 db, consistent with baroclinic shear computed from historical data. Applied to our current observations, the overlying surface current speeds could have been as high as about 150 cm/s, perhaps an unrealistically high value but not incompatible with the abovementioned 100-cm/s currents associated with the frontal jet.

The presence of greater mean current speeds at mooring 2 than at mooring 1 can be qualitatively accounted for by referring to dynamic topographies presented by Paquette et al., and also by referring to Figure 1. At the approximate locations of the moorings, the EGC is impinging from the northeast onto the Greenland continental slope, so that the moorings were located in a zone of convergence between the slope-constrained southward flow and the main core of the EGC. Higher speeds at mooring 2 probably reflect a greater transport, due to this convergence, at that mooring than at mooring 1.

3.2 Mesoscale fluctuating currents

Mesoscale is taken here to include those fluctuations which occur primarily within the 2- to 12-day period band and exclude shorter period tidal and inertial motions. Mesoscale features have been observed throughout the world ocean to be typical of fronts, meanders, eddies and wind-driven motions.

The current records were resolved into u and v components and run through a 35-hour low-pass filter as described in Section 3.1. The qualitative nature of the mesoscale fluctuations can be seen in the resulting time-series of u and v components (Figure 3). For the early part of the records, from their start until about late October, the greatest fluctuations were typically about 15 cm/s in amplitude. A notable exception was the large (about 30 cm/s) single oscillation which occurred in late October, primarily at mooring 1, though it was present also in the lower level at mooring 2. From late October until early February all records were "quieter" than earlier. Through the mid-winter February–April period the currents were charac-
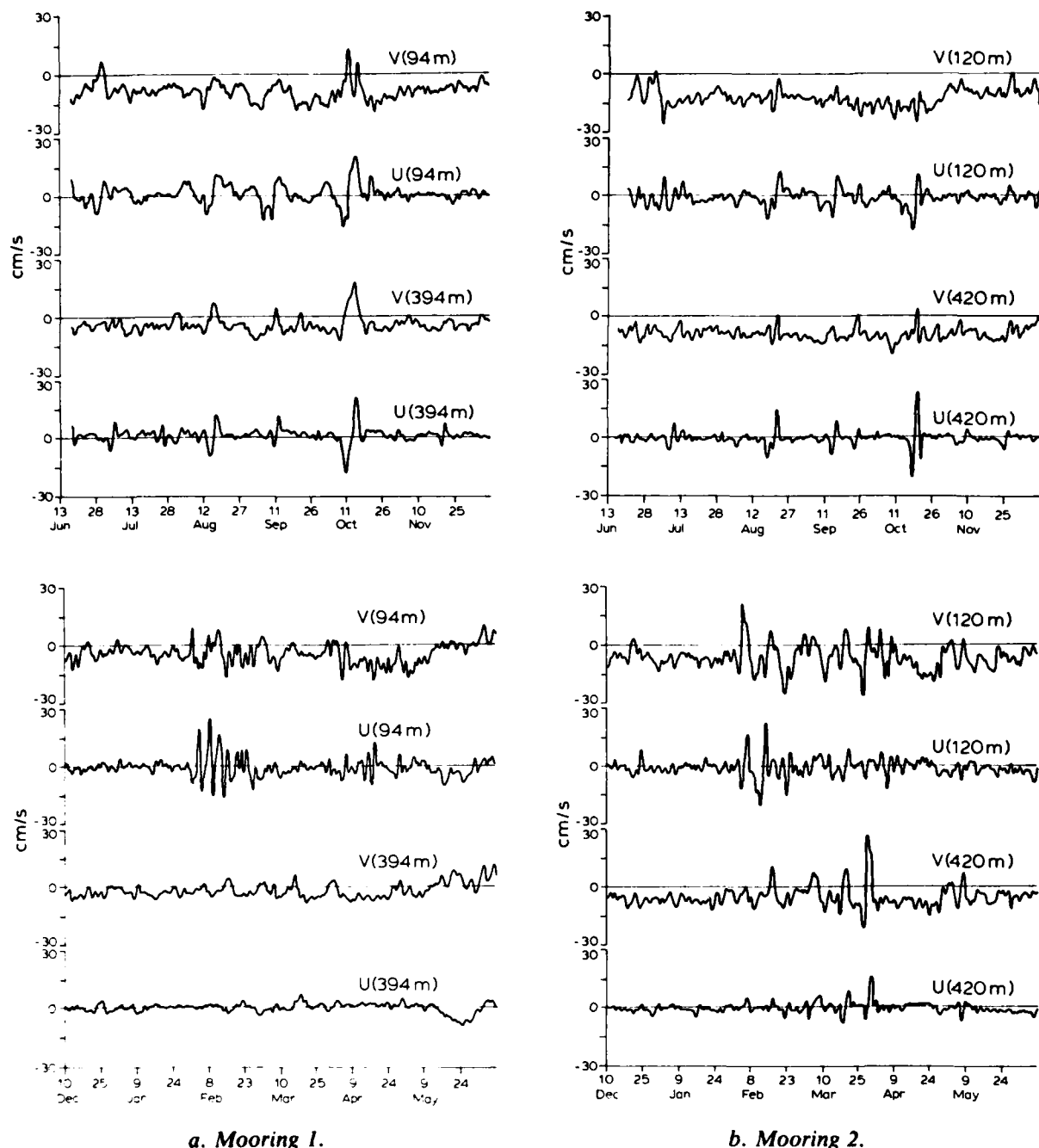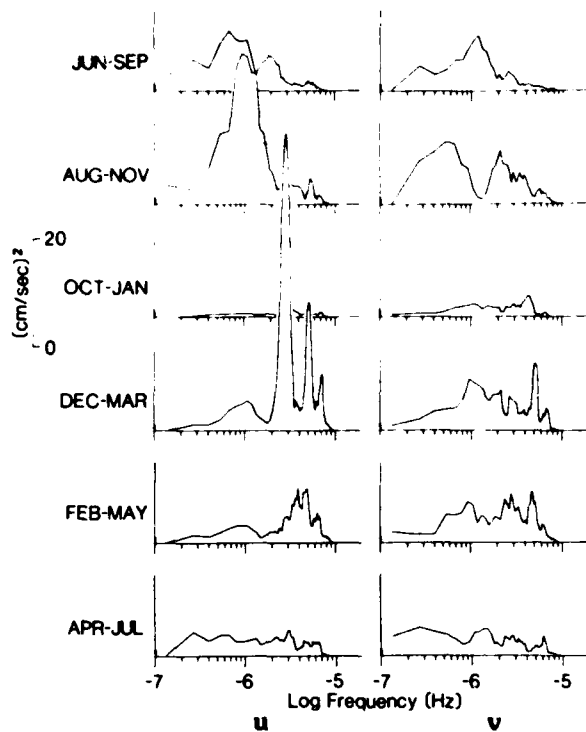
a. Mooring 1.   *b. Mooring 2.*

Fig. 3. Low pass (35-hour) filtered u *and* v *current components.*

terized by consistently large (20–30 cm/s), persistent fluctuations having shorter time scales than those observed through summer 1984. Finally, by May–June 1985 the fluctuations had returned to a pattern similar to that observed in summer 1984.

The above observations were quantified by computing energy-preserving spectra for the u and v components from all four time series (Figure 4). These spectra were computed for sequential 90-day-long records, with a 30-day overlap at each end. Each spectrum was band-averaged to give estimates with 10 degrees of freedom. This method provides a sufficiently long record for each spectral computation to give confidence in the results.

a. Mooring 1, 94 m.
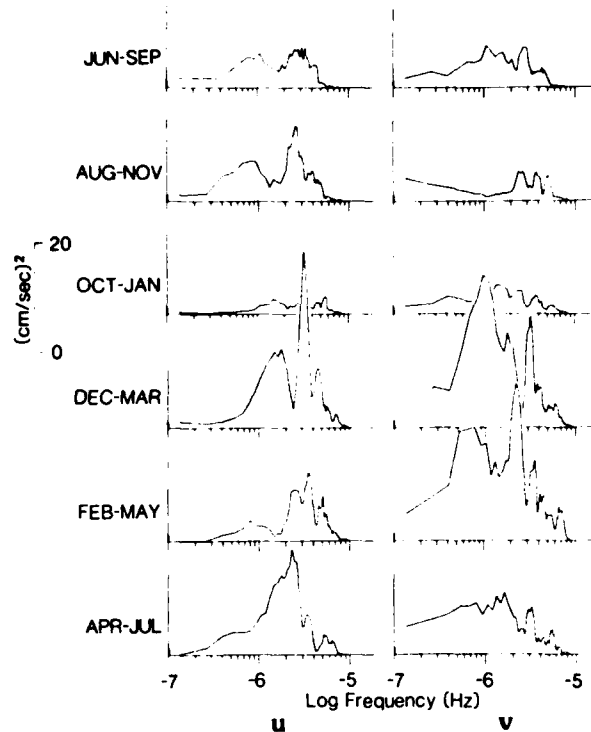
c. Mooring 2, 120 m.
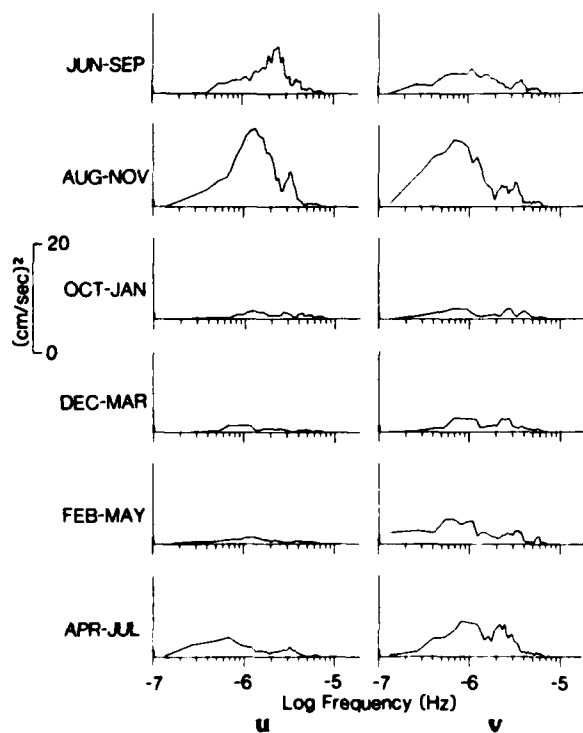
b. Mooring 1, 394 m.

d. Mooring 2, 420 m.

Fig. 4. Variance spectra computed for overlapping, sequential 90-day segments of the current record at moorings 1 and 2. Segments started on the 15th of the month and ran for 90 days. Interval is given by month in the left margin. Left plot is for u (cross-isobath), and right plot is for v (along-isobath).

46

and also breaks the entire record into enough segments to identify the long-term differences which were noted visually from the time-series plots. These spectra yield the following information.

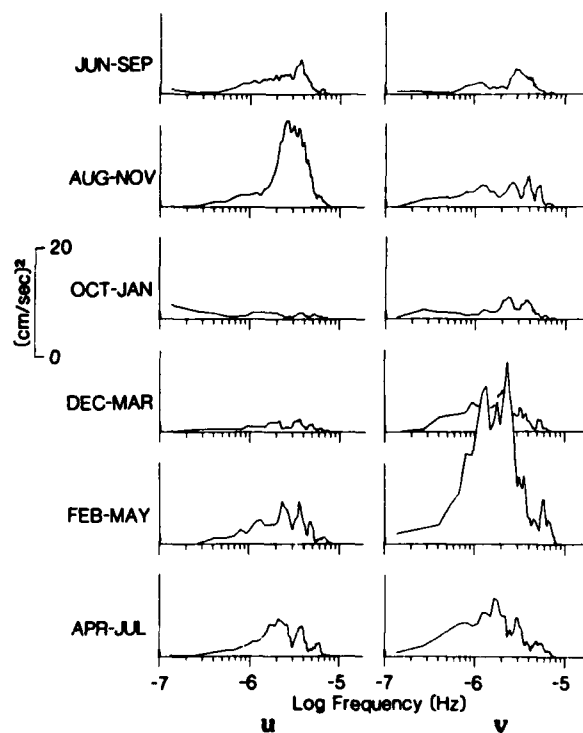1. The significant mesoscale energy was contained in the period band between about 2 and 12 days.

2. The upper level observations at both moorings showed a tendency for energy to be concentrated at longer periods (8–12 days) in summer and shorter periods (2–4 days) in winter.

3. No significant changes in spectral energy or shape occurred during June–November 1984, except for some increase in longer period energy in the upper layer at mooring 1 in August–November, in qualitative agreement with our above observation that the time-series appeared steady through this period.

4. October 1984–January 1985 was characterized by low energy levels, in contrast to the preceding and following periods.

5. December–March was characterized by a dramatic increase in upper layer energy levels. This affected primarily the u component at mooring 1, but affected u and v nearly equally at mooring 2. This energy was dominated by a very sharp peak at about a 4-day period, which reflects presence of the strong oscillations which were noted in the time-series plots for February–March 1985. This energy level persisted into the late winter (February–May) period in both the upper and lower layer v components at mooring 2 but not at mooring 1. The significant vertical difference in mesoscale energy during this period is in striking contrast to the 30-day mean flow (Figure 2), which implied minimum vertical shear during the same period.

6. By spring-summer (April–July) 1985 the spectral signatures appeared to be reverting to those observed during the previous summer.

Finally, empirical orthogonal functions (EOF's) were computed for four different periods, each 90 days in length and chosen based upon inspection of both the time-series and the spectra to encompass periods characterized by quasi-steady behavior. These periods were:

I. Ninety days starting 15 June 1984, falling in the interval of strongest vertical mean shear (as inferred from the differences between upper and lower level currents) and longer period mesoscale oscillations.

II. Ninety days starting 15 October 1984, falling in the interval of intermediate vertical mean shear and low mesoscale variance.

III. Ninety days starting 15 January, encompassing the period of weakest mean currents, smallest vertical mean shear and large, relatively short period mesoscale oscillations.

IV. Ninety days starting 15 April, falling in an interval of intermediate current speeds, vertical mean shear and mesoscale variance energy.

Each mooring was analyzed separately. With two sample depths each, the records were decomposed into u and v components which generated four input time series for the EOF analyses. These analyses produced, in turn, four EOF modes describing the vertical empirical structure at each location for each period. The resulting eigenvectors representing the u and v components for each record are recombined into a vector representation (Figure 5). (We note that use of complex EOF analyses would have produced two rather than four modes and would only have shown relative as compared to absolute orientation of the eigenvectors.)

In all cases more than 80% of the variance was contained in the first two modes; therefore, only these two modes are discussed here. Forming dynamical interpretations of empirically derived modes requires that decoupled dynamic modes dominated the system throughout the period under analysis. For example, definition of barotropic and baroclinic modes requires that the former have nearly equal eigenvectors at each depth. This situation is clearly not prevalent in the results depicted in Figure 5. Consequently, the following discussions emphasize the statistical properties which can be described from EOF analyses.

Mode 1, the dominant mode, contained between 46% and 65% of the total mesoscale variance energy. This mode rotated, at both moorings and depths, from a primarily cross-shelf direction in June–September to primarily along-shelf by the following spring. The strong winter cross-shelf orientation at mooring 1 (also evident as a cross-shelf mode 2 at mooring 2) was an exception, and was due to the strong February–March east-west fluctuations which were noted above. The second mode contained 19–41% of the total variance, so that for any specified period more than 80% of the variance was contained in modes 1 and 2. The second mode behaved in inverse fashion to the first, i.e. it rotated from primarily along-shelf in June–September to primarily cross-shelf by the

47

MODE 1

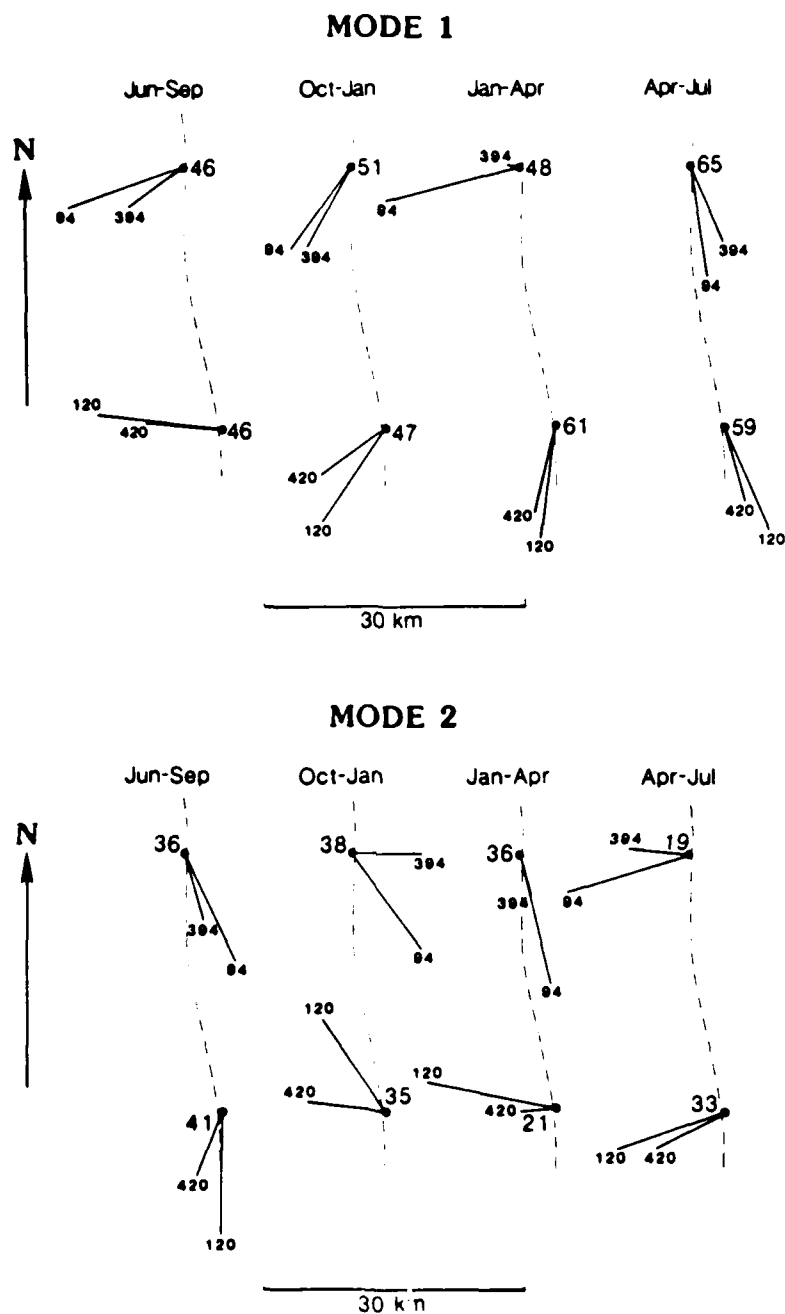## MODE 2

Fig. 5. EOFs computed for four separate periods. Upper plots are for first mode EOFs, while lower plots are for second mode. Dashed lines show local bathymetric trend. Solid dots indicate mooring locations (uppermost is 1 and lower is 2 for each EOF plot), and nearby numbers indicate percentage variance contained in that mode. Smaller numbers near "heads" of vectors indicate depths.

following spring. In June-September 46% of the variance was cross-shelf (mode 1) while 36-41% was along-shelf (mode 2); the difference between these two modes is probably not significant for this period, which we would expect because u and v fluctuations were similar during this period (Figure 3). In October-January the modes were both inclined to the isobaths. This period, however, was one of quite low variance (see the October-January spectra in Figure 4) so that the significance of the modes for this period is uncertain. In January-April the upper layer at mooring 1 shows the influence of the vigorous cross-shelf fluctuations, an influence which was evident in the weaker cross-shelf mode 2 at mooring 2. By April-July the majority of the variance was still along-shelf, 65% at mooring 1 (mode 1) and 59% at mooring 2 (mode 2).

The EOFs also provide information on vertical differences in the variance. In June-September the lower level EOFs were typically about half those in the upper level. In October-January the upper and lower level values were more nearly equal. In January-April the picture was more confused, with nearly all of the variance at mooring 1 occurring in the upper layer whereas mooring 2 had significant mode 1 energy in the lower layer. By April-June the ratio between upper and lower layer variance appeared to be approaching that which had characterized the previous summer, though there was proportionally more lower level variance than had been present.

To summarize, the mesoscale variance energy in summer 1984 fell primarily in the 8- to 12-day period band, was about twice as intense in the upper as in the lower level, and was about equally directed across- and along-shelf. Autumn 1984 saw the lowest observed variances, with distribution across the frequency band and poor directional definition. In winter 1985 variance was high, was confined primarily to the 2- to 6-day period band, was primarily in the upper level, and was both cross- and along-shelf. In spring 1985 the variance had intermediate values, was broad band and was primarily along-shelf.

The EGC/EGPF system has been characterized as having a rich mesoscale eddy field (Johannessen et al., 1983). Time-series current observations which coincided roughly with the summer 1984 MIZEX field experiment indicate, in fact, propagation of eddies or eddy-like features past moorings 1 and 2 (Figure 6). The most obvious such feature, occurring on about 28 June-2 July, was readily identifiable as an anticyclonic feature hav-
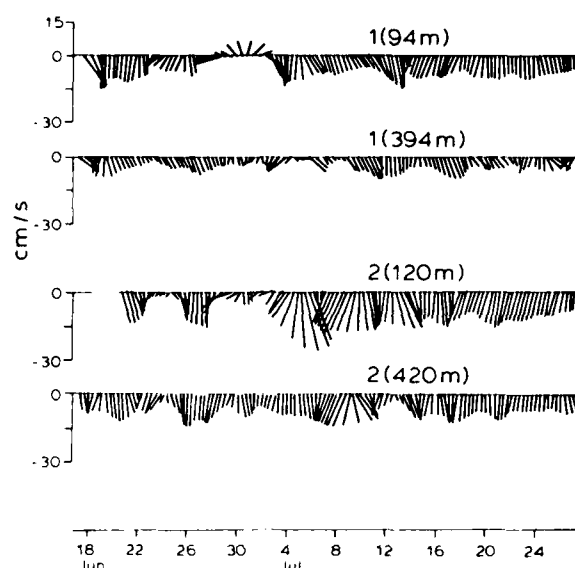

Fig. 6. Sample segment, overlapping in time much of the summer 1984 MIZEX field experiment, of low-pass (35-hour) filtered vector current plots showing signatures of eddies.

ing associated speeds of 10-15 cm/s in the upper level at mooring 1. This feature was less apparent at mooring 2, but this may have been due in part to masking by the stronger mean southward flow at the latter location than at mooring 1. A less pronounced anticyclonic eddy-like feature was apparent at mooring 2 on about 23-24 June, but was much less apparent at mooring 1. Other fluctuations which occurred throughout the time-series segment can be interpreted variously, if not unambiguously, as combinations of anticyclonic and cyclonic eddies. This pattern persisted throughout the 13-month-long current records, though eddy activity was minimal during the autumn period of low spectral energy. In general, the current observations substantiate prior claims that the region is rich in eddy activity.

Finally, the highly energetic east-west oscillations which occurred, with about a 4-day period, during February 1985 at mooring 1 deserve comment because of their high energy and uniqueness within these records (no similar features were observed at any other time during the mooring period). Current amplitudes approaching 30 cm/s were associated with these fluctuations (Figure 3), and the resulting variance dominated both the spectra (Figure 4a) and the mode 1 EOFs (Figure 5). They were evident also at mooring 2, where much of the variance had been shifted to lower

49

frequencies. They were highly baroclinic, being confined to the upper layer. Their origin is unknown.

3.3 Tidal currents

The raw (i.e. unfiltered) current records were analyzed for tidal current constituents. These analyses were carried out on a 12-month-long segment for each record using the method of Foreman (1978). The tidal currents were dominated by the semidiurnal M2 and S2 constituents. Of the smaller diurnal constituents, only K1 was significant. These three constituents are graphically shown in Figure 7. It is apparent from these plots that the semidiurnal tidal currents were greater in the upper than in the lower layers. The diurnal constituents were, conversely, slightly larger in the lower than in the upper layer. The results from the sequential monthly tidal analyses which were carried out to check the current data (see Section 2) indicated that these variations with depth were nearly constant throughout the observation period.

A short time-series plot of the non-filtered currents from mooring 1 indicates qualitatively the relative significance of tidal currents with respect to the mean and fluctuating flows (Figure 8). While the individual constituents, of which M2 is the largest with a magnitude of about 5 cm/s, are of the same order or less than the mean flow, the interactions between constituents can create large enough tidal period fluctuations to be significant when viewed within the context of short-term field experiments.

3.4 Near-inertial currents

The unfiltered current time-series plots showed well-defined semidiurnal current fluctuations (Figure 8). As noted above, much of this semidiurnal variability was due to the M2 and S2 tidal constituents. However, the observed day-to-day fluctuations in diurnal current speeds were too great to be explainable in terms of the tides. For example, sharp increases in the semidiurnal u and v currents occurred on about 29 November and 3 December. It is hypothesized that these fluctuations were due to near-inertial oscillations, which at the latitudes of the moorings should have a limiting (i.e. inertial) period of about 12.24 hours.

To test for the presence of near-inertial motions, the current records were detided and demeaned by subtracting the predicted tide and long-term mean from the unfiltered series. A sample segment of the unfiltered data, the corresponding
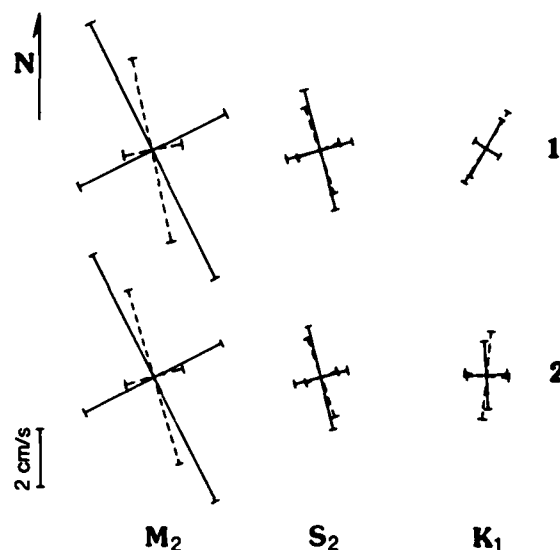
Fig. 7. Plots of tidal current ellipses (major and minor axes) for the three major observed constituents M2, S2 and K1. Upper plots are for mooring 1, and lower are for mooring 2. Solid plots are for nominal 100-m depth, and dashed plots are for nominal 400-m depth (see Table 1 for actual depths).

Fig. 8. Time plots of unfiltered u and v current components showing raw data (upper), artificially generated tidal current series (middle), and detided series (lower).

50

Observed   Detided

Variance (cm^2/s^2)

M$_2$

S$_2$
K$_2$
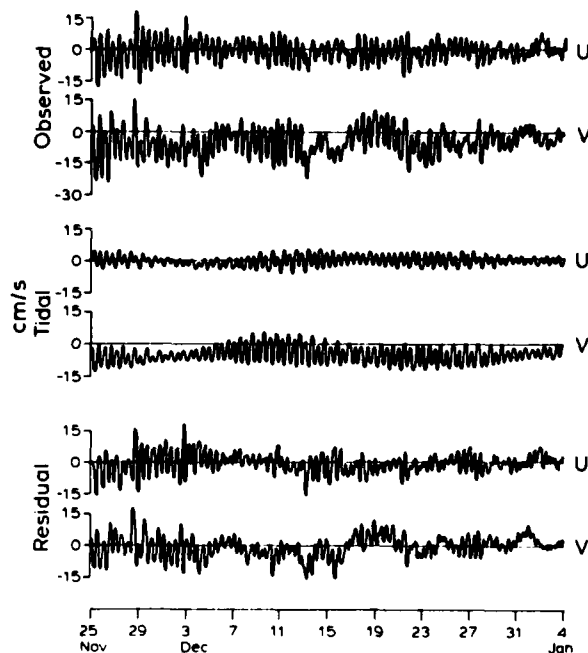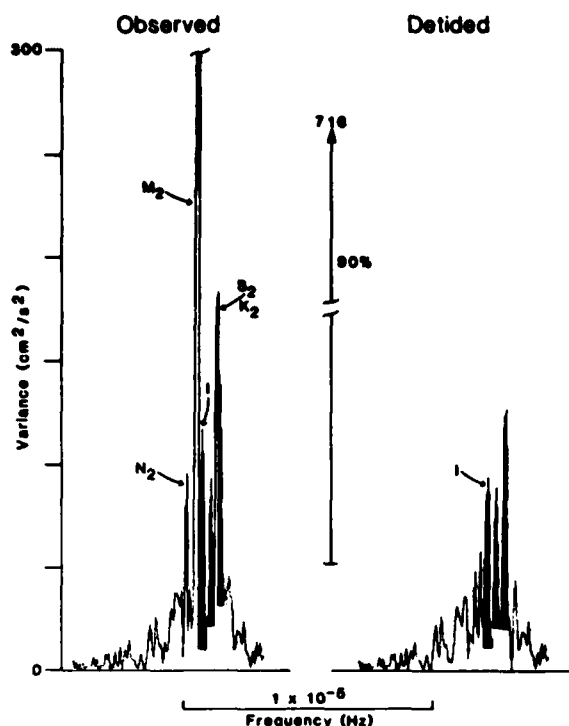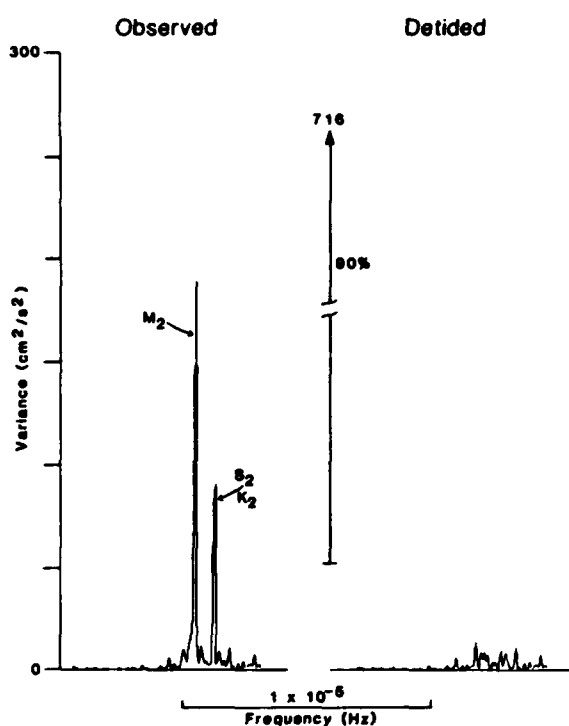
N$_2$

90%

716

300

0

1 x 10^{-5}
Frequency (Hz)

a. Upper layer; the near-inertial bands have been shaded for comparison purposes.

Observed   Detided

Variance (cm^2/s^2)

M$_2$

S$_2$
K$_2$

90%

716

300

0

1 x 10^{-5}
Frequency (Hz)

b. Lower layer.

Fig. 9. Spectra showing variance in the vicinity of the semidiurnal band before (left) and after (right) detiding the time-series by subtracting the tidal series from the raw data.

predicted tidal current and the residual currents is shown in Figure 8. Prominent semidiurnal current oscillations remain after subtraction of the tidal currents. Spectral analyses were then carried out to determine the nature of these fluctuations. The spectra were generated by ensemble averaging two 4096-point FFT's with prewhitening and a Hanning window with a 10% cosine overlap. Two examples of the spectra for the unfiltered original data and for the residual currents are presented in Figure 9. The spectra have been plotted in variance-preserving format (linear y-axis) with a linear frequency scale to display detail in the vicinity of the semidiurnal tidal band. These spectra demonstrate that most of the tidal variance has been effectively removed; this is especially evident for the deeper of the two records, where no significant semidiurnal variance remains in the residuals. The upper level residual indicates a significant (at the 90% level) variance peak at the true inertial frequency, and also two significant superinertial peaks. Nothing can be said concerning the relative magnitudes of the peaks because of the broad confidence limits; however, it is apparent that significant near-inertial variance energy was present in the upper layer currents (Figure 9a) but not in the lower layer (Figure 9b).

The presence of near-inertial motions having been established, certain features shown in the residual time-series can be explained (Figure 8). The approximate equality of the semidiurnal u and v components, coupled with an observed 90-degree phase lead of v ahead of u, are consistent with anticyclonic, circular particle orbits which typify near-inertial motions. The large semidiurnal currents which were present on about 29 November and 3 December appear to be inertial "ringing" in response to some strong forcing—probably a storm event. During these events the near-inertial motions clearly dominated the tidal currents. Such near-inertial "ringing" has been observed at sites throughout the world ocean (see for instance the current time-series shown by Anderson et al., 1983), and is generally believed to be generated by surface wind events (see for example d'Asaro, 1985). The more or less continual lower amplitude near-inertial "background" motions are of uncertain origin. They may be wind-generated and propagate into the region from elsewhere, or may be generated by such theoretically feasible means as interactions between surface or internal waves (Hasselmann, 1970). The frequency shifting to superinertial bands is likewise of uncertain origin and probably due to a combination of factors including mean current shear and lateral density gra-

51

dients, as, for instance, reported along the Oregon coast by Kundu (1976).

Virtually no near-inertial motions were present in the lower layer at either mooring; these motions were confined to the upper layers. Concentration of these motions in the upper layers is consistent with upper layer generation by winds or wave interactions. Within this context, it is also worth noting that the observations reported here were from a nominal depth of 100 m. Near-inertial motions in shallower layers or at the surface were most certainly present and were probably considerably more energetic than those described here, particularly if generated by surface forcing such as storm winds.

If there are uncertainties regarding the modes of generation of these near-inertial motions, the uncertainties concerning mechanisms for decay are still greater. One possible theoretical mechanism is, however, of special interest. Bell (1978) has hypothesized that near-inertial motions can decay through transfer of energy to the internal wave field. Since internal waves are of special significance in the marginal ice zones for a number of reasons (see for example Muench et al., 1983), further studies should perhaps focus in part on this possible mechanism.

SUMMARY

Our preliminary analysis of the overwinter 1984–85 current observations from the East Greenland Current/Polar Front system has led to the following conclusions:

1. Net flow was southward, along-isobath, for nearly the entire 13-month observation period. Cross-isobath flow was usually negligible.
2. Southward current speeds (30-day averaged) were greatest, and vertical speed differences (interpreted loosely as shear) were also greatest, during summer–autumn and were least in mid-winter. Summer–autumn upper layer (~100 m) speeds were 10–15 cm/s, and lower layer (~400 m) speeds were 5–10 cm/s. In winter the respective speeds were 5–10 and less than 5 cm/s.
3. Energetic current fluctuations occurred in the 2- to 12-day period band. In summer these fluctuations were present in both upper and lower layers and were predominantly cross-isobath, whereas in winter they were confined, with some exceptions, to the upper

layer, with episodes of both along- and cross-isobath dominance. In summer–autumn the fluctuations tended toward longer (8- to 12-day) periods, whereas in winter they were of shorter (4-day) periods.
4. Mesoscale eddies were identifiable features at the moorings throughout the observation period, and were responsible for much of the observed variance. They were predominantly anticyclonic, and were distributed similarly to the variance as to season and depth.
5. The tidal currents were dominated by the M2 (lunar semidiurnal) constituent, which had a magnitude of about 5 cm/s. The S2 and K1 constituents were also significant. The semidiurnal (M2 and S2) constituents were significantly baroclinic and decreased with increasing depth. The diurnal (K1) constituent increased slightly with increasing depth.
6. Near-inertial current oscillations were present throughout the upper (~100 m) layer records. Typical speeds were 5 cm/s, but oscillation amplitudes as great as about 15 cm/s were observed on occasion. No significant near-inertial motions were present in the lower (~400 m) layer.

REFERENCES

Anderson, I., A. Huyer and R.L. Smith, Near-inertial motions off the Oregon coast. *J. Geophys. Res., 88,* 5960–5972, 1983.

Bell, T.H., Radiation damping of inertial oscillations in the upper ocean. *J. Fluid Mech., 88,* 289–308, 1978.

d'Asaro, E.A., The energy flux from the wind to near-inertial motions in the surface mixed layer. *J. Phys. Oceanogr., 15,* 1043–1059, 1985.

Foreman, M.G.G., Manual for tidal currents analysis and prediction. Pacific Marine Science

Report 78-6, IOS Pat Bay, Sidney, B.C., 70 pp., 1978.

Hasselmann, K., Wave-driven inertial oscillations. *Geophys. Fluid Dyn., 1,* 463-502. 1970.

Johannessen, O.M., J.A. Johannessen, J. Morison, B.A. Farrelly and E.A.S. Svendsen, Oceanographic conditions in the marginal ice zone north of Svalbard in early fall 1979 with an emphasis on mesoscale processes. *J. Geophys. Res., 88,* 2755-2769, 1983.

Kundu, P.K., An analysis of inertial oscillations observed near Oregon coast. *J. Phys. Oceanogr., 6,* 879-893, 1976.

Lagerloef, G.S.E., R.D. Muench and J.D. Schumacher, Low-frequency variations in currents near the shelf break: Northeast Gulf of Alaska. *J. Phys. Oceanogr., 11,* 627-638, 1981.

Muench, R.D., P.H. LeBlond and L.E. Hachmeister, On some possible interactions between internal waves and sea ice in the marginal ice zone. *J. Geophys. Res., 88,* 2819-2826, 1983.

Paquette, R.G., R.H. Bourke, J.F. Newton and W.F. Perdue, The East Greenland Polar Front in autumn. *J. Geophys. Res., 90,* 4866-4882, 1985.

An Ice/Air Feedback Mechanism for the
Migration of the Marginal Ice Zone

P.C. CHU
Department of Geophysical Sciences
The University of Chicago, Chicago, Illinois

The aim of this study is to investigate, by means of a coupled ice/air model, the generation of strong along-ice-edge winds in the MIZ, the formation of the ice edge jet, and the instability criteria of ice drift. Ice-drift observations in the Greenland Sea from 28 April to 3 September 1978 (Figure 1) show two different types of ice motion. Oscillation occurs mostly in spring (April, May, and June) and nonoscillation takes place in summer (July and August). Ice melts and becomes thinner from winter to summer. Although ocean eddies probably produce oscillations in drift track, another relation between the pattern of ice motion and ice thickness may still exist. One purpose of the present work is to find this relation.

A possible mechanism for the air/ice interaction is presented in Figure 2. The low-level air flow generated by differential surface heating is waterward (icebreeze) and equatorward along the ice edge in both eastern Greenland and the eastern Antarctic Peninsula and influences the ice through surface air stress. However, movement of the ice edge in the MIZ toward warm water changes the thermal conditions near the surface and produces an air surface temperature gradient across the ice edge.

The ice/air interaction model depicted in this article is intended to simulate the main physical processes and to determine some instability criteria for the prediction of MIZ migration.
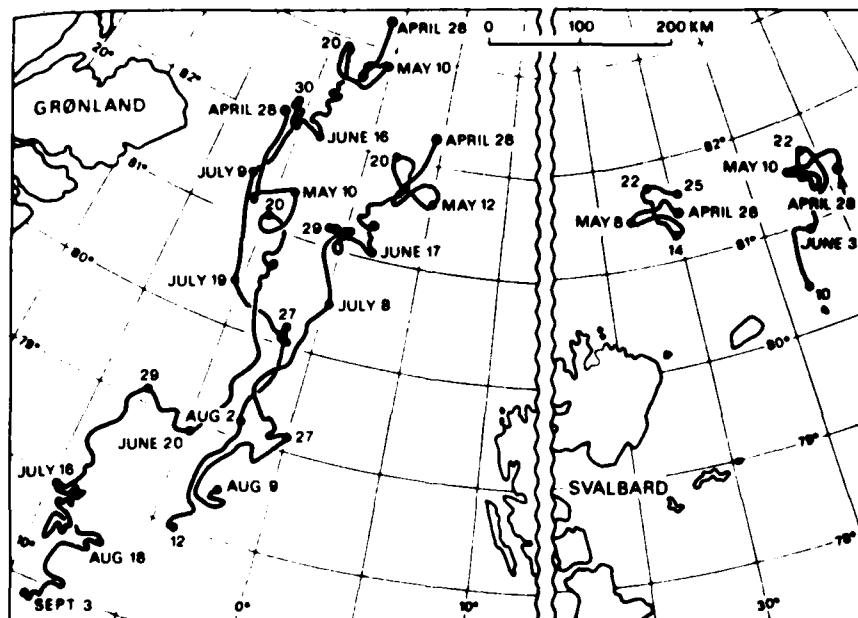

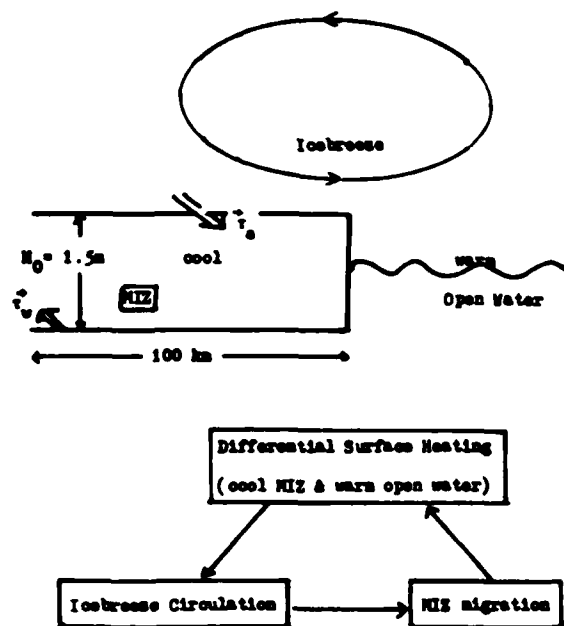*Fig. 1. Ice-drift observations in the Greenland Sea.*

54

Fig. 2. Ice/air/water coupled system.

Thermally forced boundary layer air flow

The surface isotherms, which are nearly parallel to the eastern coast of Greenland over the Greenland Sea (Prik, 1959), indicate that air temperature monotonically increases waterward near the MIZ. Such differental surface heating generates a local air flow near the MIZ. In this section we utilize a planetary boundary layer model treated by Kuo (1973) and Chu (1985) to simulate a thermally forced boundary layer air flow. The coordinate system is chosen as moving with the edge of the MIZ. The x-axis is in the cross-edge direction, and the y-axis parallels the ice edge, as shown in Figure 3. The x-coordinate's unit length is twice the MIZ width, L (200 km), and that of the vertical coordinate is $\Omega = (\nu/\Omega)^{1/2}$, where ν is the vertical eddy viscosity and Ω is the angular velocity of the earth's rotation. The line $x = \frac{1}{2}$ is located at the ice edge. The MIZ covers the zone ($0 < x < 0.5$, y) where the y-axis ($x = 0$) is near the boundary between the MIZ and the interior ice pack. It is considered that spatial variations in the MIZ are much larger perpendicular to the ice edge than parallel to it, so derivatives with respect to y are assumed to be zero. Since acceleration of the ice edge is small compared to that of the air flow, we may ignore the inertial force due to the use of a coordinate system (moving relative to the earth).

The potential temperature of air is divided into two parts: a basic state $\theta_{B*}(z)$ and perturbation θ'_*. The basic state is given by

$$\theta_{B*}(z) = \theta_{B0} + (N^2 \theta_{B0} \delta/g)z, \qquad (1)$$

where θ_{B0} is the basic air potential temperature at the surface and N is the Brunt-Vaisaila frequency.

Waterward migration of the MIZ increases the surface temperature gradient, and iceward migration of the MIZ decreases the surface temperature gradient. Surface temperature perturbation is parameterized as

$$\theta'_* = -DT_0[1 + \zeta(t)] \cos \pi x, \qquad (2)$$

where DT_0 is the mean surface temperature difference across the MIZ and $\zeta(t)$ is the nondimensional displacement of the ice edge. The coordinates and atmospheric variables are nondimensionalized by setting

$$(x_*, z_*, t_*) = (xL, z\delta, tT),$$

$$s' \equiv \theta'_*/\theta_{B0} = (DT_0/\theta_{B0})s \qquad (3)$$

$$(u_*, v_*, w_*) = U(u, v, w\delta/L),$$

$$P_* = \varrho_a(g\delta DT_0/\theta_{B0})P,$$

where

$$U \equiv g\delta DT_0/(2L\Omega\theta_{B0}) \qquad (4)$$

is the scale of the icebreeze wind and T is the time scale for the change of surface heating due to the movement of the ice edge. If we assume that the local air flow satisfies the modified Boussinesq approximation (Kuo, 1973), then the vorticity equation, the momentum equation (both in the y direction), and the heat equation for air disturbances
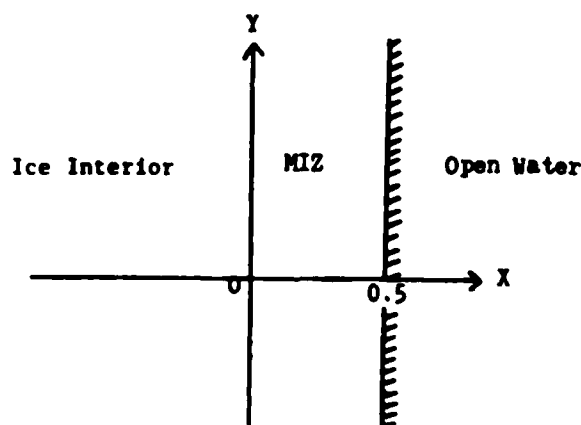

Fig. 3. The model MIZ and the coordinate system.

generated by differential heating near the MIZ are written by (Chu, 1985)

$$E\nabla_i^2 \nabla_{\zeta}^2 = f_0\, \partial v/\partial z - \partial s/\partial x, \tag{5}$$

$$E\nabla_{\nu}^2 v = -f_0\, \partial\psi/\partial z, \tag{6}$$

$$E\nabla_{\nu}^2 s = R_i\, \partial\psi/\partial x, \tag{7}$$

and

$$u = -\partial\psi/\partial z, \quad w = \partial\psi/\partial x,$$

$$\nabla_{\nu}^2 \equiv \delta^2\, \nu_h/(L^2\nu)\partial^2/\partial x^2 + \partial^2/\partial z^2,$$

$$\nabla^2 \equiv \delta^2/L^2\, \partial^2/\partial x^2 + \partial^2/\partial z^2 \doteq \partial^2/\partial z^2, \tag{8}$$

where $f_0 = \sin\lambda$, λ is the latitude, and

$$E \equiv \nu/(2\Omega\delta^2) = \tfrac{1}{2}, \quad R_i \equiv \delta^2 N^2/(4L^2\Omega^2) \tag{9}$$

are the Ekman number and global Richardson number, respectively. Eliminating ν and s from Equations 5 through 7, we find that the streamfunction satisfies the following partial differential equation:

$$(\tfrac{1}{4}\nabla_r^4 + f_0^2)\, \partial^2\psi/\partial z^2 + R_i\, \partial^2\psi/\partial x^2 = 0. \tag{10}$$

We solve Equation 10 for streamfunction ψ, and obtain the solutions of ν and s from Equations 6 and 7 after substituting ψ. The local air flow is thermally forced by differential surface heating as indicated in Equation 2; therefore, the streamfunction should be written as

$$\psi(x, z, t) = \overline{\psi}\,(z, t)\sin\pi x. \tag{11}$$

The boundary conditions in the vertical direction are derived as follows. The dependent variables should remain finite as $z \to \infty$, i.e.,

$$\mathrm{Lim}\, (|\psi|,\ |\partial\psi/\partial z|,\ |v|,\ s|) < \infty. \tag{12}$$
$$z \to \infty$$

The boundary conditions at $z = 0$ are:

$$\psi = 0, \qquad \partial\psi/\partial z = K\partial^2\psi/\partial z^2, \tag{13}$$
$$v = K\partial v/\partial z, \qquad s = -[1 + \zeta(t)]\cos\pi x,$$

where K is a measure of the effective depth of the constant stress-sublayer (Kuo, 1971). Substituting Equation 11 into Equation 10 we obtain the following sixth-order ordinary differential equation for the Fourier coefficient ψ:

$$d^6\overline{\psi}/dz^6 - 4\gamma d^4\overline{\psi}/dz^4 + 4(f_0^2 + \gamma^2)$$

$$d^2\overline{\psi}/dz^2 - 4\pi^2 R_i\overline{\psi} = 0 \tag{14}$$

where

$$\gamma \equiv \pi^2\delta^2\, \nu_h/(2L^2\nu). \tag{15}$$

The general solution of Equation 14 has the following form:

$$\overline{\psi}(z, t) = [1 + \zeta(t)]\sum_{j=1}^{6} \bar{a}_j e^{\lambda_j z}, \tag{16}$$

where the eigenvalues λ_j $(j = 1,2,...,6)$ are the roots of the succeeding sixth-order algebraic equation:

$$\lambda^6 - 4\gamma\lambda^4 + 4(f_0^2 + \gamma^2)\lambda^2 - 4\pi^2 R_i = 0. \tag{17}$$

Table 1 lists all the eigenvalues under typical stratification at three distinct latitudes (65°, 70°, and 75°). Notice that f_0^2 appears in Equation 17, so the eigenvalues in Table 1 represent both northern and

Table 1. The eigenvalues of the boundary layer air flow model at three different latitudes.

	Latitude	
65°	70°	75°
(-0.32371, 0)	(-0.31223, 0)	(-0.30378, 0)
(-1.02800, 0.87796)	(-1.04508, 0.89586)	(-1.05823, 0.90973)
(-1.02800, -0.87796)	(-1.04508, -0.89586)	(-1.05823, -0.90973)
(0.32371, 0)	(0.31223, 0)	(0.30378, 0)
(1.02800, 0.87796)	(1.04508, 0.89586)	(1.05823, 0.90973)
(1.02800, -0.87796)	(1.04508, -0.89586)	(1.05823, -0.90973)

southern polar regions. According to the upper boundary conditions listed in Equation 12 we must set up coefficients that correspond to those eigenvalues with positive real parts to zero. Consequently the general solution Equation 16, satisfying the top boundary conditions, may be written by:

$$\bar{\psi}(z, t) = [1 + \zeta(t)] \sum_{j=1}^{3} \bar{a}_j e^{\lambda_j z}, \quad (18)$$

where the eigenvalues λ_j all have the negative real parts. Substituting Equation 18 into 11 we obtain the streamfunction

$$\psi(x, z, t) = \sum_{j=1}^{3} \bar{a}_j [1 + \zeta(t)] e^{\lambda_j z} \sin \pi x. \quad (19)$$

Integrating the momentum equation (6) and heat equation (7) with respect to z after substituting Equation 19, we find that v and s are given by

$$v(x, z, t) = [\bar{b} e^{-\sqrt{2\gamma} z} - f_0 \sum_{j=1}^{3} \bar{a}_j \lambda_j$$

$$F(\lambda_j, \gamma) e^{\lambda_j z}][1 + \zeta(t)] \sin \pi x, \quad (20)$$

$$s(x, z, t) = [\bar{c} e^{-\sqrt{2\gamma} z} + \pi R_i \sum_{j=1}^{3} \bar{a}_j$$

$$F(\lambda_j, \gamma) e^{\lambda_j z}][1 + \zeta(t)] \cos \pi x. \quad (21)$$

where

$$F(\lambda, \gamma) \equiv 1/(\lambda^2/2 - \gamma). \quad (22)$$

Substituting solutions 19–21 into the vorticity equation (5) we find that

$$\bar{c} = \sqrt{2\gamma} f_0 \bar{b}/\pi. \quad (23)$$

Substituting solutions 19–21 into the surface boundary conditions listed in Equation 13, we obtain the following four algebraic equations for $\bar{a}_j$ and $\bar{b}$.

$$\sum_{j=1}^{3} \bar{a}_j = 0 \quad (24)$$

$$\sum_{j=1}^{3} \lambda_j (1 - K\lambda_j) \bar{a}_j = 0 \quad (25)$$

$$-f_0 \sum_{j=1}^{3} \lambda_j (1 - K\lambda_j) F(\lambda_j, \gamma) \bar{a}_j$$

$$+ \bar{b}(1 + K\sqrt{2\gamma}) = 0 \quad (26)$$

$$\pi R_i \sum_{j=1}^{3} F(\lambda_j, \gamma) \bar{a}_j + \sqrt{2\gamma} f_0 \bar{b}/\pi = -1. \quad (27)$$

The four constants $\bar{a}_1$, $\bar{a}_2$, $\bar{a}_3$, and $\bar{b}$ can be readily obtained by solving the four linear nonhomogeneous algebraic equations.

Figures 4–6 reveal the solutions for zero ice motion at $\lambda = 75°$, $DT_0 = 6°C$, and $N = 10^{-2} s^{-1}$. Figure 4 shows the distribution of air temperature
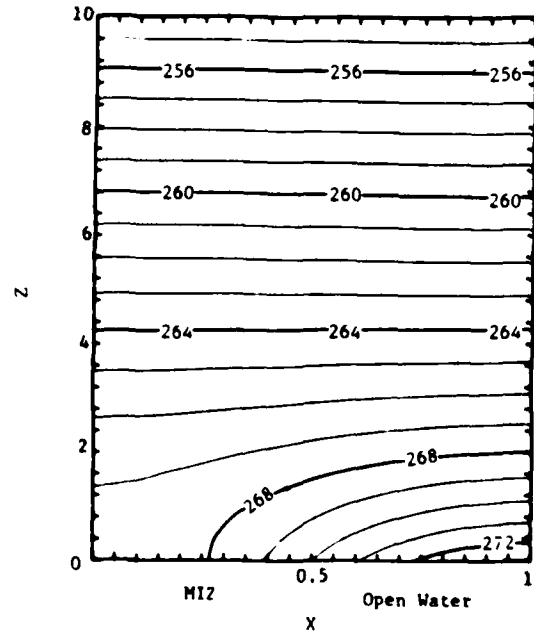

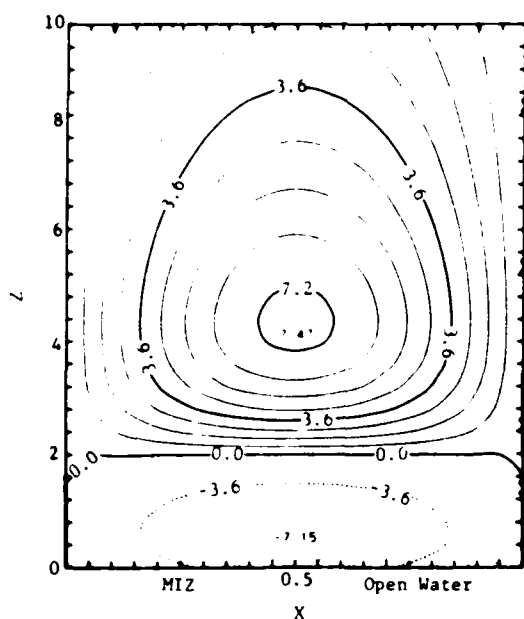Fig. 4. The distribution of air temperature (°K) in the cross-ice section.

57

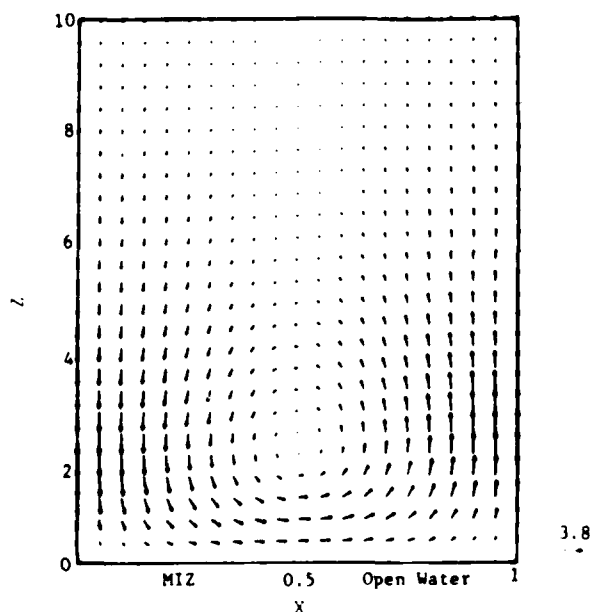Fig. 5. The distribution of thermally forced along-ice-edge winds (m s⁻¹) in the cross-ice section.

Fig. 6. Thermally forced icebreeze circulation in the cross-ice section with u in m s⁻¹ and w in cm s⁻¹.

in the cross-ice section. The horizontal temperature gradient is very deep near the ice edge and decreases with altitude. Above $z = 3$ ($z_* = 800$ m) there is almost no horizontal temperature gradient. Figure 5 shows the distribution of the wind along ice-edge v in the cross-ice section. The longshore wind is equatorward at low levels (below $z = 2$) and poleward at high levels. This strong equatorward wind along the ice edge near the MIZ (around 7 m s⁻¹) is consistent with the observations along the eastern Antarctic Peninsula (Schwerdtfeger, 1979). Figure 6 shows the cross-ice circulation. The maximum value of the ice breeze, which is around 3 m s⁻¹, is located at the ice edge.

Ice drift model

Suppose that the MIZ is considered to be pack ice with linear viscous rheology and constant shear and bulk viscosities. The MIZ has a mean thickness of H_0. The linearized momentum equation and continuity equation are written by:

$$\partial u_i/\partial t_* = (\bar{\xi} + \bar{\eta})\, \partial^2 u_i/\partial x^2$$

$$+ f v_i + (\tau_{ax} + \tau_{wx})/(\varrho_i H_0) - g \partial h_i/\partial x, \quad (28)$$

$$\partial v_i/\partial t_* = \bar{\eta}\, \partial^2 v_i/\partial x^2 - f u_i$$

$$+ (\tau_{ay} + \tau_{wy})/(\varrho_i H_0) \quad (29)$$

$$\partial h_i/\partial t_* = -(H_0/L)\, \partial u_i/\partial x, \quad (30)$$

where $f\,(= 2\Omega \sin\lambda)$ = Coriolis parameter
ϱ_i = ice density
u_i, v_i = $\mathbf{V}_i$, ice velocity
τ_{ax}, τ_{ay} = τ_a, wind stress
τ_{wx}, τ_{xy} = τ_w, water stress
h_i = ice thickness perturbation generated by forcing terms
x = nondimensional horizontal coordinate

and $\bar{\eta}$ and $\bar{\xi}$ are defined by

$$\bar{\xi} \equiv \xi/(\varrho_i H_0 L^2), \qquad \bar{\eta} \equiv \eta/(\varrho_i H_0 L^2), \quad (31)$$

where η and ξ are the shear and bulk viscosities of ice. The air and water stresses are given by

$$\tau_a = C'_a\, \mathbf{V}_a, \quad (32)$$

$$\tau_w = C'_w(\mathbf{V}_w - \mathbf{V}_i), \quad (33)$$

58

where V_a is the surface air velocity, V_w the surface water velocity, and C'_a and C'_w the dimensional air and water drag coefficients. C'_a is further given by

$$C'_a = C_a \varrho_a U [(\partial \psi_0/\partial z)^2 + v_0^2]^{1/2} \big|_{z=0, x=0.5}, \quad (34)$$

where ψ_0 and v_0 are obtained by Equations 19 and 20. In contrast to the treatments by Hibler (1984), Lepparanta and Hibler (1984), and Lepparanta (1984), the surface air and water stresses τ_a and τ_w are directly computed by the boundary layer flow model presented in the previous section. Substituting the expressions for air and water stresses (32) and (33) into Equations 28 and 29 and assuming that $V_w = 0$, we obtain

$$\partial u_i/\partial t_* = (\bar{\xi} + \bar{\eta})\, \partial^2 u_i/\partial x^2 - \bar{C}_w u_i + f v_i$$

$$\bar{C}_a u_{a0}[1 + \zeta(t)] \sin \pi x - g/L\, \partial h_i/\partial x, \quad (35)$$

$$\partial v_i/\partial t_* = \bar{\eta} \partial^2 v_i/\partial x^2 - \bar{C}_w v_i - f u_i$$

$$+ \bar{C}_a v_{a0}[1 + \zeta(t)] \sin \pi x, \quad (36)$$

where

$$\bar{C}_a \equiv C'_a/(\varrho_i H_0), \quad \bar{C}_w \equiv C'_w/(\varrho_i H_0),$$

$$u_{a0} \equiv -g\delta DT_0/(2L\Omega\theta_{B0}) \sum_{j=1}^{3} \bar{a}_j \lambda_j,$$

$$(37)$$

$$v_{a0} \equiv g\delta DT_0/(2L\Omega\theta_{B0})[\bar{b} - f_0 \sum_{j=1}^{3} \bar{a}_j \lambda_j F(\lambda_j, \gamma)].$$

Equations 30, 35, and 36 are the basic equations for ice motion. The solutions of these two equations should have the same Fourier component as the forcing terms, i.e.,

$$u_i(x, t_*) = \bar{u}_i(t_*) \sin \pi x,$$

$$v_i(x, t_*) = \bar{v}_i(t_*) \sin \pi x.$$

$$(38)$$

By definition, $\zeta(t)$ is the nondimensional ice-edge displacement in the x-direction. It is related to ice velocity by

$$Ld\zeta/dt_* = u_i(\frac{1}{2}, t_*) = \bar{u}_i(t_*). \quad (39)$$

Eliminating two of the three dependent variables, u_i, v_i, and h_i, from Equations 30, 35, and 36 we get

the following third-order equation for the coefficients:

$$[D^3 + (\alpha_1 + \alpha_2)D^2 + (\pi^2 g H_0/L^2 - \bar{C}_a u_{a0}/L$$

$$+ \alpha_1 \alpha_2 + f^2)D + \alpha_2(\pi^2 g H_0/L^2 - \bar{C}_a u_{a0}/L)$$

$$- f\bar{C}_a v_{a0}/L](\bar{u}_i, \bar{v}_i) = 0, \quad (40)$$

where

$$D = d/dt_*,$$

$$\alpha_1 \equiv \pi^2(\bar{\xi} + \bar{\eta}) + \bar{C}_w,$$

$$\alpha_2 \equiv \pi^2 \bar{\eta}^2 \bar{C}_w \quad (41)$$

The general solutions of Equation 40 have the following form:

$$\bar{u}_i(t_*) = \sum_{j=1}^{3} d_j \exp(\mu_j t_*),$$

$$(42)$$

$$\bar{v}_i(t_*) = \sum_{j=1}^{3} e_j \exp(\mu_j t_*).$$

The eigenvalues μ_1, μ_2, μ_3 are the roots of the following equation:

$$\mu^3 + (\alpha_1 + \alpha_2)\mu^2$$

$$+ (\pi^2 g H_0/L^2 - \bar{C}_a u_{a0}/L + \alpha_1 \alpha_2 + f^2)\mu$$

$$+ \alpha_2(\pi^2 g H_0/L^2 - \bar{C}_a u_{a0}/L) - f\bar{C}_a v_{a0}/L = 0. \quad (43)$$

Stability and oscillation criteria

In the present research the bulk ice viscosity ξ is taken to be twice the shear ice viscosity η. The standard values of the parameters are given in Table 2. We solve the characteristic equation (43) with different values of H_0, η, and DT_0. H_0 varies from 0.5 to 10.5 m, η from 0 to 2×10^9 kg s^{-1}, and DT_0 from 1 °C to 21 °C. The instability criterion of the MIZ migration in the ice/air-coupled model can be written by

$$\text{Re}(\bar{\mu}) \begin{cases} < 0 \text{ decaying} \\ = 0 \text{ neutral} \quad \bar{\mu} = \mu_1, \mu_2, \mu_3 \quad (44) \\ > 0 \text{ growing} \end{cases}$$

59

Table 2. The standard model parameters.

$L = 200$ km	$\nu = 5$ m^2 s^{-1}	$\nu_h = 10^5$ m^2 s^{-1}
$\Omega = 0.729 \times 10^{-4}$ s^{-1}	$g = 9.81$ m^2 s^{-2}	$K = 0.9$
$N = 10^{-2}$ s^{-1}	$\theta_{B0} = 270\,^\circ$K	$C_w' = 0.55$ kg/m^2 s^{-1}
$C_a' = 1.2 \times 10^3$	$\varrho_a = 1.29$ kg m^3	$\varrho_w = 10^3$ kg m^3
$\varrho_i = 910$ kg m^3	$U_i < 1$ m s^{-1}	$\lambda = (65\,^\circ, 70\,^\circ, 75\,^\circ)$

where $\bar{\mu}$ is the root of the cubic equation (43). The oscillation criterion of the MIZ migration is given by

$$\text{Im}(\bar{\mu}) \begin{cases} = 0 & \text{nonoscillatory} \\ \\ \neq 0 & \text{oscillatory} \end{cases} \quad \bar{\mu} = \mu_1, \mu_2, \mu_3 \quad (45)$$

Dependence of eigenvalues on parameters

We compute all the roots of Equation 43. Here μ_1 is real in the entire space, and μ_2 and μ_3 are real

for some values of (H_0, η, DT_0) and are complex conjugates for others.

Figure 7 shows the surface of $\mu_1 = 0$ in three-dimensional space (H_0, η, DT_0). This surface divides the space into two parts corresponding to growing and decaying modes. The growing mode appears when DT_0 exceeds some critical value around 2 °C, and is located in the small mean ice-thickness H_0 region. Ice motion corresponding to the eigenvalue μ_1 is nonoscillatory.

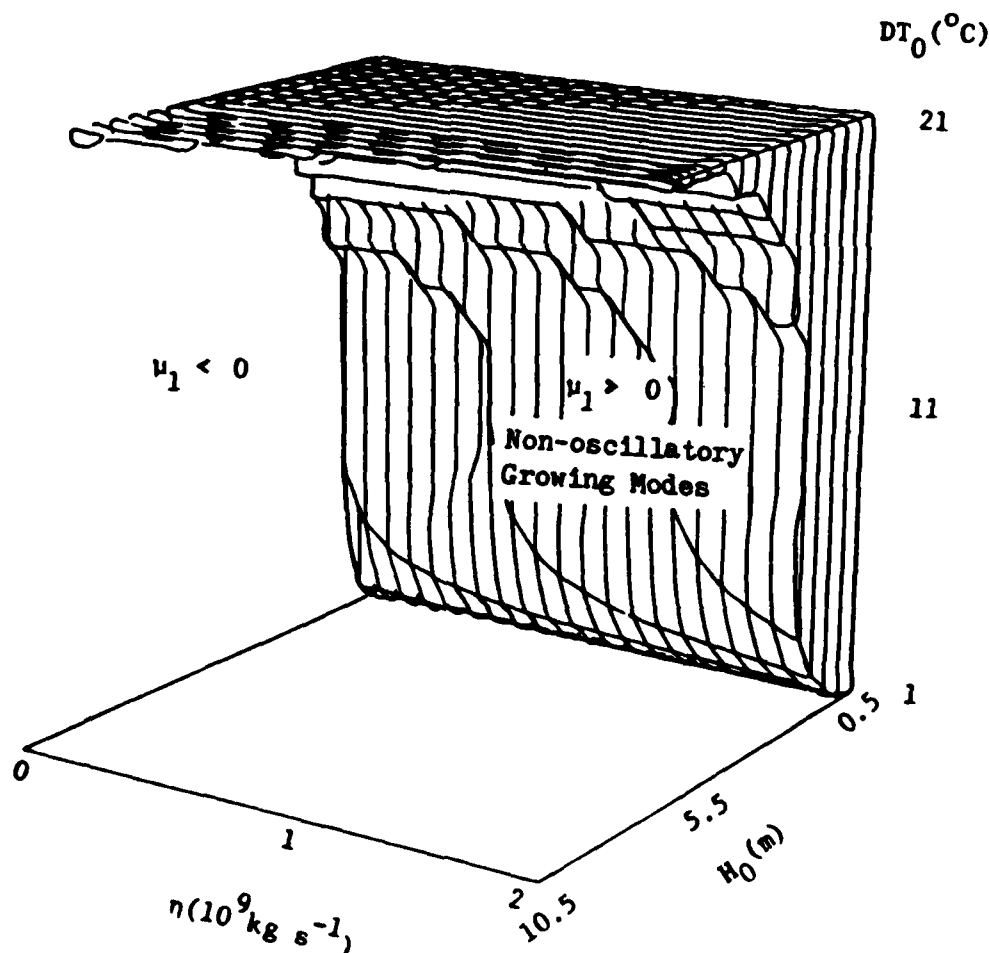Figure 8 indicates the surface of $\text{Re}(\mu_2) = 0$ [or

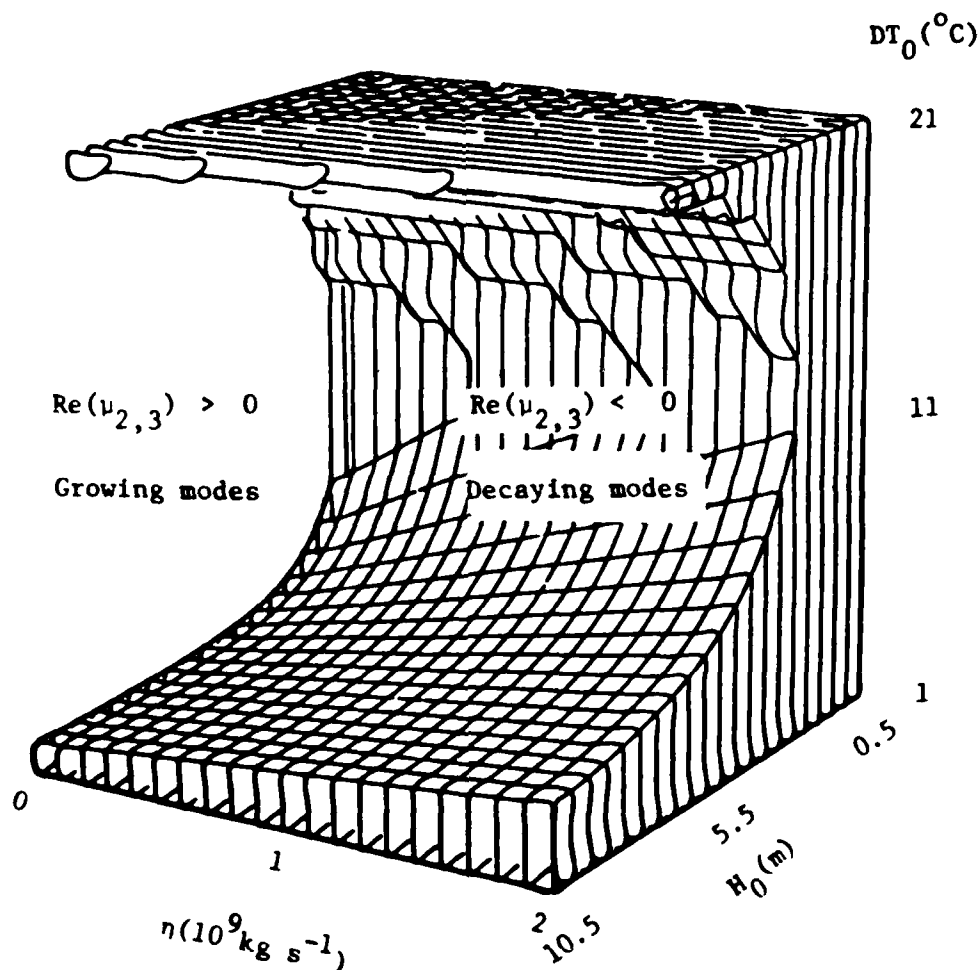Fig. 7. Separation of nonoscillatory decaying and growing modes referring to real eigenvalue μ_1.

Fig. 8. Separation of decaying and growing modes referring to eigenvalues μ_2 and μ_3.

Re(μ_1) = 0] in the parameter space (H_0, η, DT_0). This surface separates the whole space into growing and decaying parts. The growing mode is present when DT_0 exceeds some critical value that is a function of H_0 and η (in case of H_0 = 4.5 m and η = 10^9 kg s^{-1}, DT_0 = 6 °C), and is concentrated in the large mean ice-thickness H_0 region.

Figure 9 reveals the segregation of nonoscillatory and oscillatory modes relating to μ_2 and μ_3. Comparing Figure 9 with Figure 8, we find that the decaying mode of μ_2 and μ_3 is nonoscillatory, whereas the growing mode of μ_2 and μ_3 is oscillatory.

Whether ice motion grows or decays substantially depends on the parameter DT_0. When DT_0 is small, the motive force is so small that it cannot overcome the dissipative effect and does not make ice motion unstable. If DT_0 becomes large enough to overcome the dissipative forces originated by ice stress and friction, ice motion becomes larger.

Whether ice motion is oscillatory or nonoscillatory largely depends on parameter H_0. In cases of small H_0, the restoring force is so small that it cannot balance the motive force and cannot produce oscillations. However, when parameter H_0 exceeds some critical value (which varies with DT_0 and η) and becomes large enough to balance the motive force brought on by the ice breeze generated by surface temperature difference, the ice motion becomes oscillatory.

For the nonoscillatory growing mode, the time during which ice doubles its speed is computed by

$$T_1 = \ln 2 / \mu_1 \qquad (\mu_1 > 0). \qquad (46)$$

If H_0, η, and ξ are assigned as commonly used values:

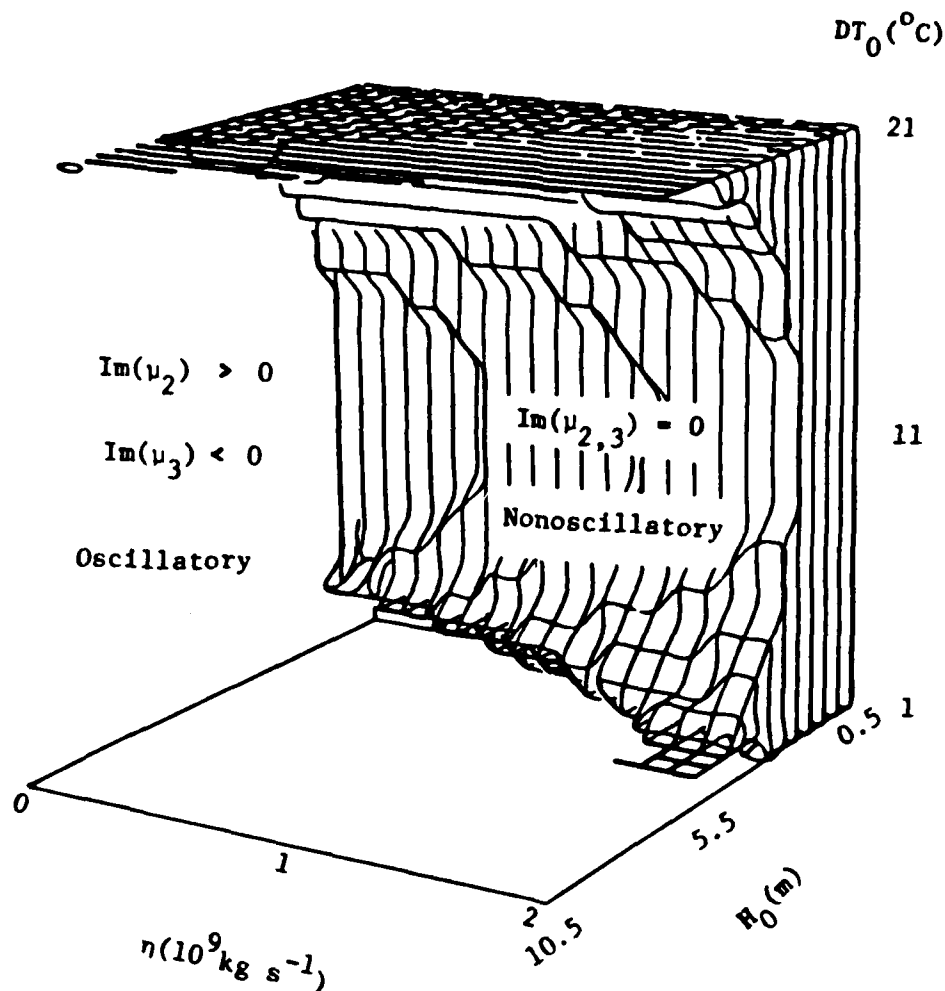$$H_0 = 1.5 \text{ m}, \quad \eta = 10^9 \text{ kg s}^{-1}, \quad \xi = 2 \times 10^9 \text{ kg s}^{-1},$$

61

DT_0 (°C)

21

$Im(\mu_2) > 0$

$Im(\mu_3) < 0$

$Im(\mu_{2,3}) = 0$

11

Nonoscillatory

Oscillatory

0.5 1

5.5

H_0 (m)

0

1

2

10.5

$\eta(10^9 kg\ s^{-1})$

Fig. 9. Separation of nonoscillatory and oscillatory states referring to eigenvalues μ_2 and μ_3.

The doubling time treated as a function of DT_0 is shown in Figure 10, which displays a decrease of T_1 with an increase of DT_0. T_1 changes from 7.3 hr to 0.73 hr as DT_0 varies from 6 °C to 16 °C. It takes only 12.4 hr for the ice velocity to increase from 6 cm s⁻¹, which is a steady-state estimation, to 20 cm s⁻¹ when $DT_0 = 6$ °C.

The oscillatory growing mode is ice motion due to μ_2 (or μ_3), whose real part is positive.

$$Re(\mu_2) = Re(\mu_3) > 0,$$

the growth rate $Re(\mu_{2,3})$ increases with an increase of DT_0 (increase of forcing term), with an enlargement of H_0 (increase of restoring force), and with a reduction of η (decrease of dissipation). With $DT_0 = 6$ °C, $\eta = 10^9$ kg s⁻¹, and $H_0 = 4.5$ m, the growth rate is 0.22×10^{-4} s⁻¹ and the corresponding doubling time is 8.75 hr. The period of growing oscillatory mode, defined by

T_1 (hr)

25

20

15

10

5

0

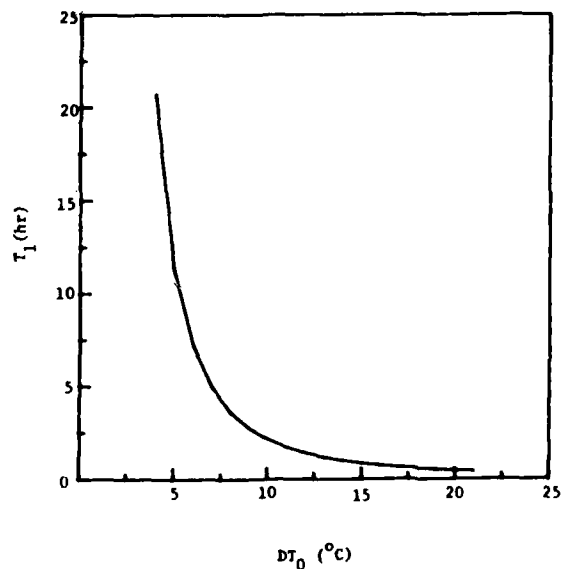5   10   15   20   25

DT_0 (°C)

Fig. 10. Dependency of doubling time on DT_0 for the nonoscillatory growing mode.
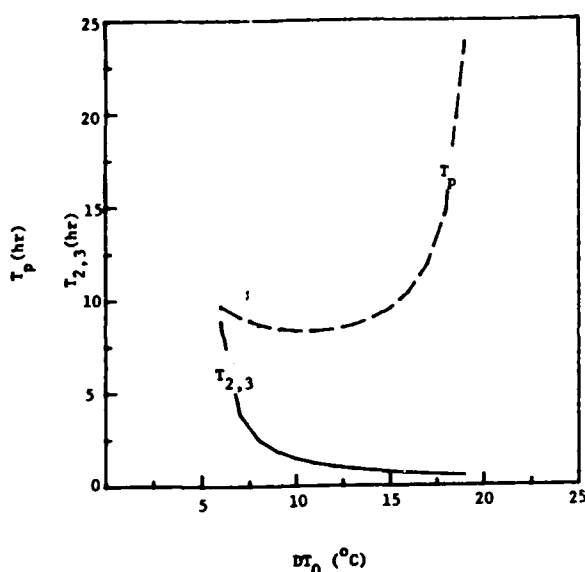
62

Fig. 11. Dependency of doubling time and period on DT_0 for oscillatory growing mode.

$$T_p = 2\pi/|\mathrm{Im}(\mu_{2,3})| \qquad (47)$$

is 9.7 hr.

Figure 11 shows the growth rate and period as functions of DT_0 for $H_0 = 4.5$ m and $\eta = 10^9$ kg s^{-1}. The growth rate decreases monotonically with an increase of DT_0. However, the period decreases slightly when DT_0 varies from 6 °C to 10 °C, and then increases with DT_0 rapidly. When $DT_0 = 19$ °C, the period is nearly one day.

Conclusion

This ice/air-coupled model is intended only to depict the mesoscale processes of ice/air interaction in the MIZ. The synoptic scale pressure gradient associated with the semi-permanent Icelandic low may in addition produce equatorward winds in the Greenland Sea, and large-scale ocean currents near the East Greenland Sea or the Antarctic Peninsula may drive ice drift. These processes are, however, beyond the scope of the current research. Nevertheless, when the ice to open water temperature gradient is strong, the mesoscale feedback mechanism discussed here may become as strong, or stronger, than the synoptic scale and oceanic forcings.

The equatorward and waterward surface winds near the MIZ in the Greenland Sea and the east Antarctic Peninsula are thermally generated by differential surface heating over ice and water. The surface wind has its maximum speed along the ice edge. The component of surface wind parallel to the ice edge can reach 7 m s^{-1} when the temperature gradient in the cross-ice direction is chosen as 0.03 °K km^{-1}. This agrees with the observational results at the east Antarctic Peninsula reported by Schwerdtfeger (1979).

The migration of the MIZ is forced by local winds generated by differential surface heating over ice and water near the ice edge. The ice velocity V_i has sinusoidal forms (38), showing an ice edge jet. The ice velocity has its maximum at the ice edge and decreases iceward. This implies that the ice edge jet is produced indirectly by the thermal effect of the ice/water contrasts.

The ice motion has two bifurcations. It first bifurcates into decaying and growing modes, depending on th mean surface temperature difference over ice and water, DT_0. When DT_0 is small, the decaying mode predominates. However, when DT_0 exceeds some critical value (i.e., 6 °C as $H_0 = 4.5$ m and $\eta = 10^9$ kg s^{-1}, and 2 °C as $H_0 = 1.5$ m and $\eta = 10^9$ kg s^{-1}), the growing mode appears. The growing mode further bifurcates into nonoscillatory and oscillatory states, depending on ice properties. In cases of small ice thickness, which causes an inadequate restoring force and generally occurs in summer, the ice motion is nonoscillatory. In cases of large ice thickness, which generates an adequate restoring force and is usually present in winter, the ice motion is oscillatory.

This research provides a possible way to predict the MIZ migration. The procedure is as follows:

a) Observe surface temperature difference DT_0 and determine the ice properties, i.e., H_0 and η.

b) Use Figures 8 and 9 to determine the pattern of motion, i.e., growing or decaying, oscillatory or nonoscillatory, etc.

c) Employ Figures 10 and 11 to determine the growth rate and period (in case of the oscillatory state).

d) Observe initial ice velocity.

e) Make a prediction of MIZ migration according to the initial ice velocity, growth rate, and period (for the oscillatory state).

REFERENCES

Brown, R.A., Planetary boundary layer modeling for AIDJEX. In *Sea Ice Processes and Models.*

63

University of Washington Press, 387-401, 1980.

Chu, P.C., A boundary layer theory of coastal desert formation and seabreeze circulation. Ph.D. thesis, The University of Chicago, 194 pp., 1985.

Glen, J.W., Thoughts on a viscous model for sea ice. *AIDJEX Bull., 2,* 18-27., 1970.

Hibler, W.D., III, Ice dynamics. CRREL Monograph 84-3, 52 pp., 1984.

Kuo, H.L., Axisymmetric flows in the boundary layer of a maintained vortex. *J. Atmos. Sci., 28,* 20-41, 1971.

Leavitt, E., Surface-based air stress measurements made during AIDJEX. In *Sea Ice Processes and Models.* University of Washington Press, 419-429, 1980.

Lepparanta, M. and W.D. Hibler III, On the role of ice interaction in marginal ice zone dynamics. *MIZEX Bulletin III,* USA Cold Regions Research and Engineering Laboratory, Special Report 84-7, pp. 23-29, 1984.

Macklin, S.A., Wind drag coefficient over first-year sea ice in the Bering Sea. *J. Geophys. Res., 88,* 2845-2952, 1983.

McPhee, M.G., The effect of the oceanic boundary layer on the mean drift of pack ice: Applica-

tion of a simple model. *J. Phys. Oceanogr., 9,* 388-400, 1979.

Overland, J.E., H.O. Mofjeld and C.H. Pease, Wind-driven ice drift in a shallow sea. *MIZEX Bulletin III,* USA Cold Regions Research and Engineering Laboratory, Special Report 84-7, pp. 49-53, 1984.

Pease, C.H., S.A. Salo, and J.E. Overland, Drag measurements for first-year sea ice over a shallow sea. *J. Geophys. Res., 88,* 2853-2862, 1983.

Prik, Z.M., Mean position of surface pressure and temperature distribution in the Arctic. *Tr. Arkticheskogo Nauchn.-Issled. Inst., 217,* 5-24 (in Russian), 1959.

Schwerdtfeger, W., Meteorological aspects of the drift of ice from the Weddell Sea toward the mid-latitude westerlies. *J. Geophys. Res., 84,* 6321-6328, 1979.

Smith, S.D., E.G. Banke, and O.M. Johannessen, Wind stress and turbulence over ice in the Gulf of St. Lawrence. *J. Geophys. Res., 75,* 2803-2812, 1970.

Vinje, T.E., The drift pattern of sea ice in the Arctic with particular reference to the Atlantic approach. In *The Arctic Ocean,* John Wiley and Sons, New York, 83-96, 1982.

The Planetary Boundary Layer in the Marginal Ice Zone

ROBERT A. BROWN

Department of Atmospheric Sciences, University of Washington
Seattle, Washington 98195

The object of the Marginal Ice Zone Experiments (MIZEX) meteorology analysis program is to obtain information for all scales of atmospheric motion that are directly affected by the marginal ice zone (MIZ) or *vice versa*. The relatively abrupt transition from pack ice to ocean surface provides an excellent location for investigating the air modification in the Planetary Boundary Layer (PBL) flow and the effects on the surface. The most significant parameter of interaction between air and pack ice or sea surface is the aerodynamic drag parameter, $C_D = \tau/\varrho U^2$. This is best obtained from measurements of stress, τ and U, at the surface. However, the measurement of stress is difficult and requires fairly complicated measurements. Consequently, stress data over the pack ice or the ocean has rarely been obtained and drag coefficients established at smooth land sites were used. Within the past decade, experiments have revealed new trends in the variation of the drag coefficient over these surfaces.

One of the goals of air/sea interaction modellers has been to get an upper boundary condition for the oceanic flow, the stress. Traditionally, this upper boundary condition, the surface stress, was used as a free parameter in dynamic models. The oceanic problem was simply solved or modelled with respect to the input forcing represented in the drag coefficient, and this constant could be looked up somewhere. In the case of a large experiment, all that was needed was to find a wind measurement in the region, square it, multiply by constant density, and obtain an estimate of the stress for the entire area. This had the advantage that if things didn't work out right in the model, one could always change the C_D as a free parameter. This was probably good enough in some cases, and it may have been justified by the difficulty that atmospheric scientists seemed to be having in determining the value of C_D over the ocean. However, there are many current oceanic models that

deal with small scales and are accurate enough to respond to variations in C_D that naturally occur.

In field experiments, the stress is usually obtained at a point using sophisticated turbulence measurements, theory, and analysis. The eddy correlation method requires high-frequency turbulence measurements to determine the time average of the velocity fluctuations correlation, $\overline{u'w'} = \tau/\varrho$. This uses sophisticated instruments that are difficult to maintain in the harsh environment of the MIZ. Nevertheless, enough measurements have been made over pack ice to give an approximation of the stress based on a single mean wind measurements using the drag coefficient method. The problem is then to extrapolate these data to the mesoscale and synoptic scale. This is done with a mixture of theory and data. The theory defines similarity parameters that can relate point values of wind, stress, and heat flux to large-scale mean flow parameters, such as horizontal pressure and temperature fields. Unfortunately, most of the similarity parameters are not universal. They vary with PBL stratification and, to a lesser degree, with surface roughness and windspeed. All of these variations become particularly significant in the MIZ, since these factors change dramatically in this region.

The model

In applications, initially the drag coefficient is often assumed to be constant. The surface stress then depends only on the surface wind speed, density being essentially constant within the boundary layer. Moreover, since surface wind measurements are generally not widely available, it is often necessary to obtain the surface wind from the geostrophic windfield. The latter can be approximated from a surface pressure field by assuming vertical coherence of the pressure gradient. This condition is a good approximation as long as significant baroclinicity (the horizontal temperature gradient)

doesn't exist. If it does, then a value for the horizontal temperature field is needed to calculate this influence (the thermal wind). PBL similarity theory provides a direct link between the synoptic flow, G, and the surface stress. The surface friction velocity, $u^* = \sqrt{\tau/\varrho}$, can be used to define the geostrophic drag parameter, u^*/G. The angle of turning between the geostrophic flow and the surface wind or stress, α, can also be calculated. All that is required is a set of good measurements of u^*, G, and/or U_{10} to evaluate the similarity parameters A' and B in

$$\frac{kG}{u^*} (\sin\alpha) = -B$$

$$(1)$$

$$\frac{kG}{u^*} (\cos\alpha) = -A'$$

where B is a constant and $A' = A + \ln(ku^*/fz_0)$ is a function of surface roughness, as represented in the roughness parameter z_0. k is von Karman's constant ~ 0.4, and f is the Coriolis parameter.

The data

To illustrate the history of oceanic drag coefficients, Figure 1 is a montage of a collection of anonymous published results of C_D vs. surface windspeed and stratification parameter, z/L, where L is the Obukhov stratification parameter, which must be designated along with C_D. Scatter is a problem in the data. C_D is not constant; it varies with windspeed, stratification, and surface roughness. These effects have been slowly identified only from many stress measurements. There is variation in C_D with magnitude of U due to surface roughness (wave spectrum) changes. Stratification measurements were generally not available, since they require measurements of vertical temperature gradients, or at least air/surface temperature differences. Early graphs of C_D vs. roughness consequently were even more scattered. Most plots of C_D vs. any single variable—stratification, roughness, or windspeed—will generally show large scatter due to the difficulty in eliminating the other effects. Since this ancillary data is not generally available, most MIZ and polar measurements have intrinsic large error.
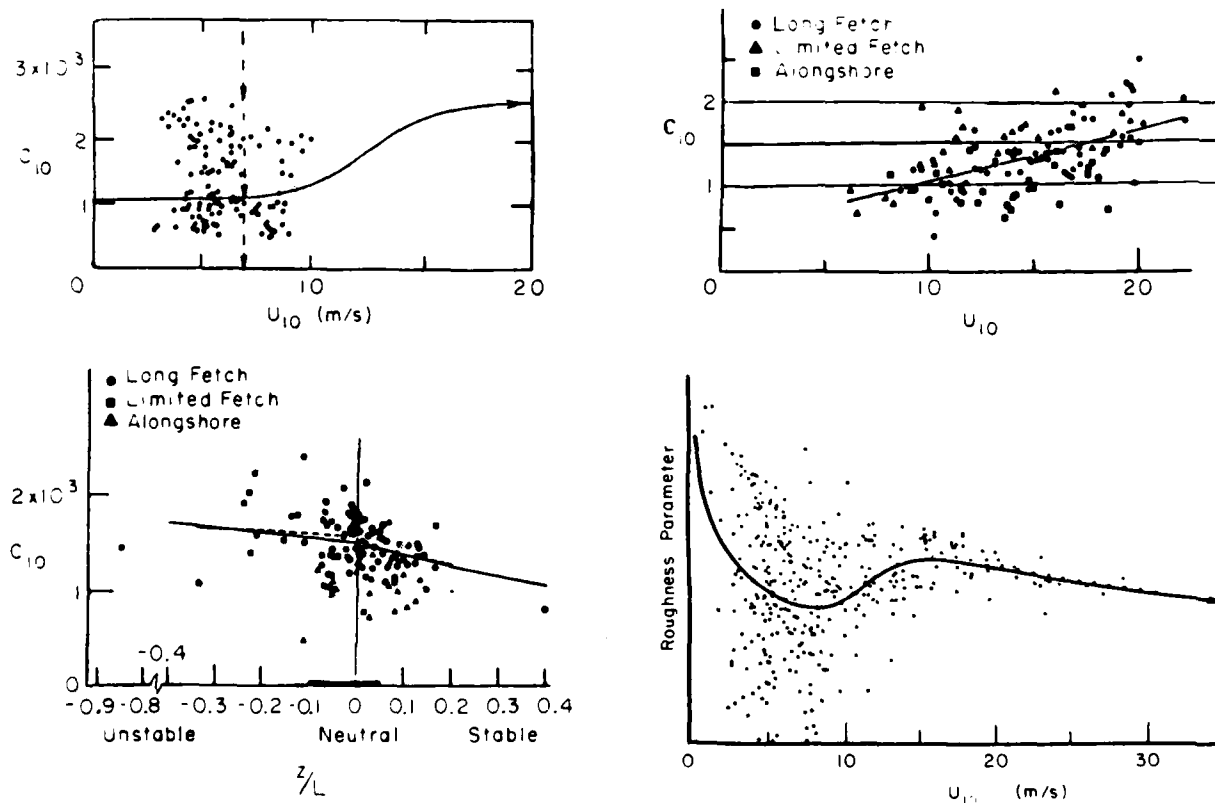

Fig. 1. The results of experimental measurements of the 10-m drag coefficient over the ocean and the roughness parameter z_0 vs. mean wind speed or stratification parameter.
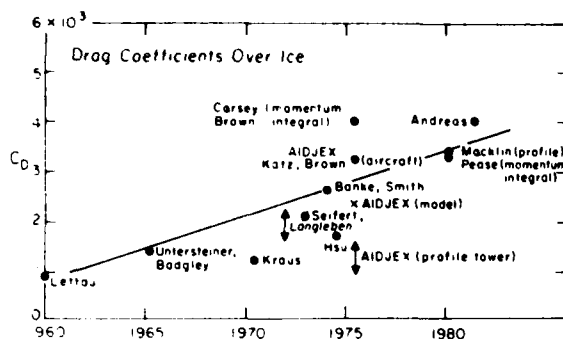
66

Fig. 2. *A representative summary of drag parameters measured over pack ice.*

Fig. 3. *Drag parameters calculated in the JASIN experiment on the weathership* Meteor. *The solid line is an average found at the Bedford Institute tower.*

Figure 2 shows representative values of C_D taken over the ice during the past few decades. A more comprehensive compilation by Overland (1985) shows the same trend. The drag seems to be increasing with time. This increase is actually due to two factors: better control in measurements, and data taken in increasingly rough ice areas. Up to 1975, measurements were usually taken on very large, very smooth ice floes. During AIDJEX (Arctic Ice Dynamics Joint Experiment), several different measurements of stress were taken. The traditional methods: the profile and eddy correlation with sonic anemometer data, all were taken on a very large, smooth ice floe, and yielded values of $1-2 \times 10^{-3}$. There were indications of higher values. Banke and Smith (1973) took measurements in rougher areas and obtained values up to 2.4×10^{-3}. Aircraft data taken during AIDJEX included large horizontal averages and yielded extrapolated values of $C_D = 2.5 \times 10^{-3}$ (Katz, 1980). Another method, which incorporated the entire boundary layer wind profile, was the momentum integral method from Brown (1974). This was used with acoustic sounder data by Carsey (1980) to obtain C_Ds up to 3.1×10^{-3}. In recent years, Pease (personal communication) (using a momentum integral), Macklin (1983) (a profile tower), Walter et al. (1984) (aircraft), and Andreas et al. (1984) have worked in the MIZ, obtaining large C_D for this rough region.

During the 1970's, several large-scale experiments were conducted where C_D was measured accurately in high winds over the ocean. Figure 3 is a representative data set from one of these experiments, the Joint Air-Sea Interaction Experiment (JASIN), calculated by Large and Pond showing a two-regime behavior of C_D with windspeed. The drag coefficient increases with windspeed at high winds—the most important case. The next illustra-
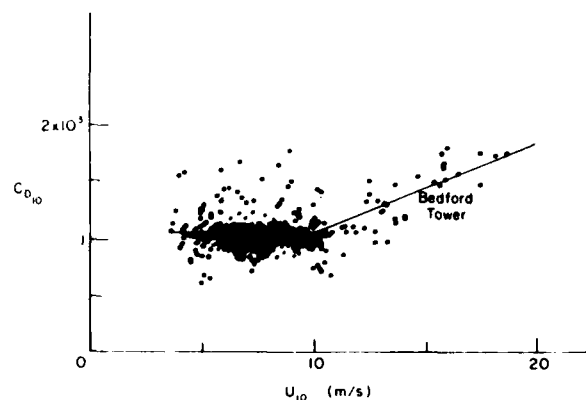
tion, Figure 4, shows a similar two-regime behavior of heat flux with respect to stratification. There is a dramatic change across neutral stratification. Since momentum is transported by the same turbulent eddies, one might expect a similar behavior in stress variation with stratification. Heat and momentum flux (stress) depend on the turbulence distribution in the PBL, which depends on surface roughness (mechanical mixing), stratification (via convective instabilities, buoyancy effects), and windspeed (via dynamic instabilities, secondary flows).

Using the observations to determine the similarity parameters resulted in large scatter in the similarity functions. The A's and B's must be determined by measuring all other parameters in Equation 1: u^*, G, k, and z_0. Since they were some (unknown) function of stratification, a parameter must be determined from measurements
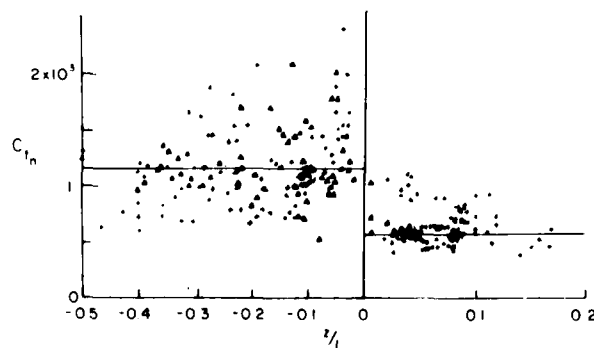

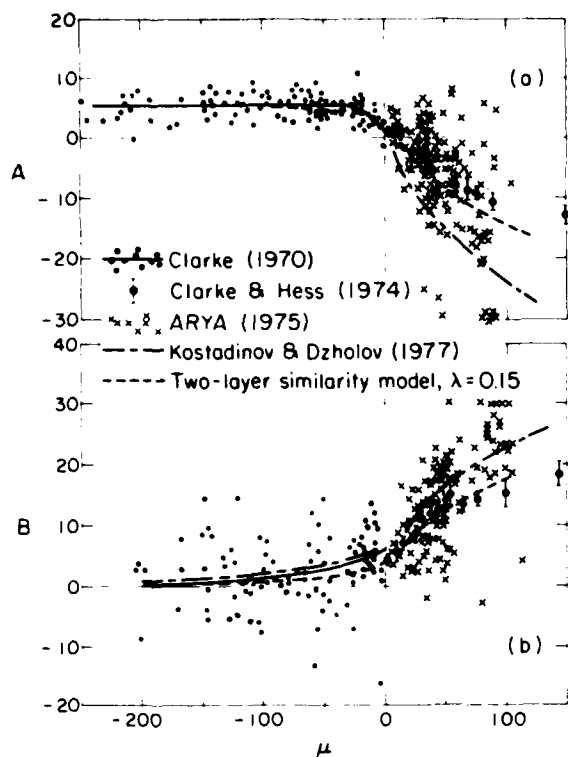Fig. 4. *Same as Figure 3 for the heat flux parameter vs. the stratification parameter* z/L.

67

Fig. 5. Similarity functions vs. stratification parameter μ = lu*/fL. Taken from Brown (1982).

Fig. 7. Air photo of ice ridges near the AIDJEX camp, 1976. This ice ridge is about 2 m high, 10 km long.

Fig. 6. Ice feathers on pack ice. The width at the nearest point is about 1 meter.

of heat flux. Figure 5 shows typical data-produced A and B vs. stratification. It would appear that we are not much better off with this method. However, the scatter in this formulation may often result from improper representation of the turbulence. When secondary flows in the Ekman layer are included in the turbulence analysis, the (modified) similarity laws offer good parameterization of the stress.

Figures 6 through 8 show some variation in the surface roughness of the ice. Figure 6 is a form of ice feathers (frosting); it is probably not common enough to worry about, but it is illustrative of how varied the ice surface can be. Figure 7 shows the pack ice near AIDJEX. This is a relatively smooth floe, but it contains ridges 1-2 m high separated by a few hundred meters to kilometers. Figure 8 shows the profile tower at AIDJEX, 26 m high, used to measure stress. Even this tall (for the Arctic) tower reaches only about 5% of the PBL, and reflects the surface roughness characteristics only in the vicinity of the tower—a relatively smooth floe. Figure 9 shows stress data obtained from this tower, plotted versus a stratification parameter, $\mu = ku*/fL$. L is the Obukhov parameter $= ku^{*}/gH_0$; H_0 is the heat flux. The lines are from the
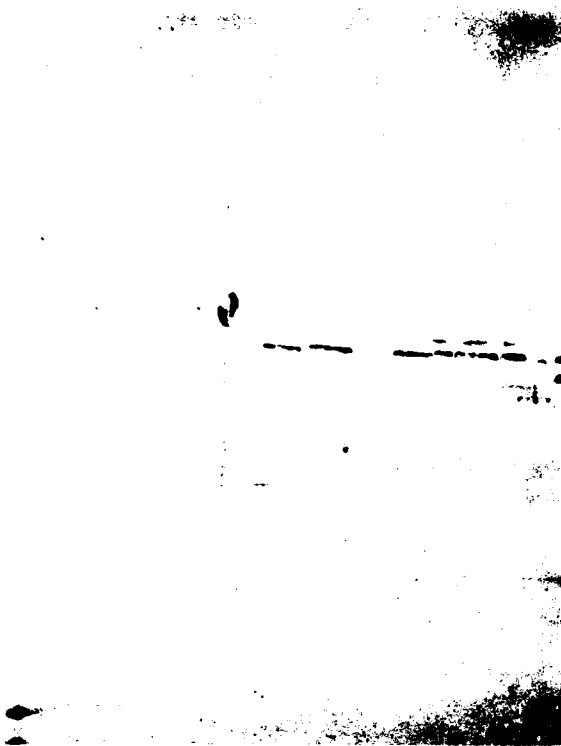
68

theory of Brown (1981). The scatter is typical. There is a clear trend toward smaller $u*/G$ for stable stratification. Since stress is proportional to $u*^2$, the change in stress (dynes/cm^2) is significant.

The general picture over the ocean is shown in Figure 10. C_D vs. surface wind magnitude at different air/sea temperature differences are shown for many experiments. The heavy line is the composite parametric curve used in the model for neutral stratification. The heavy dashed lines are the predicted curves with stratification effects. Again, the data did not have good stratification information, and this could account for some of the differences, e.g. the Davidson data were in somewhat stable stratification (personal communication).

The PBL model

Figure 11 illustrates one of the characteristics of the MIZ PBL, the omnipresence of cloud streets when wind > 7.0 m s^{-1}. In the past decade laboratory experimenters have used new flow visualization techniques to discover a fundamental characteristic of turbulent flow—the fact that often large, organized eddies or secondary flows can exist within the fully developed turbulent flow (e.g., Meyer, 1981). This happens most often when the system is in a rotating frame of reference. The clouds provide excellent flow visualization in the atmosphere, and the rotating frame of reference is built in. Furthermore, there is an analytic solution for the mean flow: the Ekman spiral. There is also an analytic solution for the mean flow containing

Fig. 8. AIDJEX meteorological tower. It was 26 m tall and was frequently climbed. The smooth ice of the large (10-km) drift is broken only by the black drums at the fuel depot.
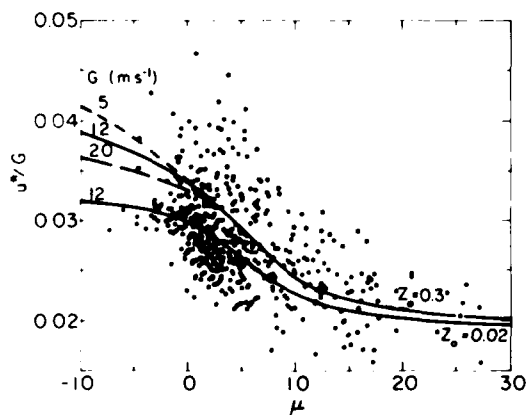

Fig. 9. Geostrophic drag parameter values obtained from the AIDJEX tower by E. Leavitt. The lines are from the theory of Brown (1981) for various geostrophic windspeeds G and roughness parameters z_0.
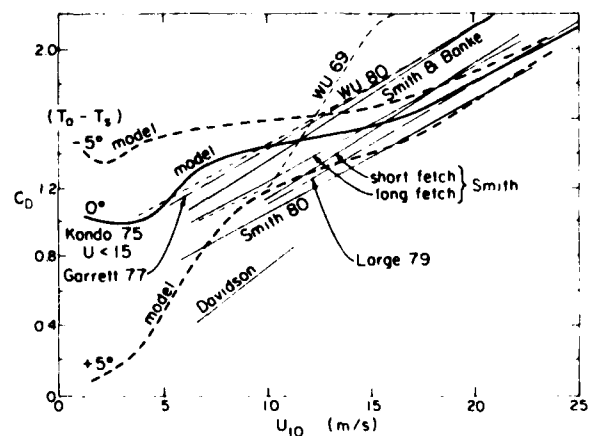

Fig. 10. The drag parameter vs. windspeed summarized for many experiments. The model function is shown for neutral, stable, and unstable stratification. Taken from Brown and Liu (1982).
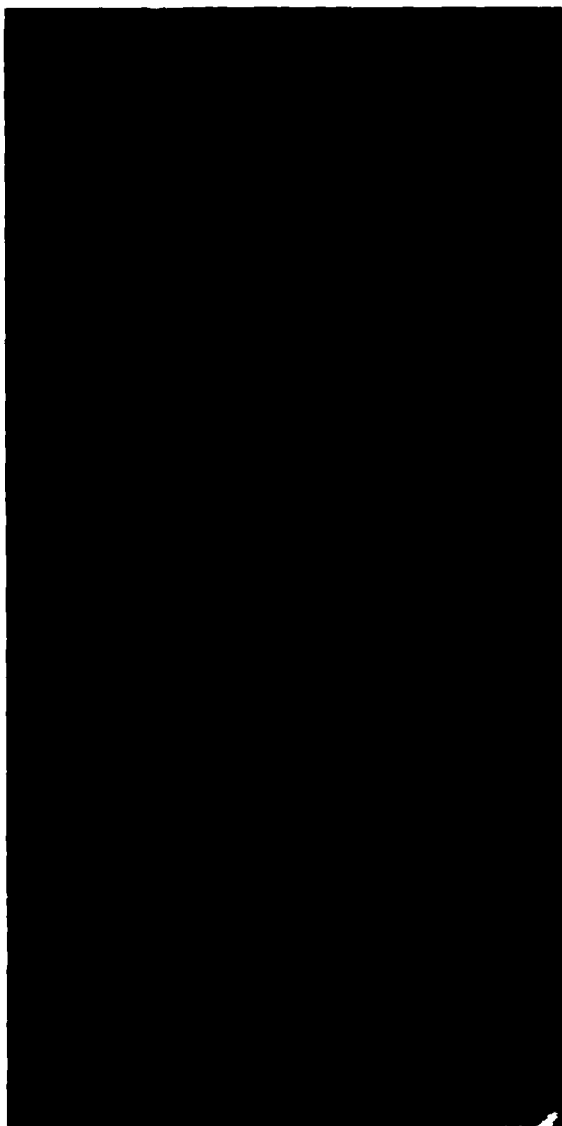
69

Fig. 11. Satellite photograph of northerly flow off the pack ice over the ocean in the Bering Sea, February 1981. The cloud rows occur in the convergence and upward motion of the underlying secondary flow roll circulation in the PBL. The wavelength is about 5 km. The stratification is near-neutral over the pack ice and convectively unstable over the ocean. The flow becomes cellular at low Reynolds numbers over the ocean.

the secondary flow large eddies: the modified Ekman spiral. Figure 12 is a sketch of the predicted flow pattern in the PBL. Condensation occurs in the updraft regions, where the convective activity and the moisture flux are enhanced. The lateral wavelength of these vortical eddies is about 2-6 km, depending on stratification in the layer. This

means that there is a significant variation in the vertical wind profile if taken at any point in the secondary vortices, such as A, B, or C in the figure. The expected vertical wind profiles are shown in Figure 13. These are the "mean" winds, which would be determined from a radiosonde launched into the PBL's vortical eddies, or rolls. Each profile is different from the mean profile, which would result from averaging across many rolls. One expects similar variation in the phase of heat, momentum, and any passive agent such as CO_2. The onset of secondary flow and enhanced flux regions as the wind gradients increase may account for the jump in momentum and heat flux indicated by Figures 3 and 4. While it is impractical to launch enough radiosondes to obtain an average, an aircraft can traverse the rolls and readily obtain average flows.

The influence of the boundary reaches quite deep into the atmospheric flow, from 100s of meters to several kilometers, depending on windspeed, surface roughness, and stratification. The scatter in point measurements with radiosonde balloons prevented any meaningful understanding of the upper PBL flow. Consequently, most data are from the surface layer. The logarithmic velocity profile and its variation with stratification for this layer over land have been thoroughly parameterized.

Our boundary layer model incorporates both surface and modified Ekman boundary layer solutions, patching them together at some height around 15% of the height of the boundary layer. Since the rolls, and consequently the mean flow dynamics, vary with convective energy input, both layers vary with stratification. Figure 14 is a sketch showing the predicted flows in each layer. The continuous velocities from the two-layer model include the contributions from surface layer stratification, PBL stratification, surface roughness, and thermal wind, as given by Brown and Liu (1982). Note that the secondary flows are a result of dynamic instabilities in the basic Ekman flow, and are always present above a threshold wind velocity of about 7 m s⁻¹ neutral—less when convection is important, and not at all when significant stable stratification exists (local $Ri \geq 0.25$).

When the equations for patching the modified Ekman solution to the log solution are written, the similarity characteristics of the PBL emerge. The "classic" similarity relations for PBL parameterization of the neutral, stable, barotrophic layer are given in (1). When stratification effects are included, the similarity equations become (Brown, 1981)
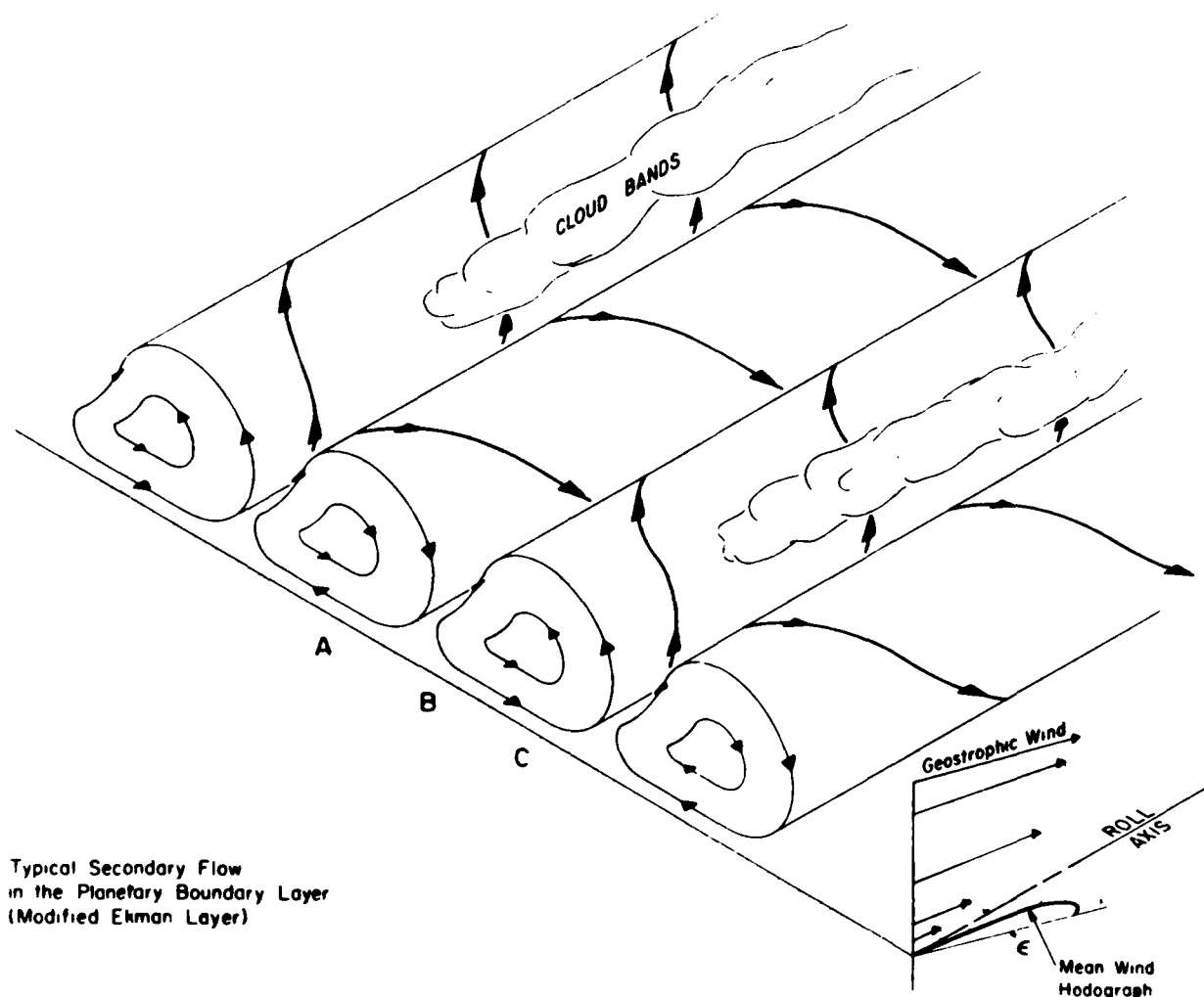
70

Fig. 12. Sketch of the coherent helical flow vortices contained in the boundary layer.
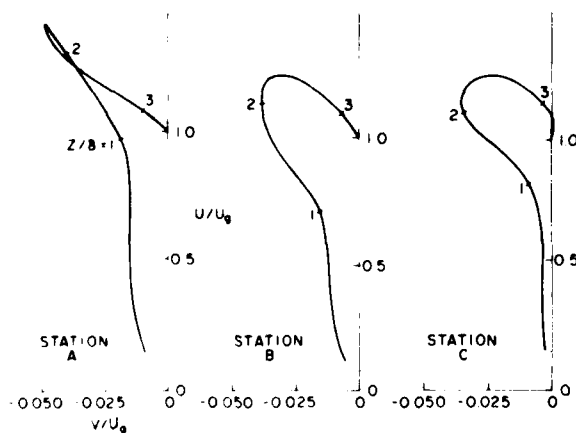

Fig. 13. Typical wind hodographs to be expected from radiosondes taken at stations A, B, or C in Figure 12. The freestream flow is U_g; the heights are with respect to the Ekman depth δ.

$$\frac{kG}{u^*} \ (\sin\alpha + \beta) = -B$$

$$\frac{kG}{u^*} \ (\cos\alpha + \gamma) = -A'$$

where $B = (1-\lambda)\psi$ and $A' = \ln\{-2ku^*/[fz_0(1-\psi)]\}$ $+ \psi-B$. β and γ are corrections that are non-zero whenever secondary flows or baroclinicity are important. ψ is the stratification correction to the surface layer (Paulson, 1970). In the general case with stratification the predicted drag law can be written, u^*/G (A, B, β, γ), where A, B, β, and γ are similarity functions. This relation is shown in Figure 15. These functions depend on stratification and the single similarity parameter, λ, which is approximately a constant, 0.15. Using this value and stratification information one can analytically calculate A, B, β, and γ. This was done by Brown
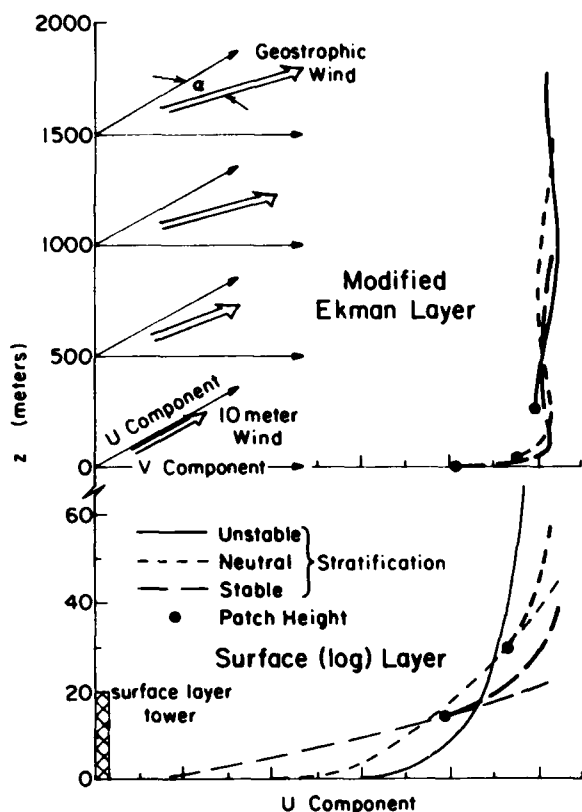
71

Fig. 14. Sketch of the velocity profile through the boundary layer for the two-layer model. Velocity profiles from the model are shown.

(1982) and the results agree with traditional curve fits to several data sets. The result is that the surface wind and stress vectors and (less accurately) heat flux are determined from the surface pressure gradients, which determine G for the neutral, barotrophic case. One needs the surface/air temperature difference for the important stratification effect on both layers. The horizontal air temperature gradient allows calculation of the thermal wind effect. The neutral roughness parameter and the single similarity parameter are known input values. The relative humidity adds a small buoyancy effect, which has been included. The model-predicted U_{10}/G and turning angle α are shown in Figure 16.

$$\frac{U^*}{G} = \frac{-|\beta B + \gamma A| + \sqrt{B^2 + A^2 - |A\beta - B\gamma|^2}}{B^2 + A^2}$$

where:

$$B = \frac{1}{2\lambda}[1 - \lambda\psi(HL)]$$

$$A = \ln(\lambda E) - \psi(HL) + B$$

$$\beta = [V_t - U_t + V_{2_z} - U_{2_z}]_0/2$$

$$\gamma = [V_t + U_t + V_{2_z} + U_{2_z}]_0/2$$

$$E = \delta/z_0$$

with:

$$HL = \frac{\lambda\delta}{L}$$

$$L = \frac{-Tu^{*2}}{kgT_*(T_A - T_s)}$$

$$u/u^* = (1/K)[\ln(z/z_0) - \psi(HL)]$$

$$\delta = \frac{2k\lambda u^*/f}{1 - \lambda\delta\psi_z(HL)}$$

Given: ψ from Businger/Dyer $= Fn(T_a - T_s)$
   U_{2_z} from Brown (1970, 1972) $\doteq |0.1, 0.1| \propto L$
   z_0 constant or $Fn(u^*)$
   $\lambda \doteq 0.15$
   (U_t, V_t) from $\nabla_H T$
   G from $\nabla_H P$

Fig. 15. Summary of the drag relation for the similarity formulation (from Brown 1982). Effects included are: ψ—surface layer stratification; (U_2, V_2)—secondary circulation; (U_t, V_t)—thermal wind; z_0—variable roughness.
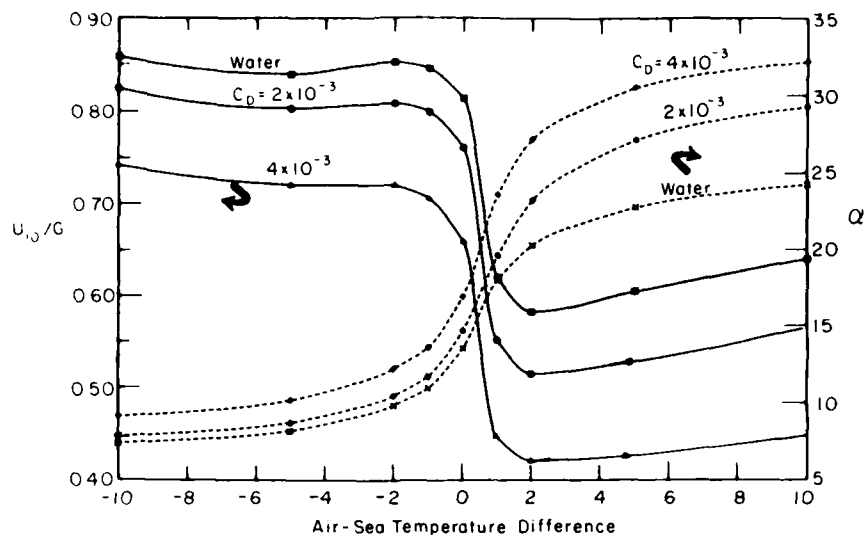
Fig. 16. Results of two-layer model for windspeed ratio, U_{10}/G, and angle of turning α for various neutral drag parameters (i.e. various roughnesses) vs. stratification.
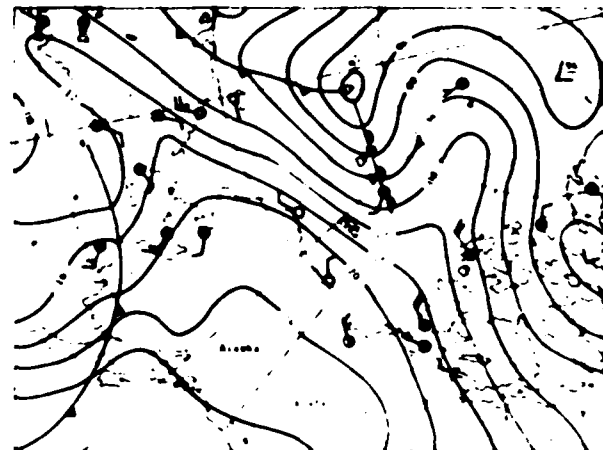
The MIZ

The basic driving force for the PBL flow and the fluxes is the freestream flow, the geostrophic or gradient wind G. This must be determined from the balance between Coriolis force and pressure gradient force. The first is determined by the latitude, but for the second we need a good pressure field. Data on surface pressure fields are routinely produced by the national weather services. However, particularly in the high latitudes, the data are often sparse and the pressure field is inaccurate. Figure 17 shows such a predicted field for AIDJEX compared to the pressure field determined by the pressure measurements at the manned stations and a ring of buoys at about 400 km diameter. While this clearly indicates that we have trouble getting adequate pressure input data, other correction factors are often minimal in the polar regions. Over the ice, roughness, stratification, and the thermal wind (horizontal temperature gradients)
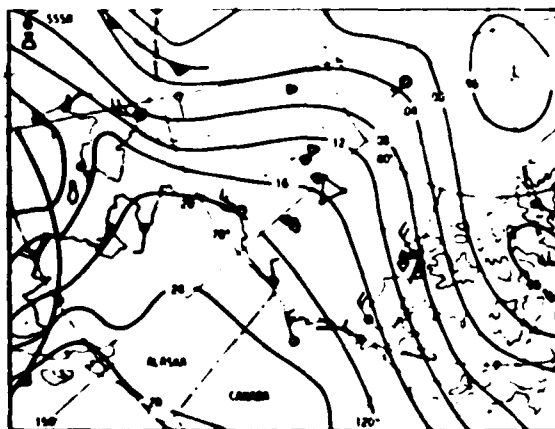
NWS

AIDJEX

Fig. 17. Comparison of NWS surface pressure map and AIDJEX pressure measurement augmented analysis by M. Albright.

73

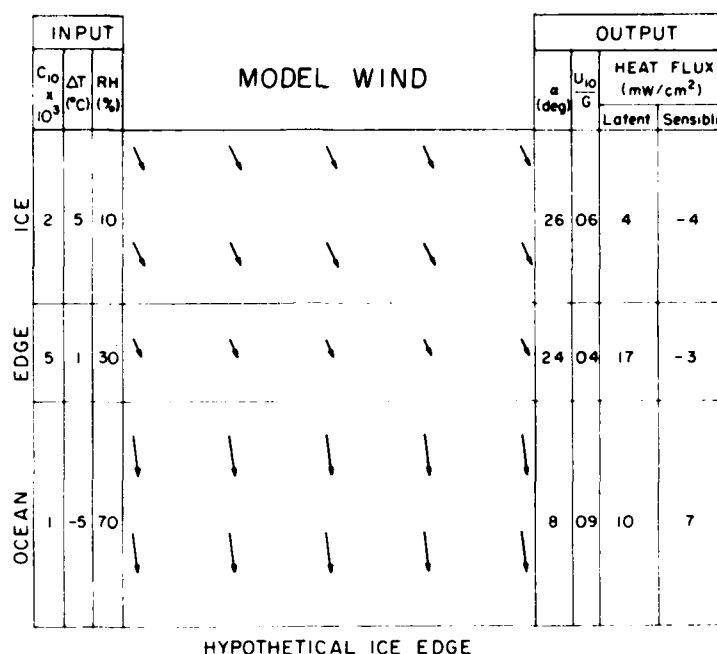|	INPUT			MODEL WIND	OUTPUT		HEAT FLUX (mW/cm²)	
	$C_{10} \times 10^3$	ΔT (°C)	RH (%)		α (deg)	$\dfrac{U_{10}}{G}$	Latent	Sensible
ICE	2	5	10		26	06	4	-4
EDGE	5	1	30		24	04	17	-3
OCEAN	1	-5	70		8	09	10	7

HYPOTHETICAL ICE EDGE

Fig. 18. The variation in the surface wind for a constant geostrophic wind field over the MIZ. The variation in drag parameter, air/sea/ice temperature difference, and relative humidity produces variation in angle of turning, speed, ratio, and fluxes.

are often fairly uniform. Thorndyke and Colony (1982) have shown excellent correlation between simple geostrophic flow from surface pressure fields and ice motion.

However, at the MIZ, both roughness and stratification change relatively abruptly. This means careful evaluation of the PBL flow field assumptions, such as flow equilibrium, is necessary. The MIZ produces excellent conditions for studies of PBL modification on the mesoscale. We have run our $N \times D$ equilibrium model for various conditions across an ice edge. The variable inputs are the surface roughness, directly related to the C_D for neutral stratification, the stratification represented in the air/surface temperature difference, and the surface relative humidity. The outputs are the angle of turning, the wind ratio, U_{10}/G, and the latent and sensible heat fluxes. Figure 18 shows representative values across an ice edge for off-ice winds. The turning and acceleration of the wind are evident. A large-scale windfield was calculated for the North Sea Experiment (NORSEX) period, shown in Figure 19. Here, only the change from moderately rough ice to moderately convec-

tive marine conditions is calculated on a 120-km grid. A hypothetical ice edge with a wavelength of about 200 km was inserted into a 10-m s⁻¹ uniform geostrophic flow field. The magnitude of the variation in the flow at the MIZ depends on the width of the MIZ and the rapidity of adjustment to the new surface conditions. However, it is instructive to look at the predicted divergence fields for this particular case (Figure 20). The imposed ice edge wavelength is evident. The interaction with the flow field, which is only slightly curved, produces indications of large divergence values in the MIZ vicinity.

Finally, to get down to the scale of the MIZ, I will speculate a bit on the effects of non-equilibrium. Figure 21 shows a cross section with transition zones as suggested by the Bering Sea MIZEX. The stratification and roughness changes from ocean to ice are as shown. The C_{D_n} corresponds to the z_0 roughness parameter. The model output for the equilibrium flow over the pack ice, the MIZ, and the ocean has been extrapolated across the edge zones by imposing a linear variation in C_D to show the expected variation in turning angle and
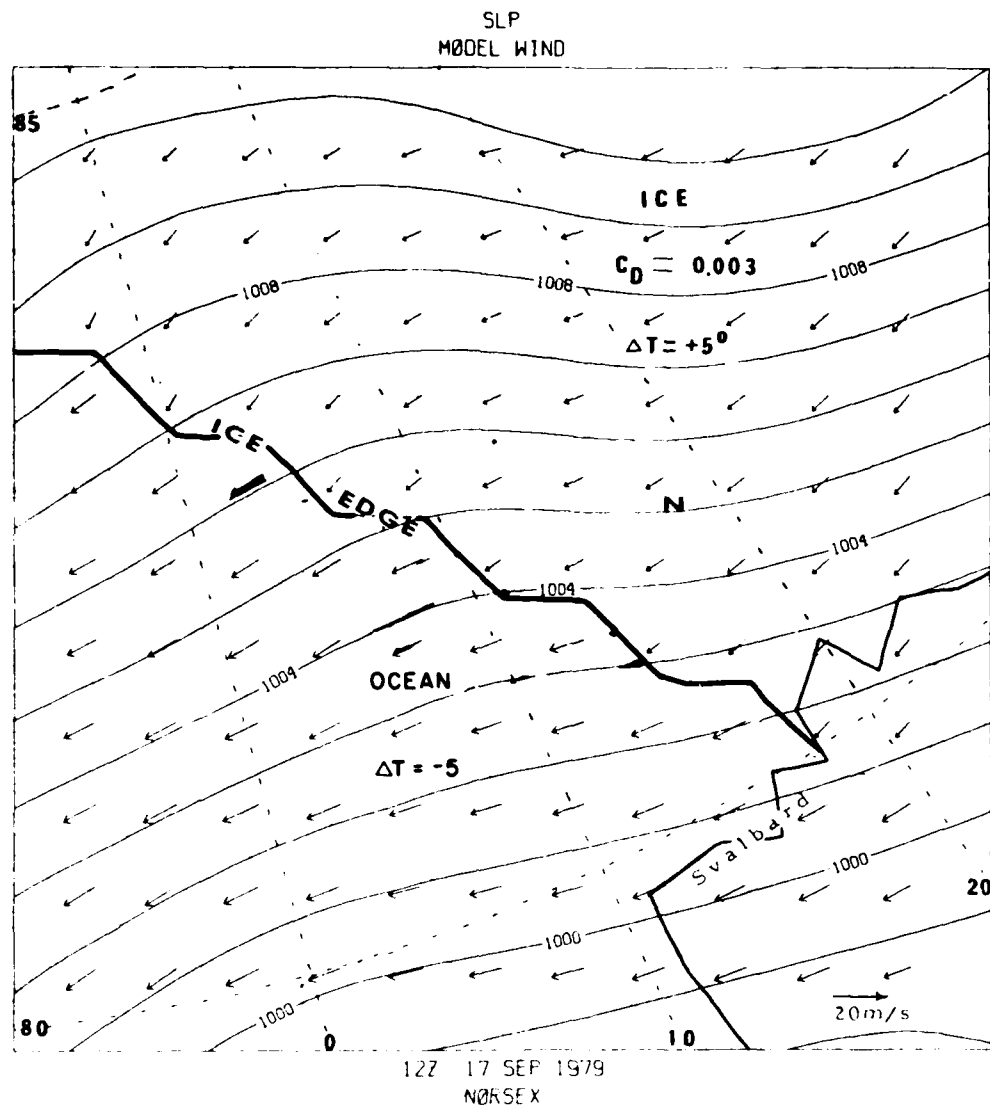
74

SLP
MODEL WIND

ICE

$C_D = 0.003$

$\Delta T = +5^{\circ}$

ICE EDGE

N

OCEAN

$\Delta T = -5$

Svalbard

1008   1008   1008
1004
1004
1000
1000
1000

85

80   0   10   20

20 m/s

12Z 17 SEP 1979
NORSEX

Fig. 19. The mesoscale wind field calculated during NORSEX. The ice edge has a representative wave variation.

U_{10}/G, depending on the direction of flow. The bottom graph shows the resulting effect on surface stress. For instance, on-ice flow has higher than equilibrium surface winds when it first hits the ice. This means that U_{10} is higher than is represented in the C_D where the wind was carefully in equilibrium for parameterizing measurements. This higher momentum will produce a compact edge. When the flow is off-ice, the gradual buildup to the rough ice may allow equilibrium values of surface winds with a ratio of $U_{10}/G = 0.64$ to develop.

Once the smoother, convective conditions over the water are encountered, the flow speeds increase towards the ratio $U_{10}/G = 0.75$. However, there is a region where the stress is lower, reflecting the lower-than-equilibrium windspeeds. The ramifications for ice band creation and movement will be left to the legions of band afficionados.

When the airflow is parallel to the ice edge, there will be differential drag and wind turning. The result is shear and convergence or divergence at the PBL along the MIZ.
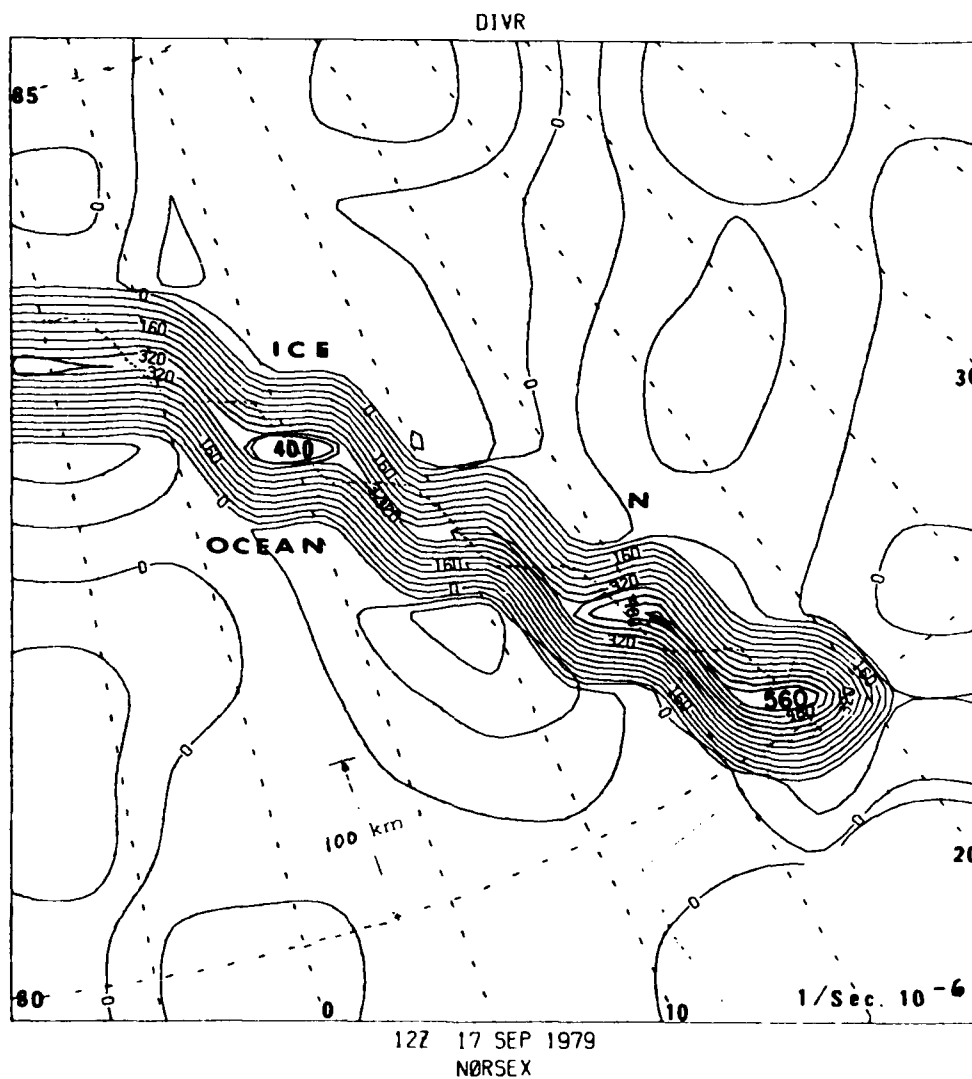
75

DIVR

Fig. 20. The divergence field from the model winds in Figure 19. The net effect of PBL
variations and the characteristic periodicity in the ice edge produce large divergences.
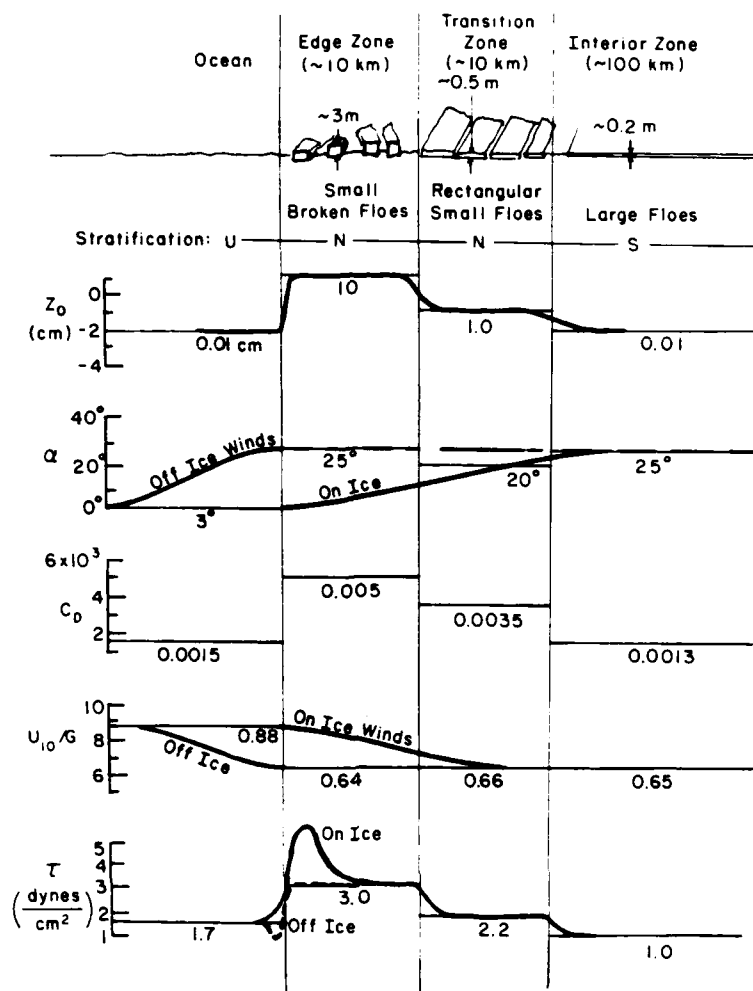
Fig. 21. A summary of the modified PBL flow across the ice edge. The model (equilibrium flow) results show constant values in each of the four zones (thin lines). The actual variations due to linearly represented inertial effects are shown in solid lines.

Conclusion

It is evident that the polar regions have certain advantages to the theoretical PBL modeller. The ability to model stress, and perhaps heat flux, on the mesoscale using similarity and geostrophic forcing has greatly increased. The drag coefficient is available to an accuracy sufficient to reflect changes in PBL stratification and ice or oceanic roughness. The conditions at the MIZ present a relatively sharp and uncomplicated transition region for the study of PBL adjustment times and processes.

There are suggestions that the divergence (or convergence for on-ice flow) is significant along the MIZ. There is probably an ice/sea breeze circulation component. This resulting wind stress can cause an oceanic circulation at the MIZ. For the along-ice flows, the surface winds are larger over the ocean than over the ice for the same geostrophic flow, yet the surface stress is larger over the ice. There are evidently several possible secondary circulations forced by this transition zone.

From a practical standpoint, to get an accurate evaluation of these variations, it will be essential

77

to get an accurate determination of the forcing flow. This will require good pressure measurements on as small a scale as instrument accuracy will allow. At 80° latitude, a 1-m s⁻¹ accuracy in G corresponds to 0.7 mb accuracy in instruments separated by 400 km. On the MIZ scale of 40 km, 0.07 mb accuracies are needed. The available NWS pressure maps probably yield no better than 2 or 3 mb accuracy on this scale and show no variation with wavelengths less than about 600 mb. They will have to be supplemented to provide mesoscale gradient wind information. Alternate prospects for accurate wind input data are aircraft survey flights in the PBL and/or satellite ocean scatterometer-determined winds together with buoy winds over the ice.

When the most recent drag coefficient data, which include variations due to stratification, humidity, and roughness, are used in conjunction with a similarly responsive PBL model for the wind, details of the MIZ stress and flux field can be calculated. The limiting factor to these relatively simple bulk formula methods for the mesoscale to synoptic fields is the accuracy of the input wind fields.

REFERENCES

Andreas, E.L., W.B. Tucker III, and S.F. Ackley, Atmospheric boundary-layer modification, drag coefficient, and surface heat flux in the antarctic marginal ice zone, *J. Geophys. Res., 89*, 649–661, 1984.

Banke, E.G., S.D. Smith, and R.J. Anderson, Recent measurements of wind stress on Arctic sea ice, *J. Fish. Res. Board Can., 33*, 2307–2317, 1976.

Brown, R.A., A simple momentum integral model, *J. Geophys. Res., 79*, 4076–4079, 1974.

Brown, R.A., Modeling the geostrophic drag coefficient for AIDJEX, *J. Geophys. Res., 86*, 1989–1994, 1981.

Brown, R.A., On two-layer models and the similarity functions for the PBL, *Bound.-Layer Met., 24*, 451–463, 1982.

Brown, R.A. and W.T. Liu, An operational large-scale marine planetary boundary layer model, *J. Appl. Met., 21*, 261–269, 1982.

Carsey, F.D., The boundary layer height in air stress measurements, In: *Sea Ice Processes and Models*, edited by R.S. Pritchard, University of Washington Press, Seattle, Washington, 443–451, 1980.

Katz, D.I., Air stress measurements from an aircraft, In: *Sea Ice Processes and Models*, edited by R.S. Pritchard, University of Washington Press, Seattle, Washington, 452–463, 1980.

Macklin, S.A., Wind drag coefficient over first-year sea ice in the Bering Sea, *J. Geophys. Res., 88*, 2845–2852, 1983.

Meyer, R.E. (Editor), *Transition and Turbulence*, Academic Press, New York, 1981.

Paulson, C.A., The mathematical representation of wind speed and temperature profiles in the unstable atmospheric surface layer, *J. Appl. Met., 9*, 857–861, 1970.

Pease, C.H. and J.E. Overland, An atmospherically driven sea-ice drift model for the Bering Sea, *Annals of Glaciology, 5*, 111–114, 1984.

Thorndike, A.S. and R. Colony, Sea ice motion in response to geostrophic winds, *J. Geophys. Res., 87*, 5845–5852, 1982.

Walter, B.A., J.E. Overland, and R.O. Gilmer, Air-ice drag coefficients for first-year sea ice derived from aircraft measurements, *J. Geophys. Res., 89*, 3550–3560, 1984.

An Air-Ice-Ocean Coupled Model for the Formation of Leads or Polynyas

P.C. CHU

Department of Geophysical Sciences
The University of Chicago, Chicago, Illinois 60637, U.S.A.

SUMMARY

A seabreeze mechanism which may contribute to the formation of leads or polynyas in the marginal ice zone is investigated using a steady-state coupled air-ice-ocean model. The model contains three parts: a thermally forced boundary layer air flow, a mechanically forced ice drift, and a reduced gravity ocean model. The three components are linked through the surface temperature gradient and various stresses, i.e. air stress (on ice), ice stress (on water), and water stress (on ice).

In the marginal ice zone, a thermally generated surface wind blowing from ice to water ("icebreeze") with some deflection due to the earth's rotation is generally divergent. Such divergent local wind fields can make the ice flow either divergent or convergent, depending on the properties of the ice and water beneath them. For thin ice and a thick surface water layer, the turning angle (the angle between the directions of the surface wind and ice flow) is small and the ice flow is divergent. In contrast, for thick ice and a thin surface water layer, the turning angle is large and the ice flow is convergent. The air-ice-ocean model confirms this result and gives criteria for the formation of leads or polynyas.

INTRODUCTION

In this study, a steady-state coupled air-ice-ocean model is employed to investigate the conditions for ice divergence in the marginal ice zone (MIZ) which may break the ice and cause the formation of leads or polynyas. Although upwelling of warm, deep water and convective processes probably produce polynyas by supplying heat from the ocean, another mesoscale seabreeze mechanism which causes ice-breaking may exist.

A possible mechanism for the mesoscale air-ice-ocean interaction in the MIZ is depicted in Figure 1. The low-level air flow generated by a surface temperature gradient moves from ice to water ("icebreeze"), with some deflection to the right (or left) in the north (or south) polar region. This icebreeze should have a maximum speed near the ice edge and decrease both iceward and waterward, i.e. it is divergent over the ice and convergent over the water. The ice flow driven by the surface wind field is to the right (or left) of the wind in the north (or south) polar region. The turning angle, defined as the angle between the directions of ice flow and surface air flow, varies from 0° to
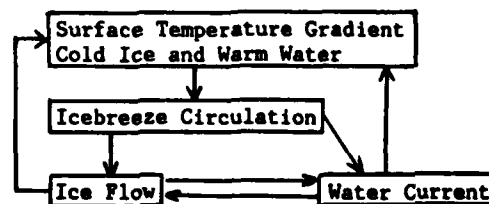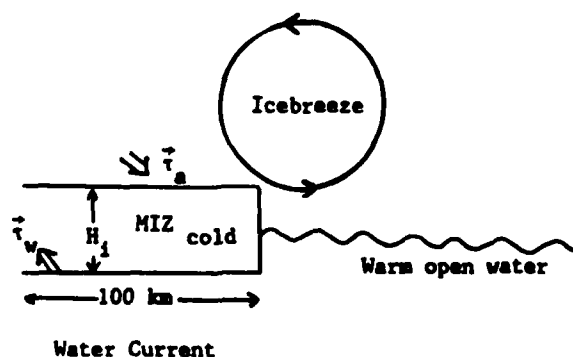

Fig. 1. Ice-air-ocean coupled system.

79

90°, depending on the properties of the ice and water.

The steady-state air-ice-ocean interaction model depicted in subsequent sections is used to determine the main criteria for ice divergence/convergence, and therefore for lead or polynya formation.

THERMALLY FORCED BOUNDARY LAYER AIR FLOW

We utilize the same planetary boundary layer model treated by Kuo (1973) and Chu (1985, 1986) to simulate a thermally forced boundary layer air flow. The coordinate system is chosen such that the x-axis is in the cross-ice-edge direction and the y-axis parallels the ice edge, as shown in Figure 2. The x-coordinate's unit length is twice the MIZ width L (i.e. 200 km), and that of the vertical coordinate is $\delta = (v/\Omega)^{0.5}$, where v is the vertical eddy viscosity and Ω the angular velocity of the earth's rotation. The line $x = \frac{1}{2}$ is located at the ice edge. The MIZ covers the zone $(0 < x < 0.5, y)$ where the y-axis $(x = 0)$ is near the boundary between the MIZ and the interior ice pack. It is considered that spatial variations in the MIZ are much larger perpendicular to the ice edge than parallel to it, and hence derivatives with respect to y are assumed to be zero (Lepparanta and Hibler, 1986).

The potential temperature of air is divided into two parts: a basic state $\theta_{B*}(z)$ and a perturbation θ_*'. The basic state is given by

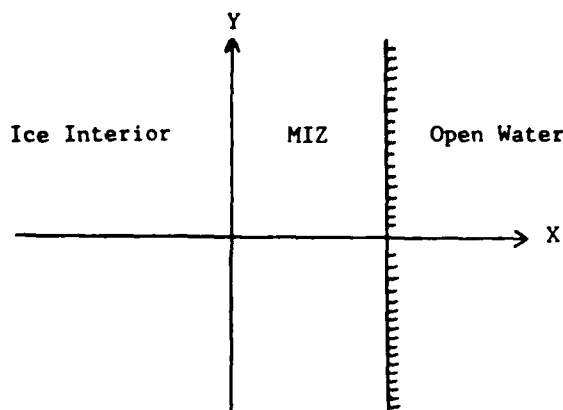$$\theta_{B*}(z) = \theta_{B0} + (N^2\theta_{B0}\delta)z \qquad (1)$$

where θ_{B0} is the basic air potential temperature at the surface and N is the Brunt-Vaisala frequency of the atmosphere.

The mathematical manipulation is almost the same as in the second section of Chu (1986), except that the steady surface temperature gradient is used here:

$$\theta_*'(x,0) = -DT_0\cos\pi x \qquad (2)$$

where $2DT_0$ is the mean surface temperature difference across the MIZ. The coordinates and atmospheric variables are nondimensionalized by setting

$$
\left.
\begin{aligned}
(x_*,z_*) &= (xL, z\delta) \\[4pt]
s' &\equiv \theta_*'/\theta_{B0} = (DT_0/\theta_{B0})s \\[4pt]
[u_*^{(a)}, v_*^{(a)}, w_*^{(a)}] &= U[u^{(a)}, v^{(a)}, w^{(a)}\delta/L] \\[4pt]
P_*^{(a)} &= (g\delta DT_0/\theta_{B0})p^{(a)}
\end{aligned}
\right\} \quad (3)
$$

where

$$U \equiv g\delta DT_0/(2L\Omega\theta_{B0}) \qquad (4)$$

is the scale of the icebreeze.

The surface wind driven by the horizontal temperature gradient is computed by

$$u^{(a)}(x) = \bar{u}^{(a)}\sin\pi x \qquad (5)$$

$$v^{(a)}(x) \; ^s \; \bar{v}^{(a)}\sin\pi x \qquad (6)$$

where

$$
\left.
\begin{aligned}
\bar{u}^{(a)} &\equiv U\sum_{j=1}^{3}a_j\lambda_j \\[8pt]
\bar{v}^{(a)} &\equiv U[b - f_0\sum_{j=1}^{3}a_j\lambda_j F(\lambda_j, r)] \\[8pt]
f_0 &= \sin\phi \\[4pt]
r &\equiv \pi^2\delta^2 v_h/(2L^2 v) \\[4pt]
F(\lambda, r) &\equiv 1/(\lambda^2/2 - r)
\end{aligned}
\right\} \quad (7)
$$

and ϕ is the latitude and v_h the horizontal eddy viscosity. Eigenvalues λ_j $(j = 1,2,3)$ are the roots

Y

Ice Interior | MIZ | Open Water

→ X

Fig. 2. The model MIZ and the coordinate system.

with negative real parts of the following sextic equation:

$$\lambda^6 - 4r\lambda^4 + 4(f_0^2 + r^2)\lambda^2 - 4\pi^2 R_i = 0 \qquad (8)$$

where the Richardson number R_i is defined by

$$R_i \equiv \delta^2 N^2 / (4L^2\Omega^2). \qquad (9)$$

The coefficients a_1, a_2, a_3 and b in eq 5 and 6 are determined by (Chu, 1986)

$$\sum_{j=1}^{3} a_j = 0$$

$$\sum_{j=1}^{3} \lambda_j (1 - K\lambda_j) a_j = 0$$

$$\qquad (10)$$

$$-f_0 \sum_{j=1}^{3} \lambda_j (1 - K\lambda_j) F(\lambda_j, r) a_j + b(1 + K\sqrt{2r}) = 0$$

$$\pi R_i \sum_{j=1}^{3} F(\lambda_j, r) a_j + \sqrt{2r} f_0 b / \pi = -1$$

where K is a measure of the effective depth of the constant stress sublayer (Kuo, 1973):

$$K = v / (C_a \delta) \qquad (11)$$

where C_a is a dimensional (m s^{-1}) air drag coefficient.

FREE ICE DRIFT MODEL

The linearized steady-state momentum equations for a free drift ice model are

$$f v^{(i)} + [\tau_x^{(a,i)} + \tau_x^{(w,i)}] / (\varrho_i H_i) = 0 \qquad (12)$$

$$-f u^{(i)} + [\tau_y^{(a,i)} + \tau_y^{(w,i)}] / (\varrho_i H_i) = 0 \qquad (13)$$

where $f = (= 2\Omega \sin\phi)$ is the Coriolis parameter, H_i the mean ice thickness, ϱ_i the ice density, $\vec{V}^{(i)} = [u^{(i)}, v^{(i)}]$ the ice velocity, $\vec{\tau}^{(a,i)} = [\tau_x^{(a,i)}, \tau_y^{(a,i)}]$ the wind stress on the ice, and $\vec{\tau}^{(w,i)} = [\tau_x^{(w,i)}, \tau_y^{(w,i)}]$ the water stress on the ice. The air and water stresses on ice are

$$\vec{\tau}^{(a,i)} = \varrho_a C_a \vec{V}^{(a)}$$

$$\qquad (14)$$

$$\vec{\tau}^{(w,i)} = \varrho_w C_w [\vec{V}^{(w)} - \vec{V}^{(i)}]$$

where $\vec{V}^{(a)} = [u^{(a)}, v^{(a)}]$ is the surface air velocity, $\vec{V}^{(w)} = [u^{(w)}, v^{(w)}]$ the water velocity and C_w the dimensional (m s^{-1}) water drag coefficient.

REDUCED GRAVITY OCEAN MODEL WITH RAYLEIGH DISSIPATION

The ocean model is a two-level model in which the lower layer is assumed to be deep enough that motion within it is vanishingly small. Such a model is referred to as a reduced gravity model. The momentum equations are

$$R u^{(w)} - f v^{(w)} - g H_w \Delta \varrho_w / (\varrho_w R) \partial^2 u^{(w)} / \partial x_*^2$$

$$= \tau_x^{(i,w)} / (\varrho_w H_w) \qquad (15)$$

$$R v^{(w)} + f u^{(w)} = \tau_y^{(i,w)} / (\varrho_w H_w) \qquad (16)$$

where R is the coefficient of Rayleigh friction, H_w the mean thickness of the surface water layer, ϱ_w the density of the surface water, $\Delta \varrho_w$ the density difference between the two layers, and $\vec{\tau}^{(i,w)} = [\tau_x^{(i,w)}, \tau_y^{(i,w)}]$ the ice stress on the water. $\vec{\tau}^{(i,w)}$ has the same magnitude but the opposite direction as $\vec{\tau}^{(w,i)}$, i.e.

$$\vec{\tau}^{(i,w)} = -\vec{\tau}^{(w,i)} = -\varrho_w C_w [\vec{V}^{(w)} - \vec{V}^{(i)}]. \qquad (17)$$

ICE DIVERGENCE/CONVERGENCE CRITERIA

The surface wind is the forcing term of the ice–ocean system. Since our model is linear, the mechanically forced ice and water motion $\vec{V}^{(i)}$ and $\vec{V}^{(w)}$ should have the same Fourier component as the forcing term $\vec{V}^{(a)}$, i.e.

$$u^{(i)}(x) = \bar{u}^{(i)} \sin\pi x, \qquad v^{(i)}(x) = \bar{v}^{(i)} \sin\pi x \qquad (18)$$

$$u^{(w)}(x) = \bar{u}^{(w)} \sin\pi x, \qquad v^{(w)}(x) = \bar{v}^{(w)} \sin\pi x \qquad (19)$$

where x is a nondimensional coordinate.

Substituting eq 5, 6, 14, 17, 18 and 19 into eq 12, 13, 15 and 16 we have the following four linear algebraic equations for the Fourier coefficients $u^{(w)}$, $v^{(w)}$, $u^{(i)}$ and $v^{(i)}$:

81

$$[R + \pi^2 gH_w \Delta\varrho_w/(\varrho_w RL^2) + \omega_3]\bar{u}^{(w)}$$

$$-f\bar{v}^{(w)} - \omega_3\bar{u}^{(i)} = 0 \tag{20}$$

$$f\bar{u}^{(w)} + (R + \omega_3)\bar{v}^{(w)} - \omega_3\bar{v}^{(i)} = 0 \tag{21}$$

$$-\omega_2\bar{u}^{(w)} + \omega_2\bar{u}^{(i)} - f\bar{v}^{(i)} = \omega_1\bar{u}^{(a)} \tag{22}$$

$$-\omega_2\bar{v}^{(w)} + f\bar{u}^{(i)} + \omega_2\bar{u}^{(i)} = \omega_1\bar{v}^{(a)} \tag{23}$$

where the parameters ω_1, ω_2 and ω_3 are defined by

$$\omega_1 \equiv \varrho_a C_a/(\varrho_i H_i)$$

$$\omega_2 \equiv \varrho_w C_w/(\varrho_i H_i) \tag{24}$$

$$\omega_3 \equiv C_w/H_w.$$

Solving the nonhomogeneous linear algebraic equations 20–23 we obtain the amplitudes of the ice and water flow fields:

$$\bar{u}^{(i)} = \omega_1[\omega_2(1-\alpha_2)\bar{u}^{(a)} + f(1 + \alpha_3\omega_2)\bar{v}^{(a)}]/$$

$$[\omega_2^2(1-\alpha_1)(1-\alpha_2) + f(1 + \alpha_3\omega_2)^2] \tag{25}$$

$$\bar{v}^{(i)} = \omega_1[\omega_2(1-\alpha_1)\bar{v}^{(a)} - f(1 + \alpha_3\omega_2)\bar{u}^{(a)}]/$$

$$[\omega_2^2(1-\alpha_1)(1-\alpha_2) + f(1 + \alpha_3\omega_2)^2] \tag{26}$$

$$\bar{u}^{(w)} = \omega_3[\bar{u}^{(i)}(R + \omega_3) + f\bar{v}^{(i)}]/$$

$$[\alpha_0(R + \omega_3) + f^2] \tag{27}$$

$$\bar{v}^{(w)} = \omega_3[\alpha_0\bar{v}^{(i)} - f\bar{u}^{(i)}]/[\alpha_0(R + \omega_3) + f^2] \tag{28}$$

where

$$\left.\begin{array}{l} \alpha_0 \equiv R + \omega_3 + \pi^2 gH_w\Delta\varrho_w/(\varrho_w RL^2) \\[6pt] \alpha_1 \equiv \omega_3(R + \omega_3)/[\alpha_0(R + \omega_3) + f^2] \\[6pt] \alpha_2 \equiv \omega_3\alpha_0/[\alpha_0(R + \omega_3) + f^2] \\[6pt] \alpha_3 \equiv \omega_3/[\alpha_0(R + \omega_3) + f^2]. \end{array}\right\} \tag{29}$$

Since our model is y-independent, the ice divergence/convergence criteria are simply

$$\bar{u}^{(i)} \begin{array}{l} > \\ = 0 \\ < \end{array} \begin{array}{l} \text{Ice divergence} \\ \text{No ice divergence/convergence} \\ \text{Ice convergence} \end{array} \tag{30}$$

Using eq 25, the criteria (eq 30) are rewritten as

$$C_r = |\bar{v}^{(a)}/\bar{u}^{(a)}| \begin{array}{l} > \\ \\ < \end{array} \begin{array}{l} \text{Ice divergence} \\ \text{No ice divergence/convergence} \\ \text{Ice convergence} \end{array} \tag{31}$$

where

$$C_r \equiv \omega_2(1-\alpha_2)/[|f|(1 + \alpha_3\omega_2)]$$

and $\beta = \tan^{-1}|\bar{v}^{(a)}/\bar{u}^{(a)}|$ is the icebreeze deflection angle due to the earth's rotation. In the present calculation we fixed all values of the parameters except for (1) the Brunt–Vaisala frequency of the atmosphere N, (2) the mean ice thickness H_i, and (3) the mean depth of the water surface layer H_w. Table 1 lists the values of the fixed parameters. Figure 3 describes the dependence of $|\bar{v}^{(a)}/\bar{u}^{(a)}|$ on R_i at three different latitudes (65°, 70° and 75°). $|\bar{v}^{(a)}/\bar{u}^{(a)}|$ increases with increasing latitude and decreases with increasing R_i. At 65° (N and S) latitude it varies from 0.9 ($\beta = 48°$) when $R_i = 0.10\times10^{-2}$ to 0.53 ($\beta = 27.5°$) when $R_i = 4.03\times10^{-2}$.

We also computed the parameter C_r as a function of H_i and H_w at three different latitudes (65°, 70° and 75°), where H_i varies from 0 to 10 m and H_w from 0 to 50 m. The distribution of C_r with H_i and H_w is shown in Figure 4. High values of C_r are located in the region of large H_w and small H_i. The smaller the H_i (or the larger the H_w), the larger the C_r. It is quite understandable that the water current $\vec{V}^{(w)}$ is very weak as H_w becomes large, because the mechanical forcing terms in eq 20 and 21, $\omega_3 u^{(i)}$ and $\omega_3 v^{(i)}$, become small. When the water current $\vec{V}^{(w)}$ is weak (refer to large H_w) the turning angle largely depends on the ice thickness. For

Table 1. The standard model parameters.

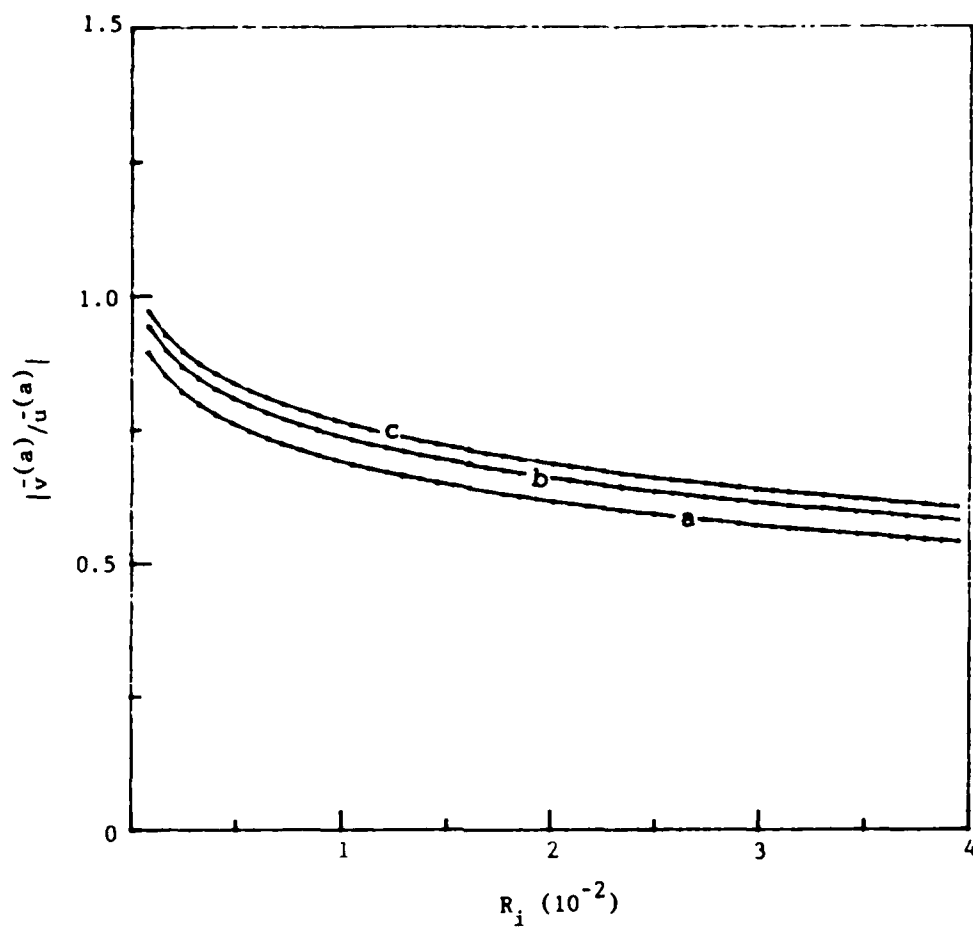| L	=	200 km	v	=	5 m^2 s^{-1}	v_h	=	10^5 m^2 s^{-1}
Ω	=	0.7292×10^{-4} s^{-1}	g	=	9.81 m s^{-2}	R	=	2.08×10^{-5} s^{-1}
θ_{B0}	=	270 K	C_w	=	1.76×10^{-3} m s^{-1}	C_a	=	3×10^{-2} m s^{-1}
ϱ_a	=	1.29 kg m^{-3}	ϱ_w	=	10^3 kg m^{-3}	ϱ_i	=	910 kg m^{-3}
$\Delta\varrho_w$	=	0.5 kg m^{-3}	DT_0	=	5 K	ϕ	=	(65°, 70°, 75°)

82

Fig. 3. Dependence of $\bar{v}^{(a)}/\bar{u}^{(a)}$ on the atmospheric Richardson number R_i for three different latitudes: (a) 65°, (b) 70°, and (c) 75°.
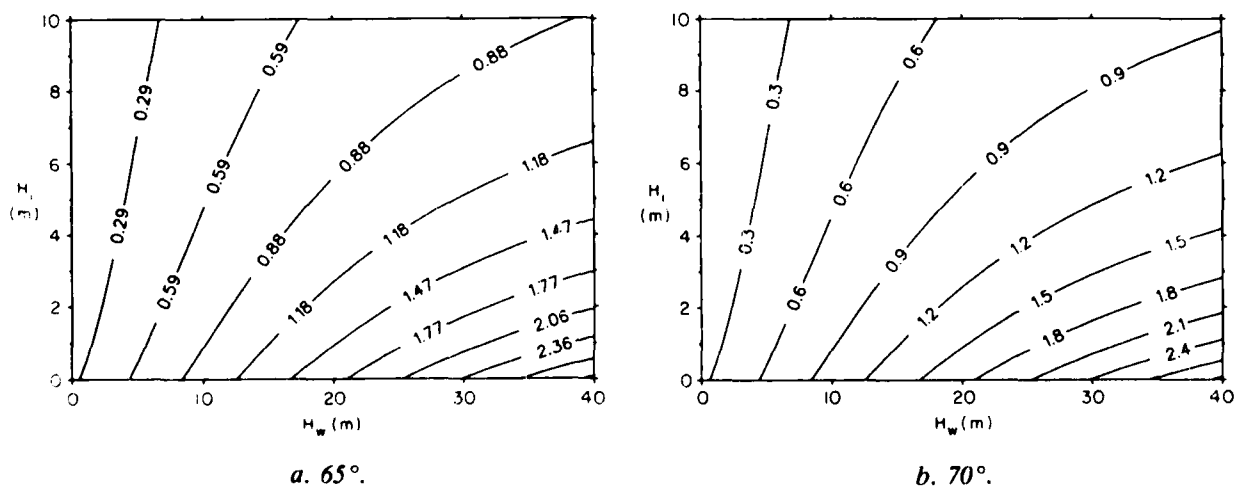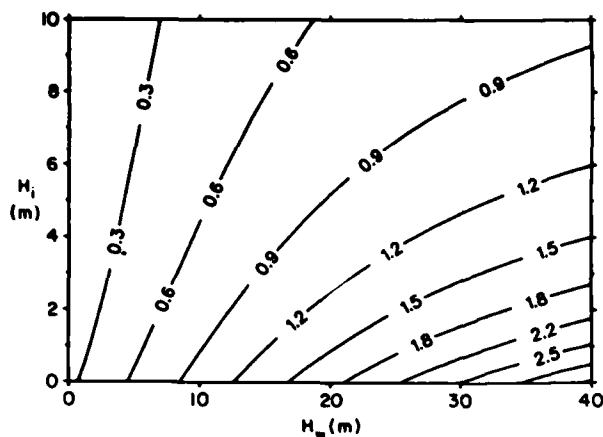

a. 65°.

b. 70°.

Fig. 4. Isolines of C_r in the (H_i, H_w) plane for three different latitudes.

83

c. 75°.

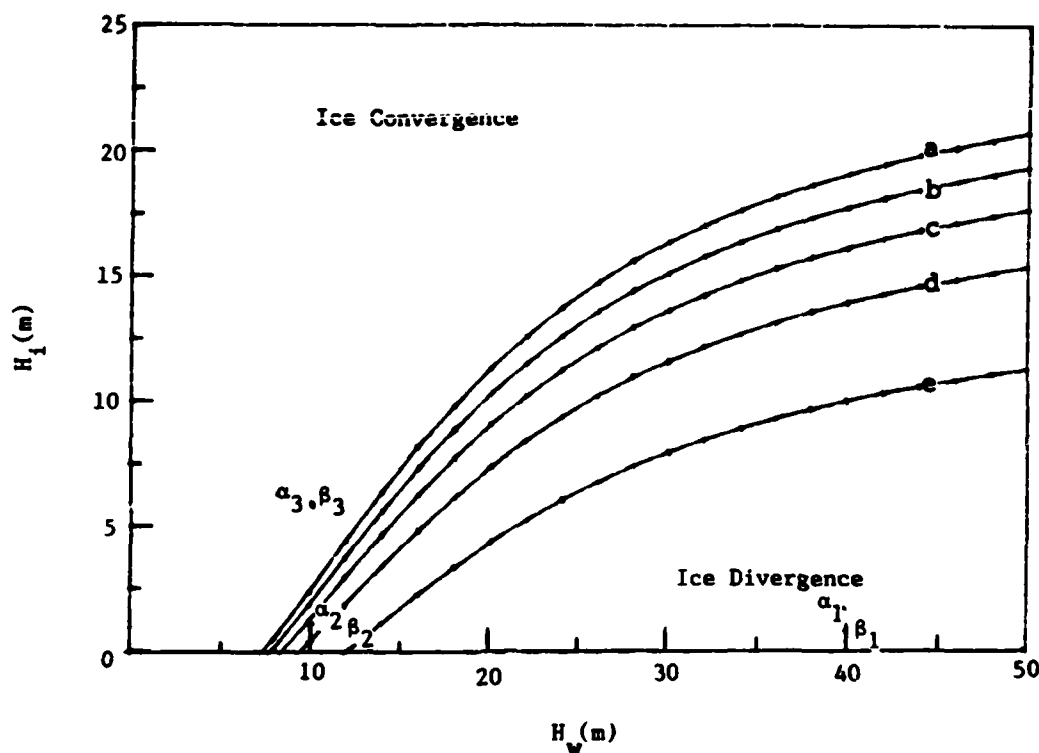*Fig. 4 (cont'd). Isolines of C_r in the (H_i, H_w) plane for three different latitudes.*

Fig. 5. H_i-H_w curves for zero ice divergence/convergence for five different values of the atmospheric Richardson number: (a) $R_i = 4 \times 10^{-3}$, (b) $R_i = 3 \times 10^{-3}$, (c) $R_i = 2 \times 10^{-3}$, (d) $R_i = 10^{-3}$ and (e) $R_i = 10^{-3}$.

thin ice, eq 22 and 23 show that $\vec{V}^{(i)}$ deflects by a small angle from $\vec{V}^{(a)}$; therefore the ice flow is divergent.

Solving the algebraic equation 25 for H_i after setting $u^{(l)} = 0$, we get the dependence of H_i on H_w for the no divergence or convergence case, as shown in Figure 5. These curves separate the parameter plane (H_i, H_w) into ice convergence and ice divergence parts. Figures 3-5 help us to justify the ice divergence/convergence in the MIZ, and to predict the formation of a lead or polynya.

AIR, ICE AND WATER FLOW FIELDS

We compute $\vec{V}^{(a)}$, $\vec{V}^{(i)}$ and $\vec{V}^{(w)}$ for the north and south polar regions. The atmospheric Brunt-Vaisala frequency N is taken as 10^{-2} s^{-1} (corresponding to a Richardson number R_i of 0.81×10^{-2}). The parameters H_w and H_i, which can be indicated as points in the H_i, H_w plane (Figure 5), are chosen to represent three cases: (1) thin ice-thick surface water layer (α_1 and β_1), (2) thin ice-thin surface water layer (α_2 and β_2), and (3) thick ice-thin sur-

84

face water layer (α_1 and β_1). The points α_1 (40 m, 1.5 m), α_2 (10 m, 1.5 m) and α_3 (10 m, 6 m) are for the north polar region, and points β_1 (40 m, 0.7 m), β_2 (10 m, 0.7 m) and β_3 (10 m, 6 m) are for the south polar region. In Figure 5, points α_1 and β_1 are located in the ice divergence area, α_2 and β_2 in the no divergence or convergence area, and α_3 and β_3 in the ice convergence area.

Figures 6 and 7 show $\vec{V}^{(a)}$, $\vec{V}^{(i)}$ and $\vec{V}^{(w)}$ in the north and south polar regions (65°), respectively.

They indicate the following results:

(1) The surface wind field does not change with H_w and H_i. When the temperature difference across the MIZ is 10°C (i.e. $DT_0 = 5$°C), $N = 10^{-2}$ s^{-1} and $\phi = 65$°, the maximum surface wind speed can reach 17 m s^{-1}.

(2) The surface wind field varies from north to south polar regions. In the north (south) polar region, the surface wind blows from the ice to the water with a deflection to the right (left).
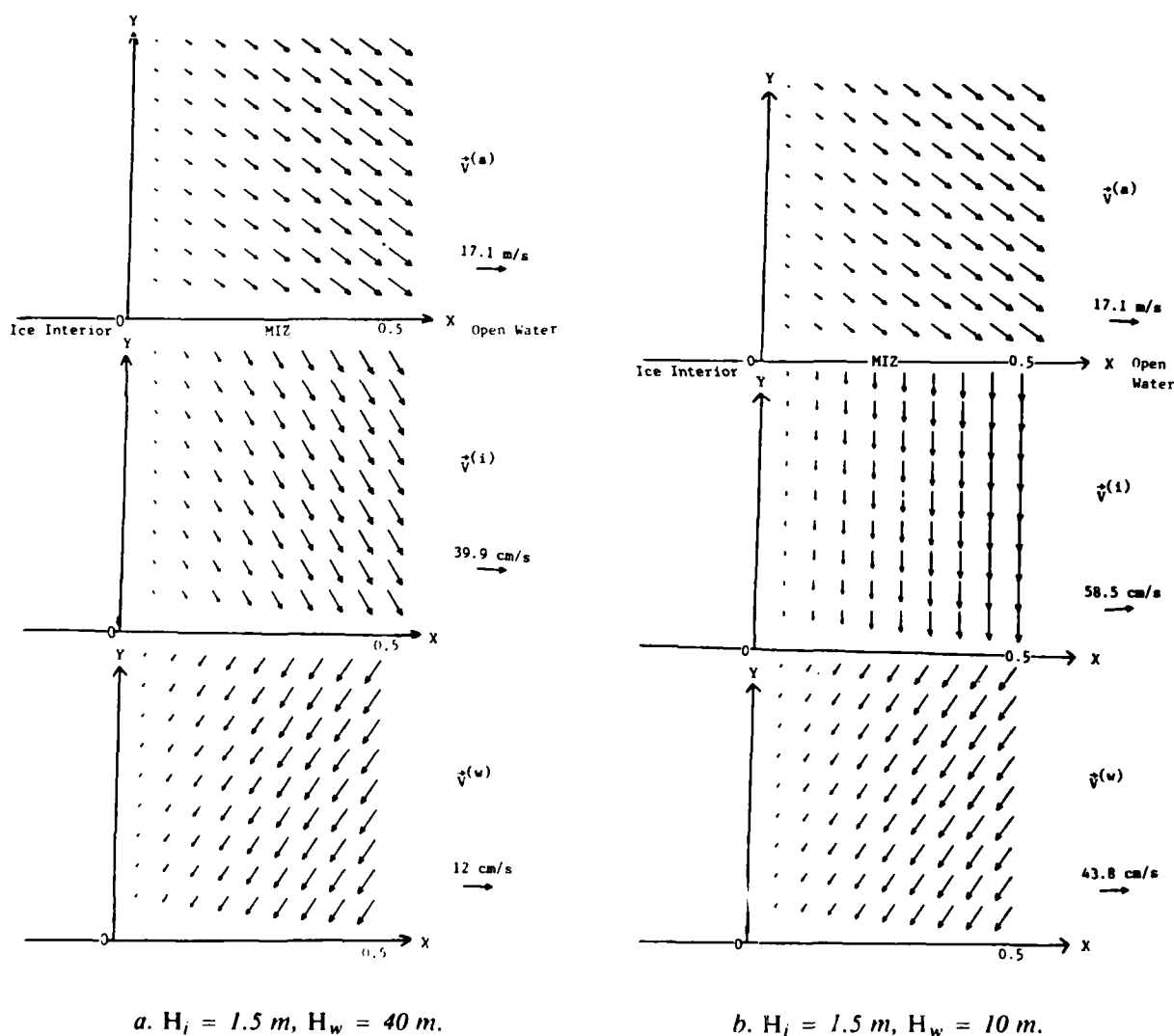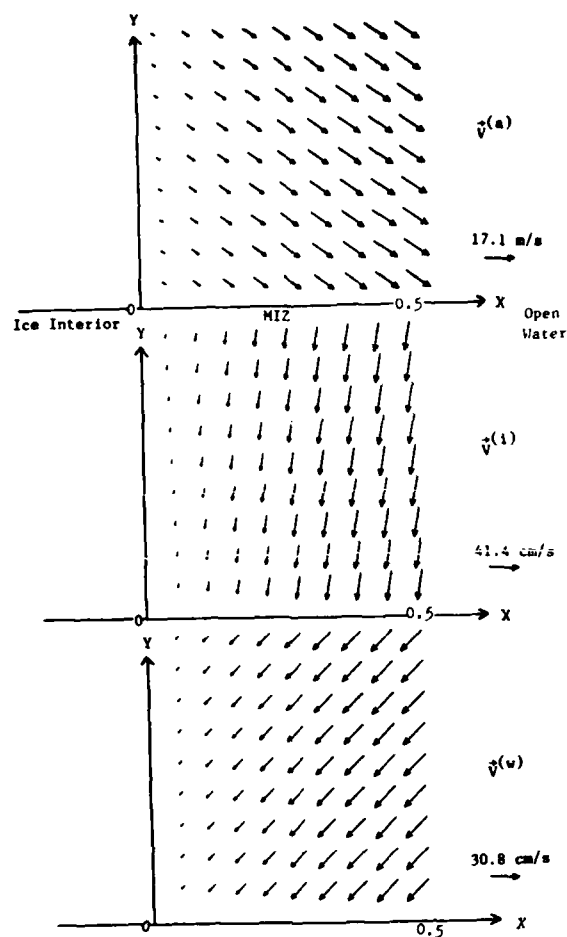

a. H$_i$ = 1.5 m, H$_w$ = 40 m.

b. H$_i$ = 1.5 m, H$_w$ = 10 m.

Fig. 6. $\vec{V}^{(a)}$, $\vec{V}^{(i)}$ and $\vec{V}^{(w)}$ in the north polar region (ϕ = 65°N, N = 10^{-2} s^{-1}).
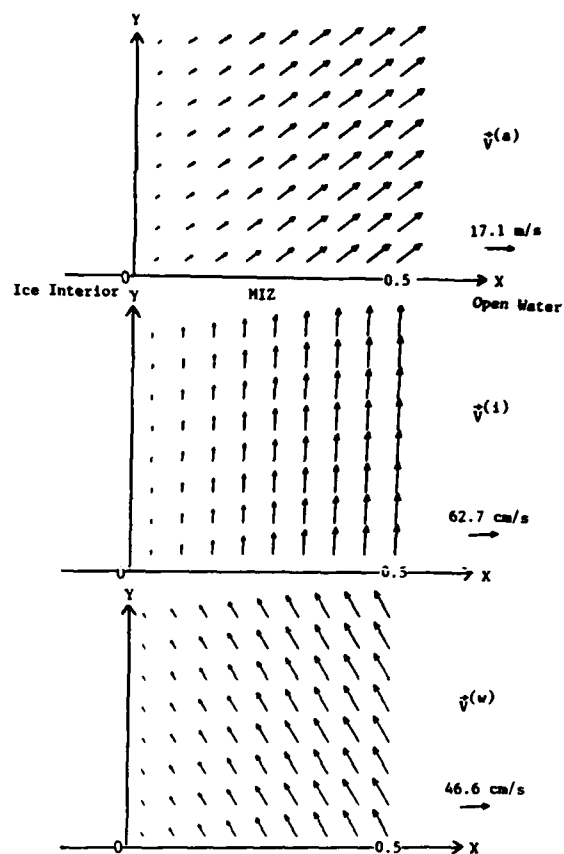
c. $H_i = 6\,m$, $H_w = 10\,m$.

Fig. 6 (cont'd). $\vec{V}^{(a)}$, $\vec{V}^{(i)}$ and $\vec{V}^{(w)}$ in the north polar region ($\phi = 65°N$, $N = 10^{-2}\,s^{-1}$).

(3) The ice flow varies with H_w and H_i. For a thin ice-thick surface water layer (points α_1 and β_1 in Figure 5), the ice flow reveals evident divergence, as shown in Figures 6a and 7a. The maximum ice flow velocity is at the ice edge. It reaches 40 cm s^{-1} (40.7 cm s^{-1}) for $H_i = 1.5$ m, $H_w = 40$ m, and $\phi = 65°N$ ($H_i = 0.7$ m, $H_w = 40$ m, $\phi = 65°S$). Such steady-state ice divergence will break the ice and cause the formation of a lead or polynya. For the thick ice-thin surface water layer case (points α_3 and β_3 in Figure 5), the ice flow exhibits obvious convergence (Figures 6c and 7c). The maximum ice flow velocity is also at the ice edge. It reaches 41.4 cm s^{-1} for $H_i = 6$ m, $H_w = 10$ m, and $\phi = 65°N$ (65°S). Such steady-state ice convergence will prevent the ice from breaking. For the thin ice-thin surface water layer case (points α_2 and β_2 in Figure 5), the ice flow displays no divergence/convergence (Figures 6b and 7b).

86
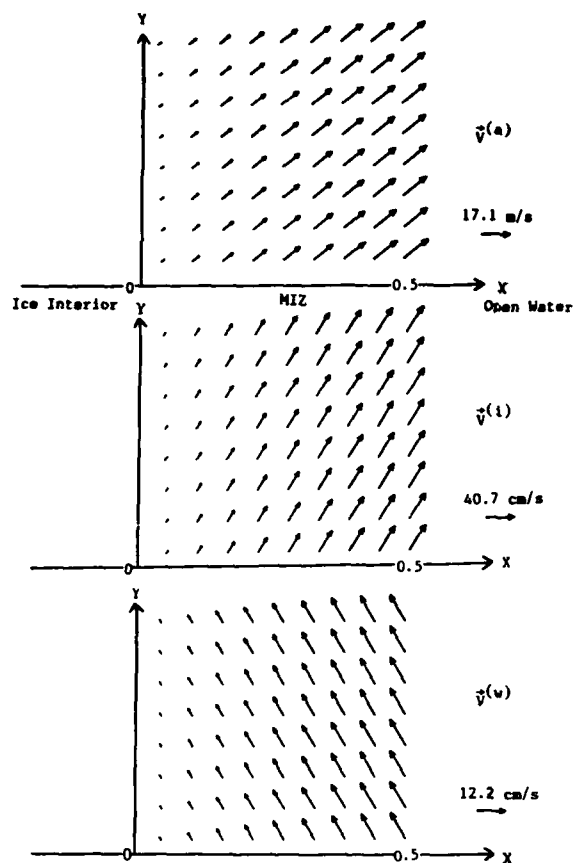
a. $H_i = 0.7\,m$, $H_w = 40\,m$.

b. $H_i = 0.7\,m$, $H_w = 10\,m$.
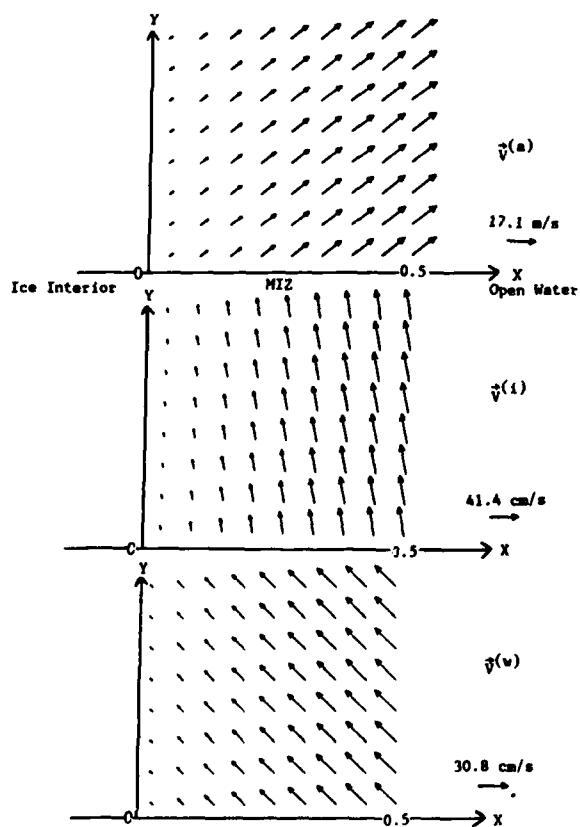
c. $H_i = 6\,m$, $H_w = 10\,m$.

Fig. 7. $\vec{V}^{(a)}$, $\vec{V}^{(i)}$ and $\vec{V}^{(w)}$ in the south polar region $(\phi = 65°S$, $N = 10^{-2}\,s^{-1})$.

87

END

10 — 86

DTIC